THÈSE POUR OBTENIR LE GRADE DE DOCTEUR DE L'UNIVERSITÉ DE MONTPELLIER

En Électronique

École doctorale I2S

Unité de recherche UMR 5214

Single Event Latchup: Temperature effects, design parameters and mechanisms

Présentée par Salvatore GUAGLIARDO

Le 17 décembre 2021

Sous la direction de Prof. Frédéric Wrobel et Prof. Jean-Luc Autran

Devant le jury composé de

Frédéric SAIGNÉ, Pr., Université de Montpellier	Président de jury
Mourad BENABDESSELAM, Pr., Université Cote d'Azur	Rapporteur
Paul LEROUX, Pr., Université Catholique de Leuven	Examinateur
Jean-Luc Autran, Pr., Université Aix-Marseille	Co-Directeur
Frédéric WROBEL, Pr., Université de Montpellier	Directeur
Karine COULIÉ, Maître de conférences, Université Aix-Marseille	Examinatrice

Les rapporteurs du manuscrit sont

Mourad BENABDESSELAM, Pr., Université Cote d'Azur	Rapporteur
Philippe PAILLET, Dr., CEA, Bruyère le Châtel	Rapporteur

UNIVERSITÉ DE MONTPELLIER

Table of contents

ABSTRACT ..... **I**

RESUMÉ ..... **II**

INTRODUCTION ..... **V**

CHAPTER 1: RADIATION ENVIRONMENT **1**

1.1 SPACE RADIATION **2**

1.1.1 Galactic Cosmic Rays *2*

1.1.2 Solar particles *5*

1.1.3 Trapped particle radiation *6*

1.1.4 Atmospheric environment *9*

1.2 FACILITIES RADIATION ENVIRONMENT **11**

1.2.1 High-energy physics accelerators *11*

1.2.2 Nuclear power plants *12*

1.3 INTERACTION OF RADIATION WITH MATTER **12**

1.3.1 Neutrons and protons interaction *14*

1.3.2 Photons interaction *15*

1.3.3 Charged particle interactions *19*

1.3.4 Electron and positron interactions *20*

1.3.5 Heavy ions *22*

1.4 CONCLUSION **28**

CHAPTER 2: SINGLE EVENT LATCHUP **30**

2.1 SINGLE EVENT EFFECTS **31**

2.2 SINGLE EVENT LATCHUP **33**

2.2.1 SEL: basic structure and electrical characteristics *34*

2.2.2 SEL: triggering dynamics *38*

2.2.3 Effect of the temperature on Single Event Latchup *40*

2.2.4 Single Event Latchup mitigation techniques *44*

2.3 CONCLUSION 47

CHAPTER 3: SIMULATION TOOLS 49

3.1 TCAD 50

3.1.1 Sentaurus Synopsys 53

3.1.2 ECORCE 62

3.2 SPICE 65

3.3 CONCLUSION 68

CHAPTER 4: SINGLE EVENT LATCHUP CROSS SECTION CALCULATION FROM TCAD SIMULATIONS 70

4.1 METHODOLOGY 71

4.1.1 Simulated structure 72

4.1.2 Parameter variation 74

4.1.3 Cross section calculation 76

4.1.4 SEL Rate 78

4.1.5 Simulation physics and ion track 78

4.2 EFFECTS OF LAYOUT MODIFICATION 79

4.3 TEMPERATURE EFFECTS 84

4.3.1 Threshold LET analysis 86

4.3.2 SEL rate analysis 90

4.4 DISCUSSION 96

4.5 CONCLUSION 99

CHAPTER 5: SINGLE EVENT LATCHUP PREDICTION USING TCAD AND SPICE SIMULATIONS 102

5.1 PREDICTION OF SEL USING TCAD AND SPICE SIMULATIONS 103

5.1.1 Simulated structure and short track 103

5.1.2 Current sign 104

5.1.3 Single Event Latchup mechanism 106

5.1.4 Comparison between Sentaurus and ECORCE 117

5.1.5 Comparison between short track and long track 120

5.1.6 Single Event Latchup electrical simulations with SPICE 124

5.2 PREDICTION OF SEL USING TCAD SIMULATIONS 129

5.2.1 Methodology 129

5.2.2 Results and analysis 132

5.3 CONCLUSIONS 138

GENERAL CONCLUSIONS 141

APPENDIX 149

REFERENCES 154

List of figures

Figure 1.1 Different space radiation sources [1]. 2
Figure 1.2 Relative abudances at 2 GeV of ions in the solar system (SS) and in the galactic cosmic rays (GCR) [7] 3
Figure 1.3 Relative contribution in fluence (green), dose (blue) and dose equivalent (red) as in the work of Durante et al. [9] 4
Figure 1.4 GCR fluxes for representative ions. Minimum and maximum refer to the periods within the solar cycle [10]. 5
Figure 1.5 Schematic of radiation belts showing the inner radiation belt and the outer radiation belt [18]. 7
Figure 1.6 Map of the Earth's magnetic field. The large red area is the South Atlantic Anomaly [19]. 8
Figure 1.7 Mechanism of primary component of terrestrial cosmic rays [3]. 9
Figure 1.8 Simulation as performed in [11], where the neutron spectra and proton spectra are shown using the MAIRE model. 10
Figure 1.9 World map showing ambient dose-equivalent rate at 12 km altitude due to GCR ions as in [11]. 10
Figure 1.10 Photoelectric cross section for silicon [26]. 17
Figure 1.11 Compton cross section for silicon, with the Brusa approach and the Klein-Nishina formula [26]. 18
Figure 1.12 Mass stopping power for an aluminum ion in silicon [30]. 24
Figure 1.13 Electronic stopping power of silicon ion in silicon [26]. 25
Figure 1.14 Comparison of electronic stopping power of B, C, N and Be in silicon as in [37]. 26
Figure 1.15 Range versus energy for different ions from Z=1 to Z = 15 in silicon [30]. 27
Figure 1.16 LET in silicon the ion cocktail of the RADiation Effects Facility (RADEF), a specialized facility in the study of radiation effects in electronics and related materials [39]. 27

Figure 2.1 Direct and indirect ionization. During direct ionization, the electron—hole pairs are created directly by the incident particle. In the indirect ionization, the incident particle will release its energy to a secondary particles, that will eventually create the electron-hole pairs [40]. 32
Figure 2.2 Parasitic bipolar portion of N-well CMOS inverter [46]. 34
Figure 2.3 Complete circuit schematics for N-well CMOS inverter [46]. 35
Figure 2.4 PNPN structure with the relative parasitic transistors.....36
Figure 2.5 I-V characteristics of the PNPN structure [46]. 37
Figure 2.6 Schematic circuit of the PNPN structure as in [42] 37
Figure 2.7 Schematic circuit of the PNPN structure as in [48] 38
Figure 2.8 Electrostatic potential inside the PNPN structure. In (a) it is shown the electrostatic potential before the ion hits, in (b) it is shown the electrostatic potential after the strike. Simulations are performed with Sentaurus Synopsys. 39
Figure 2.9 Latchup current at Source terminal and generation rate versus time as in [46].....39
Figure 2.10 Potential increase in the substrate, before and after activation of the NPN transistor [50] 40
Figure 2.11 The Latchup threshold V_{DD} as a function of temperature for the three different strikes types [51].....41
Figure 2.12 Current versus voltage curve for an emitter-base junction [52]. 43
Figure 2.13 Cross setion of a floating-body CMOS SOI technology [60]. 44
Figure 2.14 Cross section of a BiCMOS SOI technology [60]. 45
Figure 2.15 Cross section of triple well CMOS technology [60]. 46
Figure 3.1 Typical TCAD components. 51
Figure 3.2 Mesh on an NMOS structure, where the node and the finite element are highlighted.....52
Figure 3.3 Flow of simulation tools by Sentaurus Synopsys. 54
Figure 3.4 Sentaurus Workbench graphical user interface. 54
Figure 3.5 Ion strike definition in Sentaurus Synopsys [72]. 62
Figure 3.6 Temporal function for the ion generation in ECORCE [76]. 63

Figure 3.7 ECORCE's mesh design process [76] 64
Figure 3.8 Example of a SPICE input deck 67
Figure 4.1 2D structure of the PNPN built with Sentaurus Structure editor 73
Figure 4.2 Top view of a 65nm based CMOS inverter developed in Cadence Virtuoso 74
Figure 4.3 2D structure of the NPNP with the different mesh used. 74
Figure 4.4 PNPN structure with the parameters considered in our simulations and representing the parasitic transistors. 75
Figure 4.5 Source current versus time for different LET values. 76
Figure 4.6 Minimum LET value versus position. 77
Figure 4.7 Example of SEL cross section calculated with our methodology. 77
Figure 4.8 The methodology used to calculate the effect of the design parameter variation. 79
Figure 4.9 SEL cross section for temperature 80
Figure 4.10 SEL threshold LET (top) and cross section for Anode to cathode spacing (bottom) 81
Figure 4.11 SEL threshold LET (top) and cross section for doping profile factor (bottom). 82
Figure 4.12 SEL threshold LET (top) and cross section for substrate and well taps placement (bottom). 83
Figure 4.13 The methodology used to calculate the effect of the temperature variation. 85
Figure 4.14 Example of the charts used in this chapter. 86
Figure 4.15 Threshold LET versus the doping profile factor for four different temperatures (350 K, 375 K, 400 K, 425 K). 87
Figure 4.16 Threshold LET versus the anode to cathode spacing for four different temperatures (350 K, 375 K, 400 K, 425 K). 88
Figure 4.17 Threshold LET versus the well and substrate taps distance for four different temperatures (350 K, 375 K, 400 K, 425 K). 89
Figure 4.18 Heavy Ion SEL rate at GEO orbit versus the doping profile factor for four different temperatures (350 K, 375 K, 400 K, 425 K). 91

Figure 4.19 Heavy Ion SEL rate at GEO orbit versus the well and substrate taps distance for four different temperatures (350 K, 375 K, 400 K, 425 K). 92
Figure 4.20 Heavy Ion SEL rate at GEO orbit versus the anode to cathode spacing for four different temperatures (350 K, 375 K, 400 K, 425 K).....93
Figure 4.21 Heavy Ion SEL rate at LEO orbit versus the doping profile factor for four different temperatures (350 K, 375 K, 400 K, 425 K). 94
Figure 4.22 Heavy Ion SEL rate at LEO orbit versus the anode to cathode spacing for four different temperatures (350 K, 375 K, 400 K, 425 K).....95
Figure 4.23 Heavy Ion SEL rate at LEO orbit versus the well and substrate taps distance for four different temperatures (350 K, 375 K, 400 K, 425 K). 96
Figure 4.24 Recap of the parameters influence on SEL sensitivity.....99
Figure 5.1 Heavy ion generation in Sentaurus. Circled in red is the ion track in point B. 104
Figure 5.2 The injection points (red rectangles) highlighted in the PNPN structure 105
Figure 5.3 Convention sign when I>0. 106
Figure 5.4 Convention sign when I<0. 106
Figure 5.5 Example of the current charts. On the left of the chart we show the contact. Then, three different LET are used. 107
Figure 5.6 Complete current charts for point B. 108
Figure 5.7 Complete current charts for point H. 109
Figure 5.8 BN+ electrons and holes current for point B. Step 1 is circled. 110
Figure 5.9 BP+ electrons and holes current for point H. Step 1 is circled110
Figure 5.10 SP+ electrons and holes current for point B. Step 2 is circled. 111
Figure 5.11 SN+ electrons and holes current in point H. Step 2 is circled. 112
Figure 5.12 SN+ electrons and holes current for point B. Step 3 and Step 3* is circled. 112
Figure 5.13 SP+ electrons and holes current for point H. 113

Figure 5.14 SN+ electrons and holes current on the top, and SP+ electrons and holes current on the bottom for point B. Step 4 is circled. 114
Figure 5.15 SP+ electrons and holes current on the top, and SN+ electrons and holes current on the bottom for point H. Step 4 is circled. 114
Figure 5.16 SN+ electrons and holes current on the top, and SP+ electrons and holes current on the bottom for point B. Step 5 is circled. 115
Figure 5.17 SP+ electrons and holes current on the top, and SN+ electrons and holes current on the bottom for point H. Step 5 is circled. 116
Figure 5.18 SP+ electrons and holes current for point B. Step 6_A and 6_B are circled. 116
Figure 5.19 SN+ electrons and holes current for point B. Step 6_A and 6_B are circled. 116
Figure 5.20 BN+ electrons current in Sentaurus (left) and ECORCE (right). Step 1 is circled. 118
Figure 5.21 SP+ electrons current in Sentaurus (left) and ECORCE (right). Step 2 is circled 118
Figure 5.22 SN+ electrons current in Sentaurus (left) and ECORCE (right). Step 3 is circled 119
Figure 5.23 SN+ electrons current in Sentaurus (left) and ECORCE (right). Step 4, 5 and 6 are circled 119
Figure 5.24 Heavy ion generation in Sentaurus for the long track. The red line is the ion track generated by the software. 120
Figure 5.25 BN+ electrons current for the short track (left) and long track (right) for point B. Step 1 is circled. 121
Figure 5.26 BP+ electrons current for the short track (left) and long track (right) for point B. Step 1 is circled. 121
Figure 5.27 SP+ holes current for the short track (left) and long track (right) for point B. Step 2 is circled. 122
Figure 5.28 SN+ electrons current for the short track (left) and long track (right) for point B. Step 3 is circled. 122
Figure 5.29 SN+ electrons current for the short track (left) and long track (right) for point B. Step 4 is circled. 123

Figure 5.30 SN+ electrons current for the short track (left) and long track (right) for point B. Step 5 and 6 are circled. 123
Figure 5.31 PNPN structure showing the electron-hole pair separation and the electrode currents. Green zones represent depletion layer. I_1 , I_2 and I_3 are the currents due to separation of electron-hole pairs. 124
Figure 5.32 Schematic circuit of the PNPN structure. I_1 , I_2 and I_3 represent the injection of charges at the junctions (electron-hole pair separation) 125
Figure 5.33 Pulse current used in our SPICE simulations in order to mimic the electron-hole pair separation. Threshold is obtained by varying the amplitude of the pulse..... 126
Figure 5.34 Current at the four terminal (BP+ and Sub are sum) for SPICE simulations (left) and Sentaurus short track configuration simulations (right) 127
Figure 5.35 Typical pulse current obtained with the diffusion model. Here N0=62500 pairs, r=1μm, the depletion area is 1μm^2, D=36 cm^2/s and recombination were assumed to be negligible..... 128
Figure 5.36 Set of deposition points used in the TCAD simulations. We have divided the points in three groups: substrate, n-well and under n-well... 130
Figure 5.37 Electric field color maps from Sentaurus. The collection point C_1,C_2,C_3 are shown. 131
Figure 5.38 Threshold charge versus r (distance of the deposition point from the collection point C_1) for the substrate group. The dotted line represents the linear trendline. The equation and the R^2 value are annotated in the chart..... 133
Figure 5.39 Threshold charge versus r (distance of the deposition point from the collection point C_2) for the n-well group. The dotted line represents the linear trendline. The equation and the R^2 value are annotated in the chart. 133
Figure 5.40 Threshold charge versus r (distance of the deposition point from the collection point C_3) for the under n-well group. The dotted line represents the linear trendline. The equation and the R^2 value are annotated in the chart..... 134
Figure 5.41 Efficiency factor versus X position for the substrate group. 135

Figure 5.42 Efficiency factor versus r for the substrate group. The colours represents points from the same X position. 135
Figure 5.43 Efficiency factor versus X position for the under n-well group. 136
Figure 5.44 Efficiency factor versus r for the under n-well group. The colours represents points from the same X position. 136
Figure 5.45 Efficiency factor versus X position for the n-well group..... 137
Figure 5.46 Efficiency factor versus r for the n-well group. The colours represents points from the same X position 137
Figure A.1 Complete current charts for point A. 149
Figure A.2 Complete current charts for point C. 150
Figure A.3 Complete current charts for point G. 151
Figure A.4 Complete current charts for point I. 152

List of tables

Table 1.1 Reaction products of the reaction n + ^{28}Si below 5 MeV threshold 15
Table 2.1 Temperature-Dependent parameters [55]**.** The ratio is given by the value of the parameter at 125° C and at 25° C. 43
Table 3.1 Mobility models available in Sentaurus**.** 60
Table 3.2 Circuit elements present in SPICE 66
Table 3.3 Type of analysis available in SPICE 67
Table 4.1 Summary of the parameters used in the simulations 75
Table 4.2 SEL Rate calculated for different parameters. 84
Table 4.3 Summary of the parameters used in the simulations 84
Table 4.4 Example of the tables used in this chapter. 86
Table 4.5 Summary results for threshold LET relative difference for the doping profile factors. 87
Table 4.6 Summary results for threshold LET relative difference for the well and substrate taps placement. 88
Table 4.7 Summary results for threshold LET relative difference for the anode to cathode spacing. 90
Table 4.8 SEL rate difference at GEO orbit for the doping profile variation, starting from 425 K. 91
Table 4.9 SEL rate difference at GEO orbit for the well and substrate taps distance, starting from 425 K. 92
Table 4.10 SEL rate difference at GEO orbit for the anode to cathode spacing, starting from 425 K. 93
Table 4.11 SEL rate difference at LEO orbit for the doping profile variation, starting from 425 K. 94
Table 4.12 SEL rate difference at LEO orbit for the anode to cathode spacing, starting from 425 K. 95
Table 4.13 SEL rate difference at LEO orbit for the well and substrate taps distance, starting from 425 K. 96
Table 5.1 Coordinates of the points used in the simulations. 105

Table 5.2 Coordinates of deposition points for the under n-well group..129
Table 5.3 Coordinates of deposition points for the substrate group. 130
Table 5.4 Coordinates of deposition points for the n-well group.....131
Table 5.5 Coordinates of the collection points.....132

Acknowledgement

Firstly, I would like to thank my supervisor Prof. Frédéric Wrobel. His help during these years, especially in the last, has been fundamental for the good outcome of this work. I have learned a lot from him about academic research and I will always be grateful to him for the opportunity that he gave me by letting me participate to RADSAGA. I would like to thank also Prof. Jean-Luc Autran and Prof. Paul Leroux, for their help and support during my secondments in their laboratories.

Secondly, I would like to show my gratitude to the RADSAGA project and to all the people involved in it, especially Sonia Allegretti, for her help and support. Then, I would like to thank my colleagues at the RADIAC team. They have cheered up the days in the lab and helped me in many different ways during these years. So, I would like to thank Ygor, Kimmo, Georgios, Thomas, Samir, Arthur, Gaetan, Hoang, Israel, Catherine and all the other people that helped in one way or another during my period at IES.

Lastly, I thank my family for their support from the beginning of my studies, up until now. And last but not least, I would like to thank my girlfriend Giulia, because without her support and motivation it would have been harder to withstand the pressure and fatigue during these years.

Abstract

Radiation effects on electronic components have become a crucial issue in our modern era. Whether on ground or on space applications, radiation poses a threat to the electronic devices. One of this threat is Single Event Latchup (SEL), which is a potential catastrophic condition that affects CMOS technology. It is a destructive effect and its occurrence is dependent on design parameters. So, the goals that we set for this work are to investigate the effects of specifics design parameters on SEL sensitivity and to identify a method to predict SEL.

The first part of this scope has been addressed by the investigation of the effects of specific design parameters on SEL sensitivity. The chosen parameters were doping profile, anode to cathode spacing and well and substrate taps placement. In addition, we have investigated the effect of temperature, which is a well-known key parameter for SEL sensitivity, in combination with the variation of the others parameters. TCAD tools have been used, by performing 2D simulations of a NPNP structure using Sentaurus Synopsys and ECORCE.

On the other hand, two methods to predict SEL have been explored. The first method relies on the dynamic of SEL. By using TCAD simulations, we have identified the steps that lead to SEL. Then, these steps have been used to develop a modeling circuit in SPICE, in order to use it for prediction. With the second method, we have analyzed a possible model to predict SEL considering only the charge collected and deposited in the device, by finding a correlation between the deposited charge and the occurrence of SEL.

Résumé

Dans l'ère technologique dans laquelle nous vivons, la fiabilité est un aspect crucial dans chaque domaine technologique. De l'aviation à l'automobile, les ingénieurs ont besoin de systèmes fiables qui remplissent la tâche qui leur est confiée. Cependant, les problèmes de fiabilité sont liés à différentes conditions et chaque condition doit alors être parfaitement comprise afin d'augmenter la fiabilité du système. Le rayonnement en fait partie. Le rayonnement a été découvert au XVIIIe siècle et depuis lors a été étudié pour ses effets positifs et négatifs. Parallèlement, de nouvelles technologies sont apparues. Par exemple, les composants électroniques ont commencé à être développés dans les années 50 et sont aujourd'hui la pierre angulaire de notre société moderne. Ils sont utilisés dans une variété impressionnante de domaines, des appareils électroménagers aux satellites. En clair, plus le système est crucial, plus la fiabilité est une préoccupation majeure. Du sol à l'espace en passant par l'aviation, les rayonnements constituent une menace majeure pour les composants électroniques. Ainsi, l'étude des effets des rayonnements et de leur impact sur les appareils électroniques a un rôle important sur leur fiabilité. L'une de ces effets est le Single Event Latchup (SEL) qui affecte les composants de technologie CMOS de façon potentiellement destructive et dont l'apparition dépend des paramètres de conception. Le SEL est connu depuis les années 60 et il a été étudié depuis lors, en raison du rôle important que les composants CMOS ont joué sur le marché des circuits intégrés. C'est un effet destructeur et comme tout autre effet de rayonnement, la sensibilité de Single Event Latchup dépend de différents paramètres. Ainsi, les objectifs que nous nous sommes fixés pour ce travail sont d'étudier les effets des paramètres de conception sur la sensibilité du SEL et d'identifier une méthode pour prédire le SEL.

La première partie de ce travail consiste en une étude des effets des paramètres de conception spécifiques sur la sensibilité SEL. Les paramètres choisis sont le profil de dopage, l'espacement anode-cathode et le placement des prises de puits et de substrat. De plus, nous avons étudié l'effet de la température, qui est un paramètre clé bien connu pour la sensibilité SEL, en combinaison avec la variation des autres paramètres. Des outils TCAD ont été utilisés, en effectuant des simulations 2D d'une structure NPNP à l'aide de Sentaurus Synopsys et ECORCE.

Dans la seconde partie de ce travail, deux méthodes pour prédire le SEL ont été explorées. La première méthode repose sur la compréhension des mécanismes du SEL. En utilisant des simulations TCAD, nous avons identifié les étapes qui mènent au SEL. Ensuite, ces résultats ont été utilisés pour développer un circuit de modélisation dans SPICE, afin de l'utiliser pour la prédiction. Nous présentons un modèle pour prédire le SEL en considérant uniquement les charges déposée et collectée dans le dispositif.

Introduction

In the technologic era in which we are living, reliability is a crucial aspect in every technology area. From aviation to cars, engineers need reliable systems that fulfill the task they are given to. However, reliability issues are related to different conditions and then every condition has to be fully understood in order to increase the reliability of the system. Radiation is one of these. Radiation has been discovered in the XVIII century and since then has been studied for its positive and negative effects. At the same time, new technologies have emerged. For instance, electronic components have been started to be developed in the '50s and nowadays are the cornerstone of our modern society. They are used in an impressive variety of field, from appliances to satellites. Clearly, the more the system is crucial, the more reliability is a major concern. From ground, to space, to aviation, radiation poses a major threat to electronic components. Thus, investigation of radiation effects and their impact on electronic devices has an important role on their reliability.

Due to the increasing concern on radiation effects on electronic components, the topic has become of interest for universities and industry. For this reason, in 2015 a network composed by 31 partners from 11 different European countries, launched a proposal for an Innovative Training Network in the frame of the Marie Skłodowska-Curie Actions funded by the European Commision. This project has been approved in 2016 and was called RADSAGA which stands for RADiation and reliability challenges for electronics used in Space, Aviation, Ground and Accelerators. The goal of this project is to boost the development of research on the radiation effects in electronics and to stimulate the cooperation among industry, universities and laboratories. Because of that, the RADSAGA network launched 15 PhDs proposals to tackle this topic. The 15 PhDs were divided in four work packages, depending on the field of interest. Work Package 1 deals with the environments, the facilities and the monitoring, Work Package 2 concerns the reliability and testing at component level

aspect, Work Package 3 is about qualification requirements at system level and finally Work Package 4 deals with methodologies and guidelines. The present work was developed inside the RADSAGA project and specifically inside the Work Package 2. Within this Work Package, several aspects of reliability of electronic components have been investigated. In fact, radiation may cause different effects, depending on the type of radiation and the type of component. Generally, these effects are divided in three categories: Total Ionizing Dose, Single Event Effects and Displacement Damage. The first is related to the accumulation of deposited charge by radiation in the component, the second is related to the effect of a single particle and the third is the result of atom displacement due to particle knock-out. Among these, Single Event Effects (SEE) includes a several number of different varieties. Usually, these effects are divided in non-destructive or destructive: destructive effects (also called hard errors) are not recoverable meanwhile non-destructive effects (also called soft errors) may be recovered by a reset or a power cycle. Some non-destructive error are, for instance, Single Event Upset (SEU) or Single Event Transient (SET). One the destructive effects is the Single Event Latchup (SEL). Specifically, SEL arises from the parasitic transistors which are inherently present inside a CMOS component. If radiation releases enough energy to trigger these transistors and to sustain a regenerative loop between them, a high current path will be present in the device, leading to the possible destruction of the component itself.

Single Event Latchup is the main topic of this work. As aforementioned, CMOS based components are sensitive to SEL, due to their nature. Basically, sources, well and substrate taps form a PNPN structure inside the component. This structure, which is also called thryristor, is responsible of Single Event Latchup. SEL is known since the ‘60s and it has been studied since then, because of the important role that CMOS components have assumed in the integrated circuit market.

As any other radiation effect, Single Event Latchup sensitivity depends on different parameters. First of all, temperature is one of these. Several

studies have been done about this aspect, by investigating the effects of lower temperature, as low as 50 K, and high temperature. Furthermore, the design choice of the device will influence the SEL sensitivity. The engineers can use different design choices for their device to fulfill their task, but these choices will influence not only the desired outcome, but also drawbacks.

The goal of this work is to investigate the effects of specifics design parameters on SEL sensitivity and to identify a method to predict SEL. The outline of the manuscript is the following. In the first chapter, we discuss about the different radiation environments that electronic devices may face. Every environment is different and will pose different challenges to the devices, so it is important to know the composition in energy, type of particle and flux to be able to cope with their effects. In the second chapter, we introduce Single Event Effects, specifically, Single Event Latchup. We show the triggering mechanism of SEL, the effect of the temperature and Radiation Hardening by Design (RHBD) on SEL sensitivity. In the third chapter, we focus our attention on the tools that has been used in this work. In fact, simulations have been used to reach the goal of this work. Specifically, TCAD simulations and SPICE simulations have been chosen. Then, in the fourth chapter, we start to investigate the effects of design parameters, specifically, doping profile, anode to cathode spacing and well and substrate taps placement. This investigation has been performed with 2D TCAD simulations and SEL cross sections and SEL rate have been calculated from them. Furthermore, we continue the investigation on these parameters. In particular, the effects of temperature in combination with the variation of the previous parameters has been analyzed. SEL cross sections and SEL rate have been calculated again. In conclusion, in the fifth chapter we investigate two methods for Single Event Latchup prediction. The first one uses TCAD simulations to study the dynamic of SEL. Once this was achieved, SPICE simulations have been used to create a modeling circuit that could mimic the dynamic found in the TCAD simulations. On the other hand, the second method, using only TCAD simulations, has the goal to correlate the charge deposited in the device and the manifestation of SEL. Eventually, the general

conclusions of this work are presented, adding some possible improvements for future development.

Chapter 1
Radiation Environment

Electronic components are used in almost every application. From space to ground, it is hard to find a field in which electronics is not used. They are often a crucial part of a system and so, their reliability is fundamental for their application. This depends not only on the electronic design, but also on the environment in which they operate. Every environment has different characteristic and it may pose a threat to the instrumentation. In this work, we focus on the different radiation environments in which electronic components may be used. In this chapter, we are going to highlight some of the most relevant for our case, specifying their main characteristics related to electronic devices.

1.1 Space radiation

Since from the beginning of the space era, radiation has been a major concern, both for human and electronics. Space environment is different from the kinds of radiation we experienced on Earth. Space radiation can be split into two populations: the particles trapped by planetary magnetospheres and transient particles, that consist in galactic cosmic rays (GCR) [1] and particles coming from solar events [2]. In this paragraph, we are going to discuss about these particles and their energies and fluxes. Also, we will consider the radiation environment on Earth, due to the interaction of space radiation with the Earth's atmosphere [3].

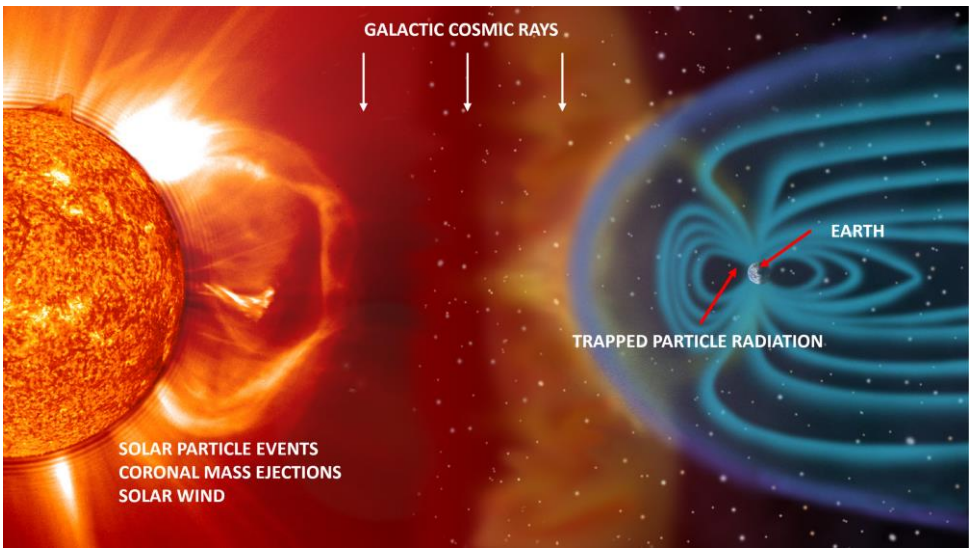

Figure 1.1 Different space radiation sources [1].

1.1.1 Galactic Cosmic Rays

Galactic cosmic rays were discovered by Victor Hess in 1912. Even though in the previous years some speculation about highly penetrating radiation coming from space was made, it was thanks to his work that it was proven their existence. He made observations on board a balloon. Starting at sea level, he measured with an ionization chamber a production of 15-16 ions/cm^3. Meanwhile, the ionization rate at 4000-5000 meters was 34

ions/cm^3. Thus, he obtained strong evidences that ionization rate increases with the altitude [4].

Galactic cosmic rays are originated from outside the Solar System and they collide isotropically on Earth. GCR are composed by elements of the periodic table with a nuclear charge from 1 to 92. Their origin can be rooted from supernova explosions, neutron stars, pulsars, and other sources where high energetic phenomena are involved [5]. Due to their composition and their energies, they can represent a significant risk to long duration spaceflight outside the magnetosphere [6]. What is relevant, it is the abundances of the particles that form the GCR [Figure 1.2] [7]. Many studies have reported a composition predominant of protons, then alpha particles and traces of heavier nuclei such as carbon and iron are also present [8]. Ions heavier than helium are called HZE particles (High atomic number Z and high energy E). Although they are only a small fraction of the total population, HZE are of great concern because of their effect on human being and electronic instrumentation. In Figure 1.3, the relative contributions in fluence, in dose and dose equivalent from the work of Durante *et al.* [9] are shown. The figure shows that the heavier particles, even though their

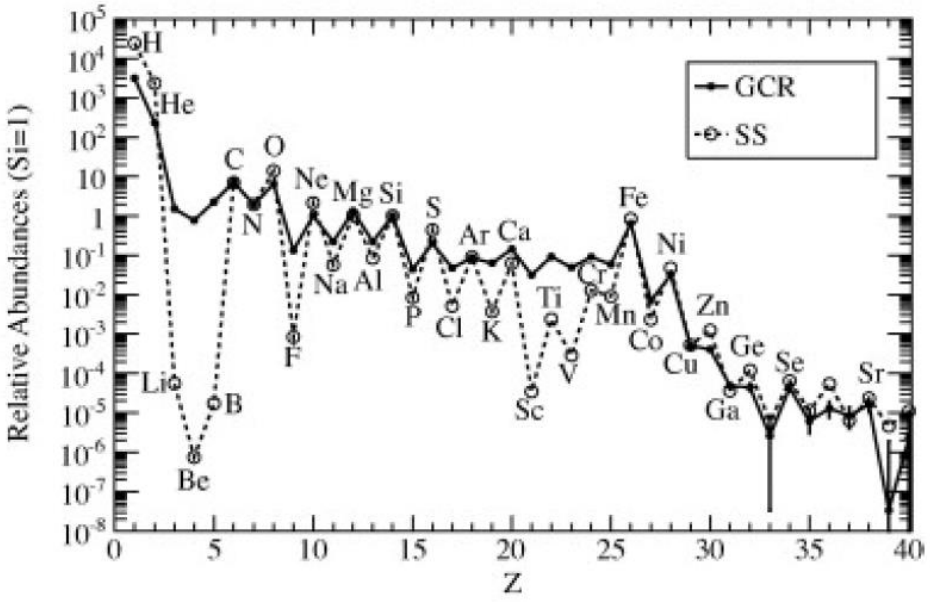

Figure 1.2 Relative abundances at 2 GeV of ions in the solar system (SS) and in the galactic cosmic rays (GCR) [7] .

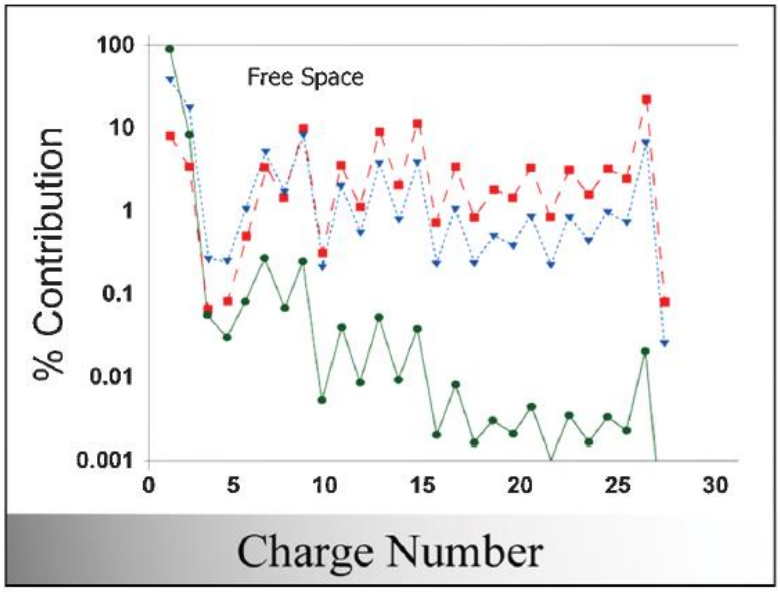

Figure 1.3 Relative contribution in fluence (green), dose (blue) and dose equivalent (red) as in the work of Durante *et al.* [9] .

abundance is considerably lower in comparison to lighter particles as carbon or oxygen, is more relevant. For instance, GCR constitutes more than 80% of the effective dose that the ISS crew receives.

The energy of the GCRs ranges between 10^9 eV up to 10^{20} eV. The flux is dependent on the energy and it is shown in Figure 1.4 [10]. However, GCR flux is not always constant. As GCR are coming from the outside of our solar system, when they enter they encounter the magnetic field of the solar particles. If the solar activity is high, GCR are scattered by the interplanetary magnetic field carried by the particles coming from the Sun [11] and thus the GCR flux decreases [9]. Vice versa, when the solar activity is at his minimum, GCR flux is at his maximum. Figure 1.4 shows this behavior. The effect of the Sun is also seen at low energies, in what it is called solar modulation. At energies lower than 1GeV/nucleon, the solar wind excludes the cosmic rays from the heliosphere. This effect is more pronounced at lower energies [6], [9].

In addition, some GCR particles may me able to cross the Earth magnetic field and then, reach the Earth atmosphere. Once there, the GCR will interact in the upper atmosphere, creating a “shower” of secondary particles. It was

thanks to these particles that GCR were discovered by Hess. In section 1.1.4, we will discuss about them in more detail.

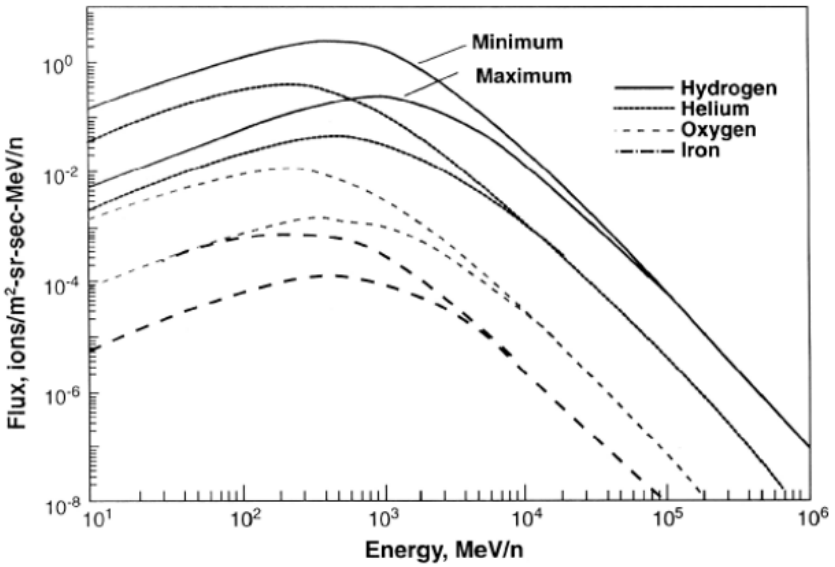

Figure 1.4 GCR fluxes for representative ions. Minimum and maximum refer to the periods within the solar cycle [10].

1.1.2 Solar particles

Due to its proximity to Earth, the major source of radiation in our solar system is the Sun. For the major part, the Sun emits all wavelengths in the electromagnetic spectrum, but the most dangerous part for space mission, it is the ionizing radiation. In fact, the Sun constantly emits particles radiation, that permeate the solar system. Additionally, instant bursts of particles (mainly protons) are released by the Sun and they are of very concern for space missions but also for their effect on Earth. The intensity and the occurrence of these event is highly dependent on the solar activity. The Sun follows an 11-year cycle, during which it varies its activity. This cycle is divided in solar maximum and solar minimum. During solar maximum period, the Sun is highly active. Because of that, its magnetic field is more able to shield GCR, but its activity is responsible for the occurrence of solar flares and coronal mass ejections (CME), which are huge blast of plasma in the interplanetary space. Meanwhile, during solar minimum, the activity of

the Sun is at its lowest. Then, the Sun is not able to shield from GCR and occurrence of solar flares or CME is rare. Occasionally, solar events can be observed during solar minimum phases [11].

The coronal mass ejections are emitted from the corona of the Sun [12], which is the outer atmosphere of the Sun and it extends many thousands of kilometers above the surface the Sun, meanwhile solar flares are a sudden explosion of energy situated near sunspots, which are dark regions in the surface of the Sun. At first, the CME were correlated to large flares [13]. Nowadays, the most accepted theory is that they are produced by a loss of stability of the coronal magnetic field [14] and that solar flares are not required to produce CME [15]. Nonetheless, the consequence of CME and solar flares is the release of energetic particles into the interplanetary space. These events are called Solar Particle Events (SPE). Due to their nature, SPEs likelihood is highly dependent on the solar activity. Their intensity is not constant and it is linked to the activity of the sun. For example, in an 11-years cycle, most of the total fluence is accumulated during two extra-large bursts [9]. Occasionally, solar events can be observed during solar minimum phases [11]. For these reasons, SPEs are highly unpredictable and can cause serious damages to the equipment and astronauts. During these events, the energy can reach 100 MeV/u and their peak flux at 1 AU from the Sun can be around $3x10^4$ particles/cm^2/s [1].

The constant part of the solar radiation is called “solar wind”. As mentioned, it is a constant flow coming from the corona of the Sun, consisting mainly of protons and electrons, but with traces of heavy ions [9], with a peak flux between 2 to $4x10^8$ particles/cm^2/s and energies between 1 eV and 10 keV [3].

1.1.3 Trapped particle radiation

The existence of trapped particles by magnetic field of the Earth was speculated since 1895. Kristian Birkeland started to investigate the mechanism of trapping of particles by a magnetic field. Later, other scientists as Carl Stoermer, Fred Singer and Nicholas Christofilos have

continued to study that subject [15]. Eventually, thanks to Explorers 1 and 3 satellites and James Van Allen work, natural radiation belts around the Earth were discovered and name after him (Van Allen Belts) [Figure 1.5] [16]–[18].

Van Allen belts position is around the geomagnetic equator over a region from 200 km to about 75000 km and they are formed by protons and electrons [18]. Worth of mention, it is an anomaly of the belts, placed over the coast of Brazil, called "South Atlantic Anomaly" (SAA) (Figure 1.6) [19] where the belts reach an altitude lower than 200 km, due to the fact that the Earth magnetic field is tilted by 11 degrees with respect to the Earth rotation axis and has an offset of 500 km towards the north Pacific. It is an important area to consider because most of the radiation received in Low-Earth Orbit (LEO) is due to this region [9]. Van Allen Belts particles originate from the interaction of Galactic Cosmic Rays and solar particles with Earth's magnetic field and the atmosphere. It is composed of two belts, called inner and outer belts. The inner belt is constituted by protons and electrons. The proton zone is produced by decaying neutrons, that occurs when cosmic rays scatter off the neutral atmosphere (a mechanism called CRAND) [18], [20]. A contribution is coming also from solar flares and coronal mass ejections [21], [22]. Meanwhile, the electrons are periodically furnished by transport from the outer zone. The maximum energy of the protons is about

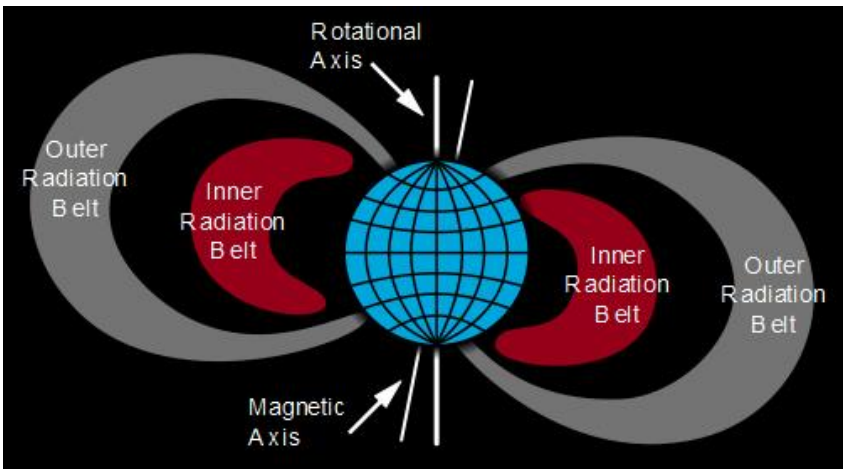

Figure 1.5 Schematic of radiation belts showing the inner radiation belt and the outer radiation belt [18].

500 MeV but this energy is only found at the core of the belt. Then, proton of 10 MeV are found and limited to altitudes below 20000 km, meanwhile protons of few MeV are observed at Geostationary orbit (GEO). On the other side, the outer belt is also formed by particles coming from the Sun, with a predominance of electrons with energy lower than 10 MeV [9].

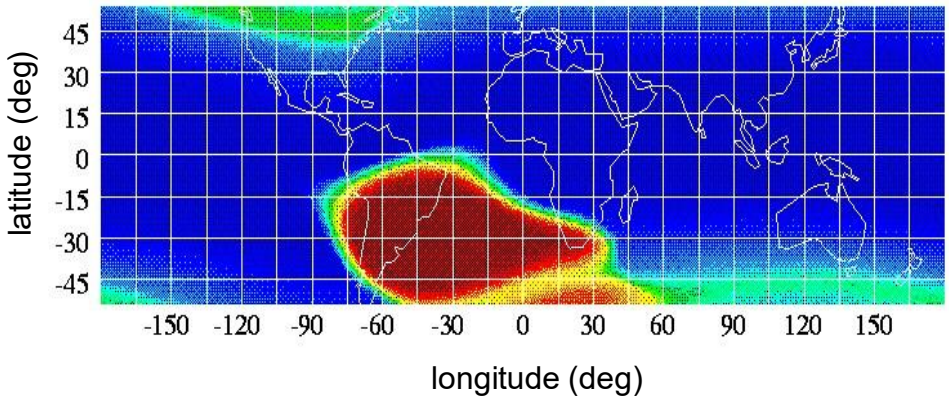

Figure 1.6 Map of the Earth's magnetic field. The large red area is the South Atlantic Anomaly [19].

The energy of the electrons is relatively low, with a maximum of 7 MeV. About the flux, the trapped radiation is modulated by the solar cycle. Then, the energy output from the sun reaches the atmosphere during the active phase of the solar cycle, increasing the density of atmospheric constituents normally encountered between 200 and 1000 km. Therefore, what happens is that for an high solar activity a lower proton intensity is measured, while electron intensity increases [23]. Vice versa, with low solar activity the electron intensity decreases, and the proton intensity increases. Several models for trapped electrons and protons are used, but NASA AP-8 and NASA AE-8 [24] represent the standard [9]. These are the only models to fully cover the region and they are based on satellites data from the '60s and the '70s.

1.1.4 Atmospheric environment

GCR and solar particles are not only a threat in outer space. As they collide with Earth atmosphere, they interact with nitrogen and oxygen. Their interaction leads to a "shower" of secondary particles [Figure 1.7]. These secondary particles are protons, electrons, neutrons, heavy ions, muons and pions, but the neutrons are of greater concern for radiation effects in the atmosphere. Their flux is not uniform, as secondary particles are the consequences of GCR and solar particles, and so they depend also on the activity of the Sun [2]. They follow an approximately 11 years solar cycle; during this cycle, if the activity of the Sun is at the minimum, GCRs are at a maximum and then also secondary particles on Earth. Plus, solar activity as solar flares, can generate a stream of charged particles that leads to the production of secondary particles on Earth's atmosphere.

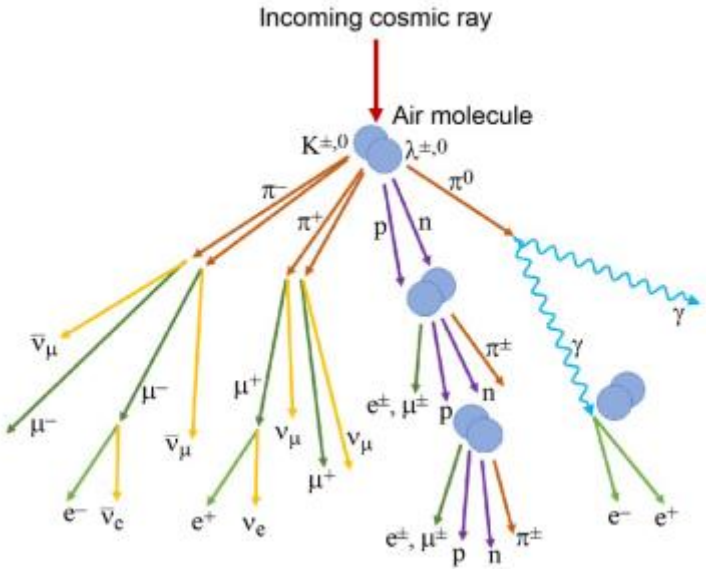

Figure 1.7 Mechanism of primary component of terrestrial cosmic rays [3].

Neutrons, protons and pions are of concern for effects of radiation on electronics, and the neutrons are of major concern because their flux is more relevant with respect to the other particles. Neutron energy spectra may vary depending on the altitude (they begin to appear at 330 km of altitude, and they have a peak at around 18 km), and they can reach energies up to

hundreds of MeV. At a first approximation, the neutron flux decreases as the energy increases and it is inverse proportional to the energy [Figure 1.8]. Moreover, particle flux is also dependent on the altitude. At 10 km altitude a flux greater than 300 times the ground level can be achieved. In addition, the particle fluxes depends also on the geomagnetic latitude, showing an increase close the northern and southern magnetic poles. In Figure 1.9, this aspect is explained by showing the ambient dose equivalent rate for different latitudes.

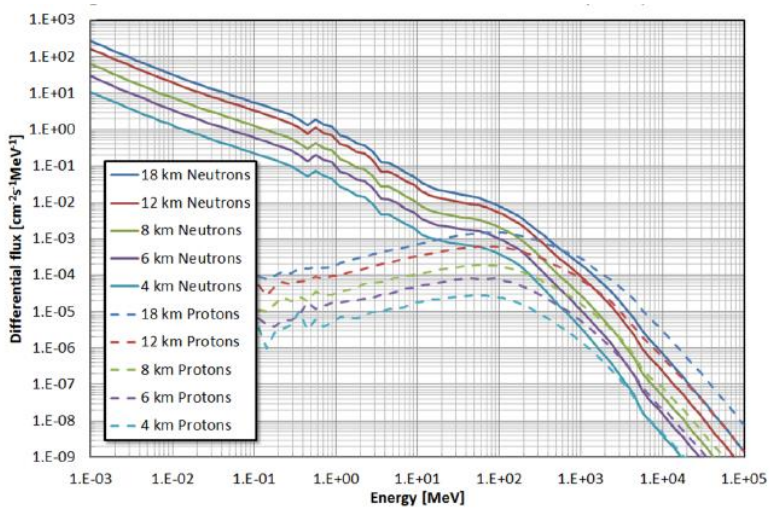

Figure 1.8 Simulation as performed in [11], where the neutron spectra and proton spectra are shown using the MAIRE model.

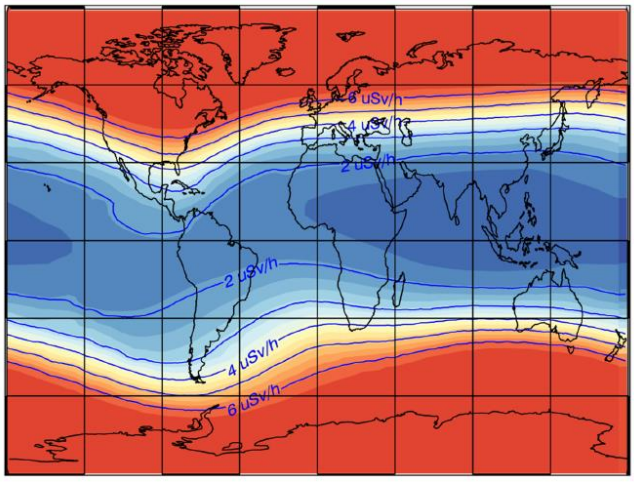

Figure 1.9 World map showing ambient dose-equivalent rate at 12 km altitude due to GCR ions as in [11].

1.2 Facilities radiation environment

Natural radiation environment is not the only threat to electronic components. Many man-made environments can pose some risk on electronic components, due to their radiation field. For example, nuclear reactors or accelerators are source of different kind of radiation. In these environments, electronic components are used for different purposes. They can be used for monitoring or controlling instruments. Moreover, they can be used in robots, in the case these environments are too risky for human being. In the next paragraph we are going to highlight some of the man-made environments and their characteristics.

1.2.1 High-energy physics accelerators

The goal of the high-energy physics research is to study short-lived particles that can be produced by colliding two beams of electrons or protons. These experiments are carried out at very high energy as 500 GeV and in massive facilities. These facilities are equipped with radiation detectors and electronic instruments needed to run the facility.

One example of high-energy accelerators is the Large Hadron Collider (LHC) at CERN [25]. The LHC is the longest accelerator on the planet (27 km) and the most energetic (~TeV). His environment consists of a mixed field of particles, as protons, kaons, neutrons, photons, electrons, and muons. These particles are generated from collision between protons or ions and by beam losses created by the interaction of the beam with the surrounding environment. The radiation environment inside LHC is disparate not only in terms of particles variety but also in terms of level of radiation. Depending on that, different choices can be made. At LHC, they divide the different zones: an area close to the tunnel; areas adjacent to the tunnel, with shielding; and “safe areas”, which are areas in which radiation levels is low enough for their scope. The used equipment, depending on which zone it will be placed and depending on its function, will be selected in order to

withstand a particular radiation environment, without causing the failure of the whole system.

1.2.2 Nuclear power plants

Nuclear power plants exploit fission reactions in order to produce energy. Thus, due to their nature, nuclear power plants can be one of the harshest radiation environments. Depending on the location inside the plant, different levels of severity have to be considered. For example, inside the reactor core, radiation levels are extremely high, and it is unlikely that electronic components will operate inside it. Meanwhile, many electronic components are present inside the reactor containment. Usually, the reactor is required to operate for 40 years and this leads to important levels of radiation accumulation for the equipment. Moreover, electronic equipment must withstand radiation during and after an accident. Nonetheless, other stress factors as ageing and temperature must be considered and then, qualification tests must be designed according to these requirements.

Nuclear power plants are not dangerous just when they are in activity. During their decommissioning, radiation levels are still high enough. Currently, this still involves human being in certain areas, but in non-accessible area, robots are used. Robots can be used also in accident situation, as it happened in Three Mile Islands (1979) and in Chernobyl (1986). Normally, robots will encounter gamma rays and thermal and fast neutrons but robots will be used in different locations with different radiation levels and so, it is arduous to define a precise spectra of neutrons and photons. Then, robots have to be qualified to withstand different kind of environments.

1.3 Interaction of radiation with matter

As we have seen from the previous paragraphs, electronic components have to face different radiation environments, with different types of radiation. Each kind of radiation will interact with the matter in a different

way and their interaction depends on the forces that are present between each particle [26]. These forces are among the four fundamental interactions which are present in the nature. The first is the *gravitational force*, which is the weakest in this contest because it is relevant when the interaction happens between massive objects. The second is the *weak interaction*, which is relevant in β-decay. The third is the *electromagnetic force* and the fourth is the *strong force.* However, our attention is on the last two, because these forces are involved in the interaction of radiation with matter. The electromagnetic force is implicated for uncharged particles interaction, as photons, and for charge particles as electrons, positrons and ions. Meanwhile, the strong force is present when neutrons and protons are involved (even though, proton can interact also via the electromagnetic force).

Then, the particles will interact through different effects which depend on their properties. The charged particles (both heavy and light) will interact mainly through elastic and inelastic collisions. Also, light charged particles will interact through bremsstrahlung emission and Cerenkov emission, meanwhile positron can undergo annihilation. Moreover, photons will interact in four ways: Rayleigh effect, the photoelectric effect, Compton scattering and pair production. Instead, neutrons will interact by absorption and scattering. Nevertheless, no matter the kind of interaction, the particles will lose at least part of their energy in the medium in which they interact. The loss of energy will contribute to the generation of electron-hole pairs inside the matter. This process is called ionization. Besides, part of the energy lost by the particles may contribute also to non-ionizing effects, which are not treated in this manuscript. In the following sections, we will discuss in detail the processes that lead to the ionization and how to calculate the energy loss by the particles in the medium that will cause ionization.

1.3.1 Neutrons and protons interaction

The force involved in the nucleons interaction is the *strong nuclear force*. Neutrons have no charge and thus they do not experience Coulombian forces. This means that they can travel considerable distance through the medium before having a collision. In order to collide, they have to be within a short range from an atomic nucleus. Meanwhile, protons have a dual behavior. Even though they are charged particles, if they have sufficient energy to overcome the Coulomb barrier, they may also interact with the nucleus through the strong force.

Neutrons and protons interactions can be elastic and nonelastic. In the elastic reactions, the kinetic energy of the system and the nature of the particles involved are conserved. Then, after the collision, part of the energy of the incident ion is transferred to the target nucleus. Consequently, the target atom can have sufficient energy to interact with the matter. In nonelastic collision, the kinetic energy is not conserved and the nature of the particles may change because one or several ions can be extracted from the nucleus. Consequently, these secondary ions may interact with the medium and then ionize it. In electronics, the main focus is on silicon. The reaction between a neutron and silicon ion may lead to several products and the knowledge of the products is important to evaluate the ionization of the matter. In Table 1.1, a short list of reaction products of the reaction between neutrons and silicon ion is shown at energy below 5 MeV. Each reaction has a threshold that is defined as:

$$E_{th} = -\frac{m+M}{M}Q \qquad \text{Eq. 1.1}$$

where M is the mass of the target nucleus, m is the mass of the incident nucleon and Q is what is called the *Q-value* of the reaction, which is the difference in mass energies of the products and the reactants. $Q < 0$ means that energy is required to activate the reaction.

Table 1.1 Reaction products of the reaction n + ^{28}Si below 5 MeV threshold

Reaction products	Threshold (MeV)
^{29}Si + γ	0
^{28}Si+ n	0
^{28}Si* + n	1.78
^{25}Mg + α	2.75
^{28} Al + p	4.00

1.3.2 Photons interaction

Photon is a particle with no mass and no electrical charge. That means, having no charge, the photon does not experience Coulomb forces while it traverses the matter, however it is able to interact with electron through process that will be described below. It is observed that when a photon beam penetrates a layer of material, the intensity of the beam is reduced due to the passage within the material. The attenuation of a monoenergetic photon beam is usually expressed through the exponential attenuation law:

$$I = I_0 \cdot e^{-\left(\frac{\mu}{\rho}\right)\cdot x_m} \qquad \text{Eq. 1.2}$$

where I_0 is the intensity of the beam before penetrating the material, $x_m$is the mass thickness, and $^{\mu}/_{\rho}$ is the mass attenuation coefficient, which depends on the material and on the photon energy. This expression represents the attenuation of a monoenergetic beam from a macroscopic point of view. Then, the mass attenuation coefficient can be correlated to the probability that a microscopic interaction occurs, σ_{tot} (also called total nuclear cross section or microscopic cross section), with:

$$\frac{\mu}{\rho} = \frac{\sigma_{tot}}{u \cdot A} \qquad \text{Eq. 1.3}$$

where u is the atomic mass unit and A is the atomic mass of the target element. The nuclear cross section is expressed in *barn* (10^{-24} cm^2)

So, when a photon beam passes through a material, it undergoes through different processes that attenuate the beam. The total cross section is the sum of the contribution of the processes, and the main contributor effects are:

- Coherent scattering
- Photoelectric effect
- Compton scattering
- Electron-positron pair production

For each effect, the cross section will show a different trend because of the several mechanisms that are involved. So, we will highlight the mechanism of each process. We start from the coherent scattering. It is also called Rayleigh scattering, and during this process, the photons are scattered by the electrons bound to the atom. In this process, the energies of the incident and the scattered photon are the same and only the direction of the photon is modified. For low photon energy the total cross section is:

$$\sigma_{Ray} \approx \frac{8}{3}\pi r_e^2 Z^2 \qquad \text{Eq. 1.4}$$

meanwhile for high energy is inversely proportional to the square of the energy.

$$\sigma_{Ray} \propto \frac{1}{E^2} \qquad \text{Eq. 1.5}$$

The next process is the photoelectric effect. In this process, an incident photon with energy $h\nu$ is absorbed by the atom, meanwhile an electron is

ejected by the atom. The electron will have an energy equal to *hν-B,* where *B* is the binding energy of the electron. The binding energy will depend on the shell where the electron is. The photoelectric effects is dominant for low-energy photons and it decreases for higher energy. In Figure 1.10, we show the photoelectric cross section for the silicon. For energy lower than 0.5 MeV the cross section is proportional to $E^{-\frac{7}{2}}$, meanwhile for energy higher than 0.5 MeV is inversely proportional to the energy *E.*

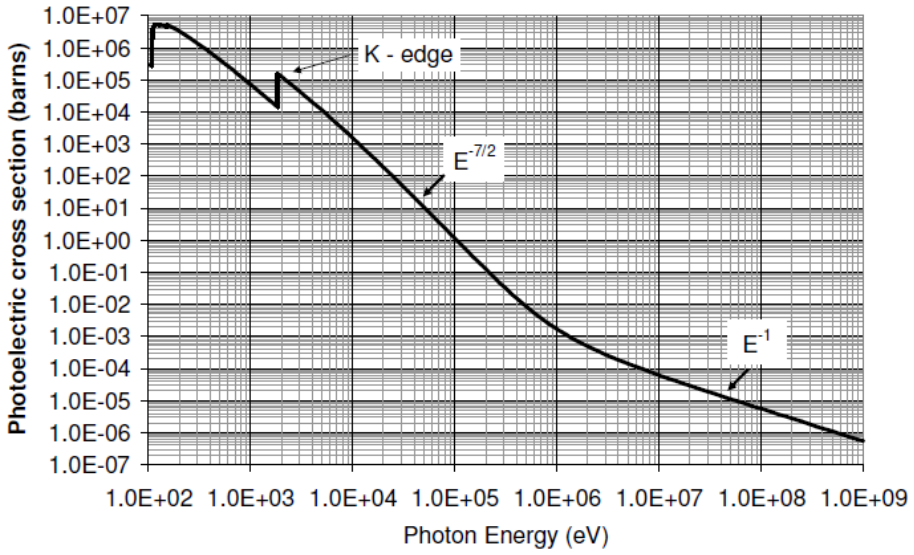

Figure 1.10 Photoelectric cross section for silicon [26].

Instead, Compton scattering is the dominant effect for the intermediate energies. In this case, an incident photon collides with an atomic electron, which is considered to be free and at rest. The effect is the release of a photon of lower energy, with a different angle with respect to the initial one. The difference in energy and momentum of the photon is given to the atomic electron. Nevertheless, using the conservation of energy and momentum allows to calculate the scattered photon energy and the scattering angle. Then, the Compton cross section is calculated using the Klein-Nishina [27] formula:

$$\sigma_{compton} = 2\pi r_e^2 \left\{ \frac{1+\kappa}{\kappa^2} \left[\frac{2(1+\kappa)}{1+2\kappa} - \frac{1}{\kappa} \ln(1+2\kappa) \right] + \frac{1}{2\kappa} \ln(1+2\kappa) - \frac{1+3\kappa}{(1+2\kappa)^2} \right\} \quad \text{Eq. 1.6}$$

where $\kappa = E/m_e c^2$ and it is calculated with the conservation of energy and momentum. However, for low energy, the hypothesis that the electrons is at rest with respect to the photon is not valid anymore. Thus, Brusa *et al*. [28] have taken into account this behavior. For energies lower than a ten of keV, we can see (Figure 1.11) that the cross section is lower with respect to Kleina-Nishina approach.

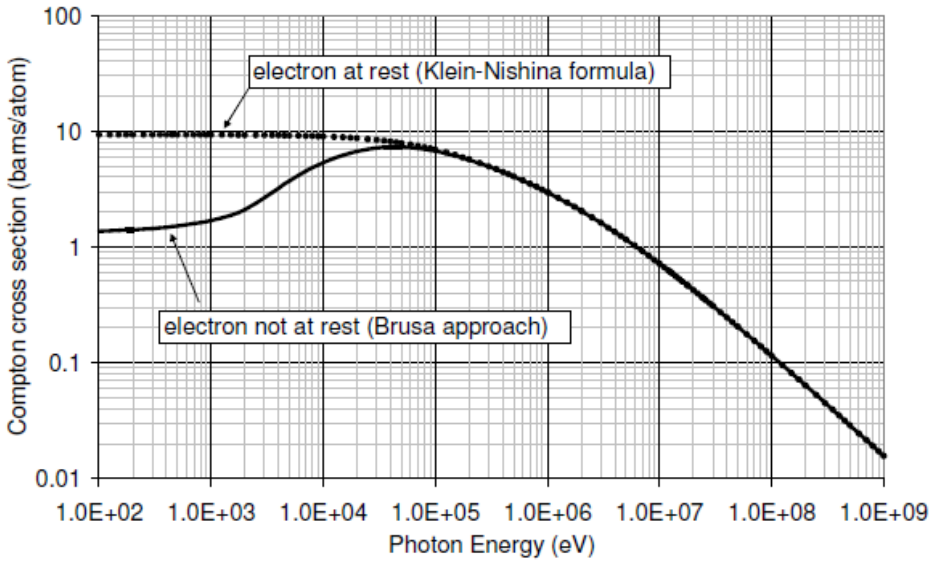

Figure 1.11 Compton cross section for silicon, with the Brusa approach and the Klein-Nishina formula [26].

The latter effect is the pair production. This is an effect that requires an energy of at least twice the electron rest energy ($2m_e c^2$). If the photon energy is higher and it is absorbed in the vicinity of a nucleus (or also an electron, even though, in this case the event is less likely with respect to the nucleus and requires a threshold of $4m_e c^2$), then a pair of electron and positron is created. At low energy the cross section is expressed by:

$$\sigma_{prod} \approx 4\alpha r_e^2 Z^2 \left[\frac{7}{9}\ln(2\kappa) - \frac{109}{54}\right] \qquad \text{Eq. 1.7}$$

meanwhile at higher energy the cross section is almost constant.

In conclusion, photons interact with the matter in many ways. These processes are competitive and depending on the energy, one of these will be predominant. At low energy (below 50 keV), the photoelectric effect is the dominant and the cross section can reach 10^6 barns. Between 50 keV and 15 MeV, the Compton scattering is more relevant, with cross section values of 1-10 barns. Eventually, at higher energy the pair production is the more likely process, with a quite constant cross section of 1 barn. Lastly, the coherent scattering has a lower impact for all the range of energies and then it is usually not considered.

1.3.3 Charged particle interactions

Charged particles (as heavy ions, electrons and positrons) will interact with the charged components of the atom via the Coulomb force. Then, during their passage in the matter, these particles will constantly lose their energy in collisions of different nature. Consequently, the particles will reduce gradually their energy. The total energy loss per unit length is then defined as the *stopping power* and it is given by:

$$Stopping\ power = \left(-\frac{dE}{dx}\right)_{tot} \qquad \text{Eq. 1.8}$$

The unit of the stopping power is the unit of energy over length. Usually, MeV/cm is used. Dividing this value by the density of the target material, the *mass stopping power* is obtained.

$$Mass\ stopping\ power = \left(-\frac{1}{\rho}\frac{dE}{dx}\right)_{tot} \qquad \text{Eq. 1.9}$$

In this case, the units are $MeV.cm^2/mg$. The mass stopping power is convenient because, in the case of gases, it is not dependent on the pressure of the material. These total values will be the sum of the various contributions from all the mechanisms of energy loss. These mechanisms will be different according to the kind of particles. To analyze these mechanism it is convenient to consider the charged particles in two different categories: heavy charged particles, like ions and light charged particles, as electrons and positrons. In the next sections, we will highlight first the mechanism for light particles and then for heavy particles.

Another quantity that is often used, is the *Linear Energy Transfer (LET).* The LET of a material, for charged particle of a given type and energy, is defined as the quotient of the energy deposited by the charged particles in the medium by the length and expressed with the same unit of the stopping power. The difference between the stopping power and the LET is that the first considers the energy lost by the particle, meanwhile the second considers the energy deposited in the medium by the particle. However, generally the LET is considered equal to the *electronic stopping power* (see paragraph 1.3.4), as most of the energy is lost by ionization and thus deposited in the medium. Only in presence of considerable loss by radiative interaction, a difference may arise.

1.3.4 Electron and positron interactions

The interaction of electrons and positrons with the matter is due to four mechanisms:

- Elastic scattering.
- Inelastic scattering.
- Bremsstrahlung emission.
- Cerenkov emission.

During the elastic scattering, the incoming particle interact with an atomic nucleus. Because it is an elastic interaction, the atom will not change its state and will not recoil because of the significant lower mass than electron and

positron. In this interaction, only the direction of the incoming particle is changed. Because of that, this effect will not contribute significantly to the energy loss by the particles.

Instead, in inelastic scattering, electrons and positrons experience the more relevant amount of energy loss and this mechanism is the dominant for this kind of particles. The incoming particle interacts with the atomic electrons and it may ionize or excite the atom. In ionization, the energy of the incoming particle is high enough to knock out an atomic electron from the atom, thus leaving the atom in a ionized state. Meanwhile, if the energy is not sufficient, the atom will be excited, moving an atomic electron to a higher energy level. The total energy loss is usually named *collisional stopping power* and it is calculated using Bethe-Bloch equation in first Born approximation:

$$\left(-\frac{dE}{dx}\right)_{col} = \frac{2\pi k_o^2 e^4 n}{mV^2}\left[ln\frac{mV^2T}{2I^2(1-\beta^2)} - \left(2\sqrt{1-\beta^2}-1+\beta^2\right)ln2 + 1 - \beta^2 + \frac{1}{8}(2-2\sqrt{1-\beta^2}-\beta^2)\right] \quad \text{Eq. 1.10}$$

where $k_o = 8.9876 \times 10^9\ N\,m^2C^{-2}$, e is the charge of the electron, n the density of electrons per unit volume, m is the mass of the electron, T is the kinetic energy, I is the mean excitation energy, V is the speed of the particle and β is the ratio of the speed of the particle and the speed of the light.

The next effect is called bremsstrahlung (from German *bremsen* "to brake" and *Strahlung* "radiation") emission. As the name suggest, this mechanism produce the emission of a radiation (in this case a photon) due to the deceleration of a charged particle, caused by the electrostatic field of the atoms. This process is common to all charged particles but its effect is considered negligible for heavy particles, compared with that for lighter particles, as electrons. In fact, using classical physics, the intensity of the bremsstrahlung radiation, is proportional to:

$$Intensity\ of\ bremsstrahlung \propto \frac{z^4 Z^2 e^6}{M^2} \qquad \text{Eq. 1.11}$$

where ze is the ion charge, Z the atomic number of the target material and M the mass of the incident ion. Considering that the intensity is proportional to the inverse of M^2, for light particles as electrons the intensity of the bremsstrahlung radiation, for the same speed and the same material, is higher with respect to particles with higher mass Z.

The Cerenkov emission is an electromagnetic radiation emitted from a particle traversing a medium at a speed greater than the speed of light in the medium itself. It is usually neglected because its contribution to the total energy loss is very low in comparison with the inelastic scattering and the bremsstrahlung radiation. In fact, the main contributor to the stopping power for electrons and positron are the inelastic scattering and the bremsstrahlung radiation, given by:

$$\left(\frac{dE}{dx}\right)_{tot} = \left(\frac{dE}{dx}\right)_{inel} + \left(\frac{dE}{dx}\right)_{Brem} \qquad \text{Eq. 1.12}$$

Their contribution is dependent on the energy of the incident particle and it can be estimated by using this empirical formula [29]:

$$\frac{(-dE/dx)_{rad}}{(-dE/dx)_{coll}} \cong \frac{ZT}{800} \qquad \text{Eq. 1.13}$$

Thus, as the energy increases the Bremsstrahlung contribution becomes more relevant.

1.3.5 Heavy ions

Heavy ion mechanisms of collision are similar to the electron's, as they are both charged particles, but peculiar differences are present because of the different masses of the particles. Mainly, elastic collisions and inelastic

collisions are the two mechanisms involved in heavy ions collisions. Elastic collisions are similar to the electron elastic scattering. An incident ion interacts with the electrostatic field of the target atom. The main difference is that the incident ion has a mass which is comparable to the target atom, meanwhile in the electron elastic scattering the mass of the electron is largely smaller than the one of the target atom. As a consequence, a significant amount of energy is released to the target ion, that can be ejected and interact in the medium or oscillates in his initial position if the energy is not enough to knock it out. Meanwhile, the target ion is deflected in a different direction from its initial direction and with a lower energy. The stopping power due to elastic collision is usually called *nuclear stopping power.* To calculate it, some semi-empirical formula are used, but nuclear stopping power is generally not relevant until very low energy is reached. In Figure 1.12 [30], we can see the mass stopping power of aluminum ion in silicon, to show that the nuclear contribution is important only for lower energy. That is why, in most applications, just the stopping power due to inelastic collision is considered. This stopping power is also called *electronic stopping power* or *Linear Energy Transfer (LET)*.

In the inelastic collision, the incident ion interacts with the electromagnetic field of an atomic electron. Energy is transferred from the incident ion to the atomic electron, that will leave the vicinity of the atom leaving a vacancy in the atom, creating an electron-hole pair. The first attempt to calculate the electronic stopping power was done by Bohr using a semi-classical approach [31], [32]. In this theory, the atomic electron is considered at rest and free before the collision with the fast ion. The incident ion will pass at a certain distance from the electron.

Also, it is assumed that the ion is negligibly deviated by the impact and it can be considered as proceeding in a straight line. Later, several attempts to include quantum-mechanism have been performed [33] and reaching the final form given by Bethe [34]. Then, his work has been extended to relativistic particles and finally a formulation known as the Bethe-Bloch equation has been obtained. This equation can be written as:

$$\left(-\frac{dE}{dx}\right)_{ion} \approx K \cdot \frac{Zz^2}{\beta^2}\left[ln\left(\frac{2m_e c^2 \beta^2 \gamma^2}{I^*}\right) - \beta^2 - \frac{\delta}{2} - \frac{C}{Z}\right] \quad \text{Eq. 1.14}$$

Where K is a constant related to the medium, z is the charge of the ion, γ is relativistic factor, I^* is the mean excitation energy, δ is the density effect correction to ionization loss, which is relevant for high energy and C is the shell correction term which corrects the assumption that the incident ion has a greater speed than the atomic electron and the other symbols are given in the section 1.3.4.

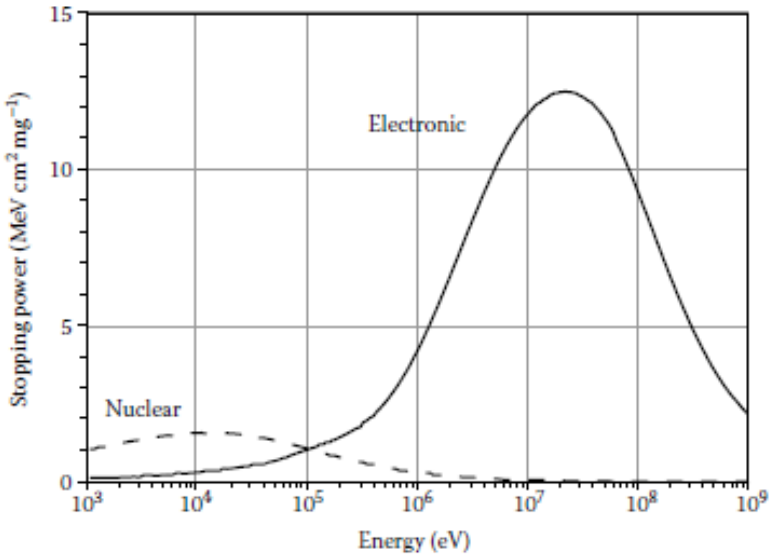

Figure 1.12 Mass stopping power for an aluminum ion in silicon [30].

However, the Bethe-Bloch equation shows some limitations at low energy. In fact, the Bethe-Bloch equation is based on the assumption that the incident ion has a speed greater than the atomic electrons. In addition, at low energy the incident ion may collect electrons and thus modifying his charge and changing his behavior. Then, at low energy the theory of Lindhard and Scharff [35] is used. They have showed that the stopping power in low energy region is a linear function of the ion velocity. Even at intermediate energy, the Bethe-Bloch equation has some limitations. Indeed, at intermediate energy the dielectric theory is used. This theory

considers that the ion modifies the dielectric constant of the medium locally. Eventually, the three theories needed to calculate the stopping power are shown in Figure 1.13. In this figure, the stopping power for a silicon ion in silicon is shown. At high energy, where the Bethe-Bloch equation is used, the stopping power decreases, meanwhile at low energy, where the power law is applied the stopping power increases. At intermediate energy, where the dielectric theory is used, a peak in the stopping power is present. This peak is called the "Bragg Peak". This trend can be found for other ions in other materials [36]. For instance, in Figure 1.14, some examples of stopping power from different ion in silicon are shown [37].

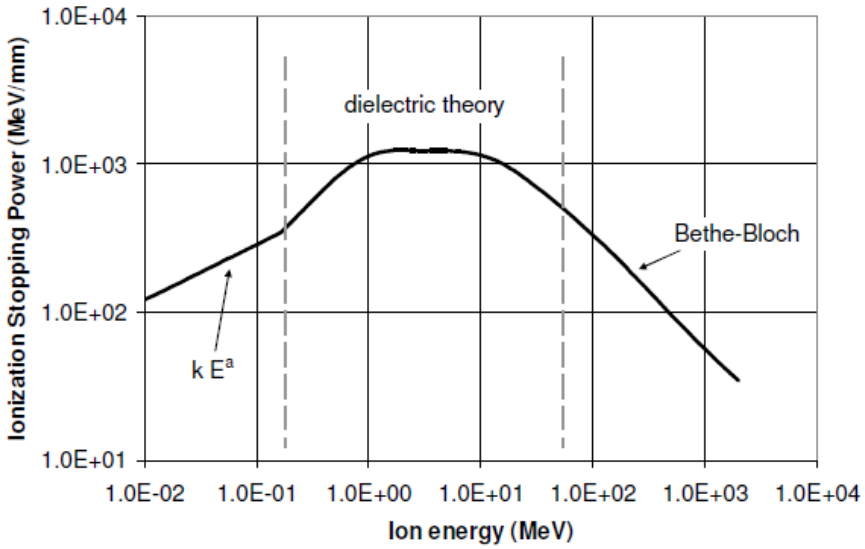

Figure 1.13 Electronic stopping power of silicon ion in silicon [26].

From the stopping power, another important parameter as the range can be calculated. The range is the traveled distance of a particle in a matter until its stopping. It is calculated by:

$$R = \int_0^E \frac{1}{\left(-\frac{dE}{dx}\right)_{tot}} dE \qquad \text{Eq. 1.15}$$

In Figure 1.15, the range of different ions in silicon is shown. From this figure, it can be retrieved that an heavier particle has a smaller range with

respect to a light particle [38]. The reason is that particles with higher Z have an higher LET. Thus, considering Eq. 1.15, an higher LET means a smaller range and this means that heavier particles release most of their energy in a shorter range with respect to light particles.

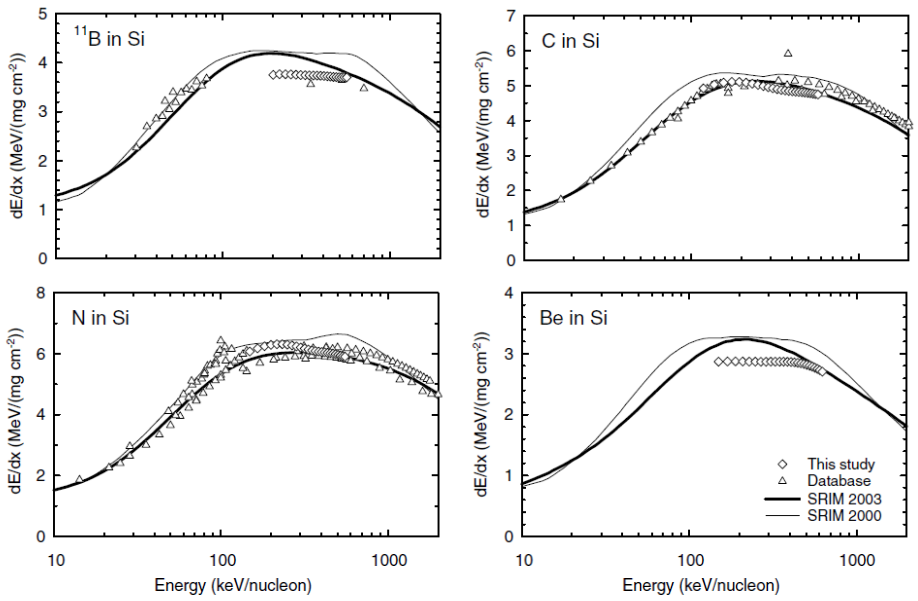

Figure 1.14 Comparison of electronic stopping power of B, C, N and Be in silicon as in [37].

Furthermore, another important information on particle interaction in the matter is the plot showing the LET versus the penetration of the particle in the matter, which is especially used in the radiation effects domain. This allows a better understanding of the effects of the particle inside the device of interest. As an example, we report the plots [Figure 1.16] of the ion cocktail of the RADiation Effects Facility (RADEF), a specialized facility in the study of radiation effects in electronics and related materials [39]. Even in this plot, we can see the characteristics discussed before. An heavier ion as Xenon-131 will have a higher LET but a smaller range with respect to a lighter ion as Nitrogen-15. Moreover, also the Bragg peak (the maximum LET for each curve) can be seen in this plot.

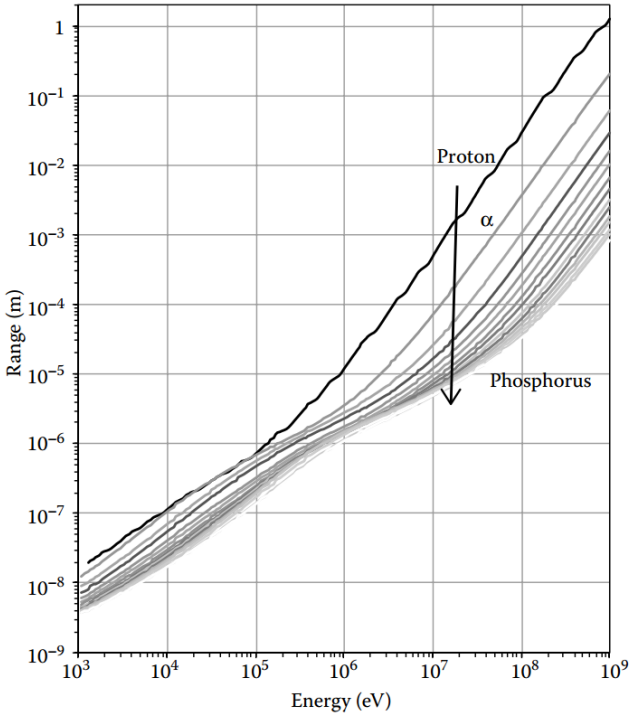

Figure 1.15 Range versus energy for different ions from Z=1 to Z = 15 in silicon [30].

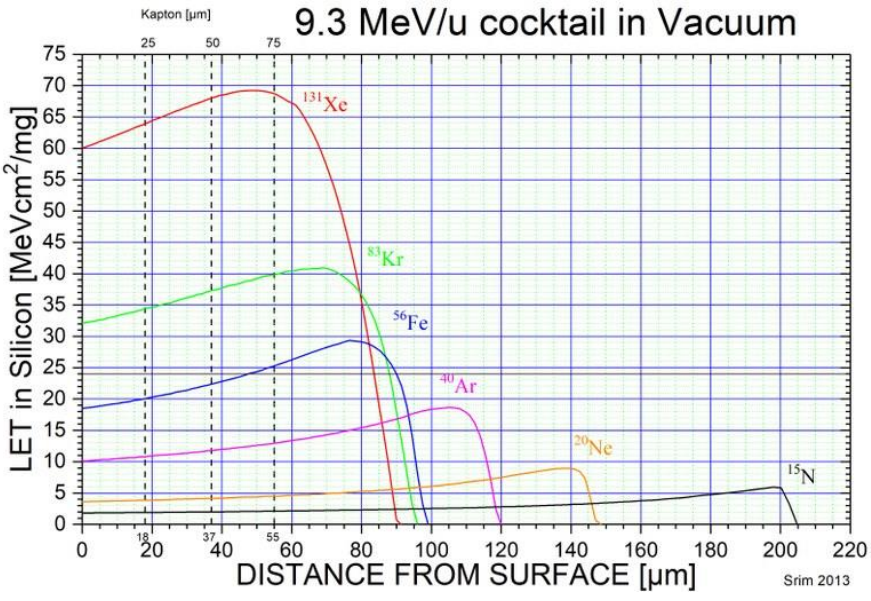

Figure 1.16 LET in silicon the ion cocktail of the RADiation Effects Facility (RADEF), a specialized facility in the study of radiation effects in electronics and related materials [39].

1.4 Conclusion

In this chapter, we have seen how the radiation is different depending on the environment. We have analyzed the different particles and their energies in space, earth and ground facilities. Then, the interaction between the particles and the matter has been presented. Every different particle interacts in different way in the matter, leading to different effects. For instance, in human body, radiation may cause severe diseases. Meanwhile, for electronics, several effects may arises due to the generation of charges inside the electronic devices, or displacement effects.

In the next chapter, we will give a brief introduction on the different radiation effects in electronics and then we will focus our attention on a specific effect, called *Single Event Latchup*. This effect is the main topic of this manuscript.

Chapter 2
Single Event Latchup

Radiation can cause different effects on electronic components. The effect depends on how radiation interacts with the material. There are three main categories of radiation effects: Total Ionizing Dose (TID), that is caused by the accumulation of charge deposited by the radiation; Single Event Effect (SEE), that it is caused by the interaction of a single particle with the device; and Displacement Damage (DD), that is the result of structure change in a semiconductor. For the scope of this work, we are going to focus on Single Event Effects and on a specific SEE, that is Single Event Latchup (SEL).

2.1 Single Event Effects

In the previous chapter, we have analyzed how different particles, as heavy ions, protons, and neutrons interact with the material of the electronic components. During their passage inside the matter, electron-hole pairs are created with the mechanisms discussed in section 1.3. Regardless that, the creation of the pairs leads to different mechanisms that will ultimately cause the Single Event Effects. These mechanisms can be divided in three steps: charge generation by the particles; charge transportation within the device; and charge collection in a sensitive region of the device. The process of creating electron-hole pairs is called *ionization*, and it can be divided in: direct ionization and indirect ionization [Figure 2.1]. During direct ionization, the energetic particle passes through the semiconductor material, and it creates electron-hole pairs. These pairs produce a cascade of secondary electrons, that will create other electron-hole pairs during their thermalization. In this way, almost all the energy deposited by the radiation strike, is transferred to the electron-hole pairs. During indirect ionization a particle that hit the component, it will not interact directly with the electrons of the atoms of the material, and so it will not ionize the matter. However, when they interact with the atoms, they can release their energy to other particles that will cause ionization. These secondary charged particles can deposit their energy as in the direct ionization mechanism and cause the single event effect [40].

Once the electron-hole pairs are created, they will be influenced by the electrical field and the doping condition inside the device. In general, after the pairs are created, they are drifted by the electric field and they diffuse in the semiconductor because of the different concentration of charges. So, the charges will be collected by the electrodes. However, during this process, the charges may recombine inside the matter. Eventually, they will induce a transient current in the device. Depending on the intensity of the current, as well on the characteristic of the device, different type of single event effects can occur.

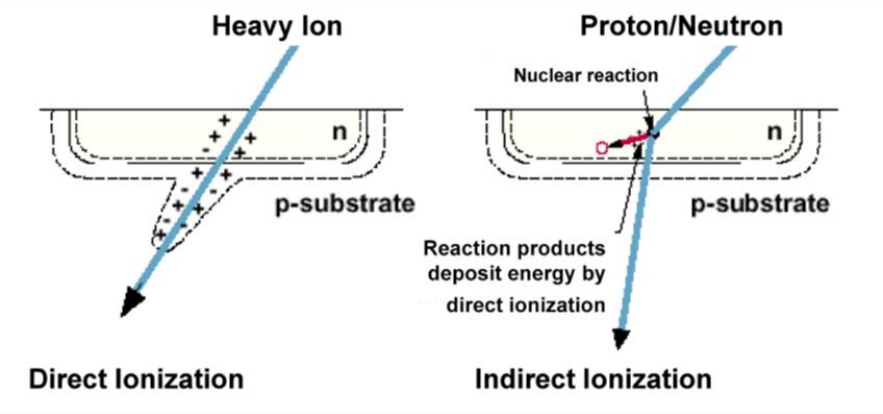

Figure 2.1 Direct and indirect ionization. During direct ionization, the electron—hole pairs are created directly by the incident particle. In the indirect ionization, the incident particle will release its energy to a secondary particles, that will eventually create the electron-hole pairs [40].

These effects are generally classified in two categories: destructive or non-destructive. Actually, many classifications exist and some of these effects can be considered as destructive or as non-destructive. For this work, we are going to use the classification given by the standard ECSS-E-HB-10-12A, released by the European Cooperation for Space Standardization [41]. In the destructive SEE group are usually included:

- Single Event Latchup (SEL) – a potentially destructive triggering of parasitic BJTs which are inherent in CMOS components.
- Single Event Burnout (SEB) – a destructive effect in power transistors, due to the triggering of a vertical n-channel transistor.
- Single Event Gate Rupture (SEGR) – Formation of a conducting path triggered by a single ionizing particle in a high-field region of gate oxide

In the non-destructive SEE group are included:

- Single Event Upset (SEU) – bit-flips that cause a change of the stored information.
- Single Event Transient (SET) – a transient current that can be interpreted as a false signal.

- Single Event functional Interrupt (SEFI) – transient corruption of a control path
- Multiple-cell Upsets (MCU) – single particles affecting several adjacent bits due to large particles ranges.

This is not a complete list of the Single Event Effects and sometimes definitions may be different. For instance, sometimes Single Event Latchup is considered also as non-destructive. In this work, the focus in on Single Event Latchup. As aforementioned, it affects CMOS components and can be potentially destructive for them. In the next chapters, we are going to discuss his triggering mechanism, state of the art and how to simulate it.

2.2 Single Event Latchup

Latchup arises from PNPN structures that are inherently present inside CMOS. It can occur from different types of electrical and current responses (electrically induced Latchup), and it can occur from single particles (heavy-ions, protons, etc.) collision (radiation induced latchup). Even though they have the same final outcome, their triggering mechanism and dynamic behaviour are different [42]. Indeed, electrically induced latchup involves surface or bulk currents which are spread over broad regions of the device, meanwhile radiation induced latchup involves a localized region around the radiation track [43]. In this work, our focus is on radiation induced Latchup, also called Single Event Latchup.

The first evidence of radiation induced latchup was found in the early 60s by Leavy and Poll [44]. They have observed Latchup in bipolar transistors, due to radiation. Later, Gregory and Shafter [45] showed that latchup is obtained also in CMOS integrated circuits, if exposed to radiation. Eventually, in the mid-1980s single event latchup was a well-known effect and his characteristics were later studied more deeply [45]. In the next paragraph, we will describe the basic structure that is needed for the SEL, the dynamics of SEL, his temperature dependence and the influence of geometry and design on Single Event Latchup sensitivity.

2.2.1 SEL: basic structure and electrical characteristics

CMOS is the main device to suffer Single Event Latchup. This is due to the presence of parasitic bipolar transistors and their triggering is responsible for the Single Event Latchup. As explained in [46], parasitic transistors are inherently fabricated inside the CMOS device. In Figure 2.2, it is shown the basic CMOS inverter structure and the parasitic bipolar transistor created inside it (LT1, LT2, VT1, VT2). There are vertical PNP bipolar transistors formed by the P+ source or the P + drain diffusion, the N-well and the P-substrate. Also, there are lateral NPN transistors formed by the N+ source or drain diffusion, the P-substrate and the N-well. From it, an equivalent electrical circuit can be designed. It is formed by a MOS part and by a portion formed by the parasitic transistors [Figure 2.3].

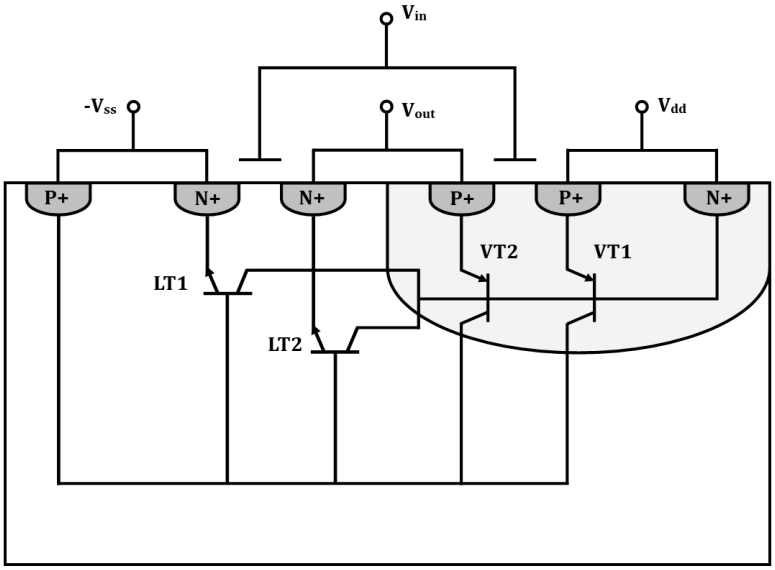

Figure 2.2 Parasitic bipolar portion of N-well CMOS inverter [46].

However, the Latchup behavior of the inverter depends on the V_{out}. Depending on its value, one of the four transistors will be off. Also, it has to be considered that, the emitter current of VT2 and LT2 [see Figure 2.2], is limited, meanwhile in LT1 and VT1, current is supply by the power source, so it has no limitations. Then, the combination of LT1 and VT1 is the more

susceptible to sustain Latchup when it occurs [46]. For this reason, when Latchup is studied, instead of considering the full CMOS inverter structure, only the PNPN structure is investigated. Certainly, for more complex devices with several CMOS components, Latchup paths can be numerous.

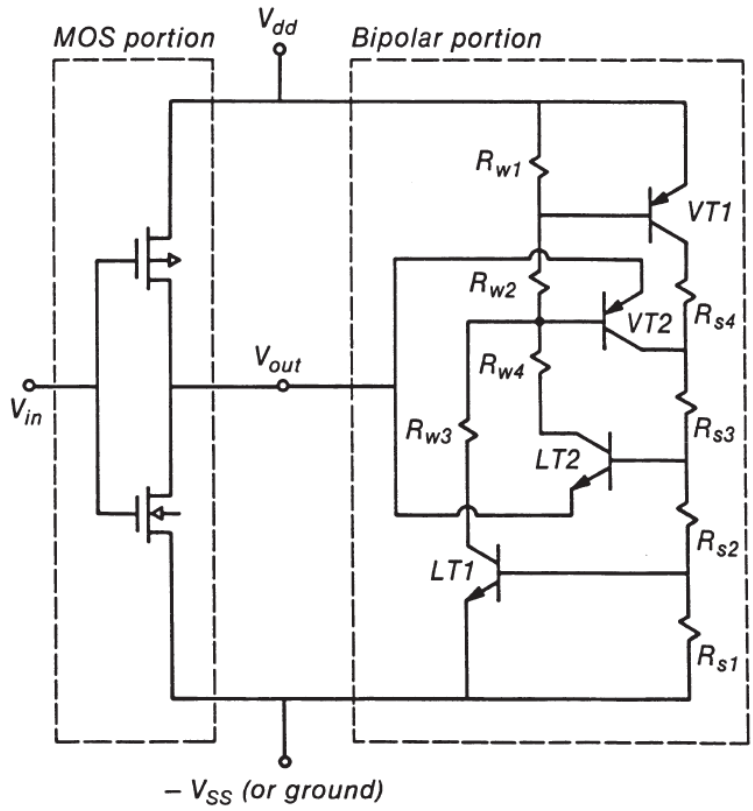

Figure 2.3 Complete circuit schematics for N-well CMOS inverter [46].

Nonetheless, Latchup (both electrical and radiation induced) triggering is still caused by one of the basic PNPN structure which are present inside the device. This structure includes the P+ and N+ sources and the N-well and P-substrate terminals [Figure 2.4]. The PNPN structure is formed by a lateral PNP transistor and NPN transistor. The PNP is a vertical BJT formed by the P-source (emitter), the N-well (base) and the P-substrate (collector) and the NPN is a lateral BJT formed by the N-source (emitter), the P-substrate (base) and the N-well (collector). This is valid both for electrically induced Latchup and radiation induced Latchup. In normal condition, the PNPN is in a high impedance state and so it can be neglected. However, if this portion enter into a low impedance state, a current can pass through this circuit. If the

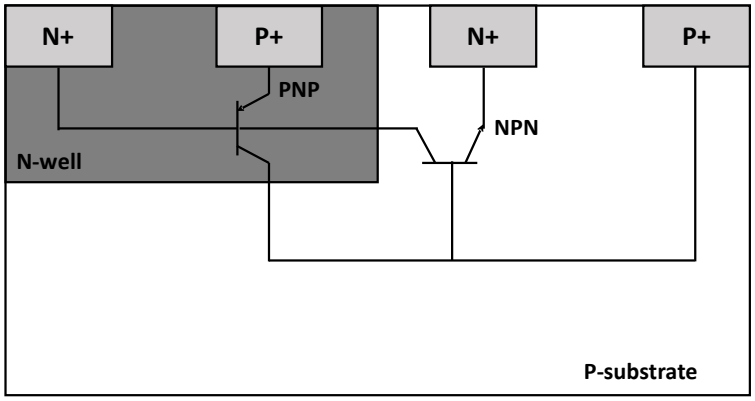

Figure 2.4 PNPN structure with the relative parasitic transistors.

current is not limited, its rising can reach dangerous level for the device itself. This behavior can be understood with the I-V curve of one of the PNPN thyristor there are formed by the PNP and NPN transistors [Figure 2.5]. In Figure 2.5, it is shown the low impedance region, which is delimited by two points, respectively called *triggering point* and *holding point*. These points are identified by triggering current and voltage (I_{trig}, V_{trig}) and holding current and voltage (I_{hold}, V_{hold}). The triggering point represents the switching point between the high impedance region and the low impedance region. Meanwhile, the holding current and voltage are the minimum conditions required to sustain Latchup, regardless the triggering mechanism [43].

In order to study the latchup, several models have been used in the past [42], [47]. The most known approach is the one presented in the work of Bruguier and Palau [42]. In addition to the PNP and NPN transitors, the resistors of the well and substrate are added. Specifically, R_{BW}, R_{EW} and R_{CW} are the well resistors of the base, emitter and collector respectively, meanwhile R_{BS}, R_{ES} and R_{CS} are the substrate resistors [Figure 2.6]. A development of the model proposed by [42], has been proposed by Al Youssef *et al.* [48]. In this work, the authors claim that the old model is limited because there is no real modeling of the intrinsic behavior of the parasitic transistors. In their model, they consider R_{EW}, R_{CS}, R_{BW} as internal resistors of the pnp transitor and R_{CW}, R_{ES}, R_{BS} are the internal resistors of

the npn transistor. In addition, the zone between the PNP and the well contact is represented by the resistor $R_{N\text{-extension}}$ and vice versa $R_{P\text{-extension}}$ represents the zone between the NPN and the substrate contact [Figure 2.7].

These models can be used for electrical simulations as in SPICE (see section 3.2). In this work, we have developed our schematic circuit to simulate SEL and we will discuss it in Chapter 5.

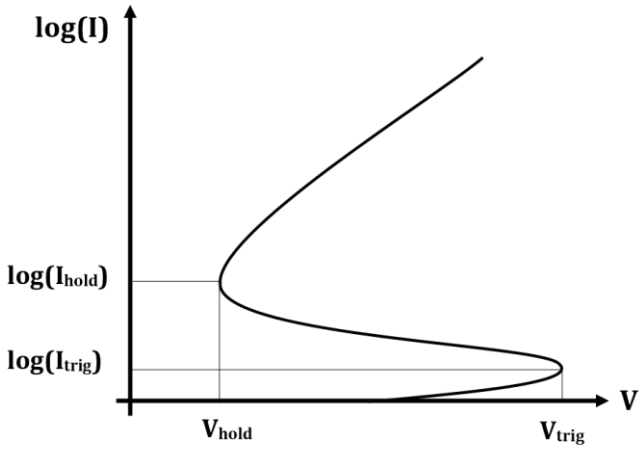

Figure 2.5 I-V characteristics of the PNPN structure [46].

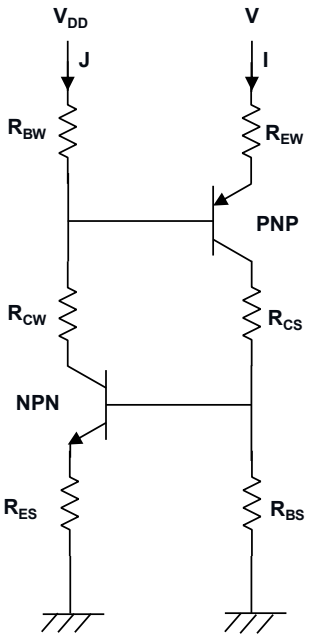

Figure 2.6 Schematic circuit of the PNPN structure as in [42]

2.2.2 SEL: triggering dynamics

Starting from the PNPN structure, we can now analyze triggering mechanism for Single Event Latchup. Generally, SEL can be triggered by the anode (the P+ contact), that turns on the vertical transistor PNP, or by the cathode (the N+ contact), that turns on the lateral transistor NPN. However, anode triggering is more likely than cathode triggering, as less charge is needed to trigger the vertical transistor with respect to the lateral one [49].

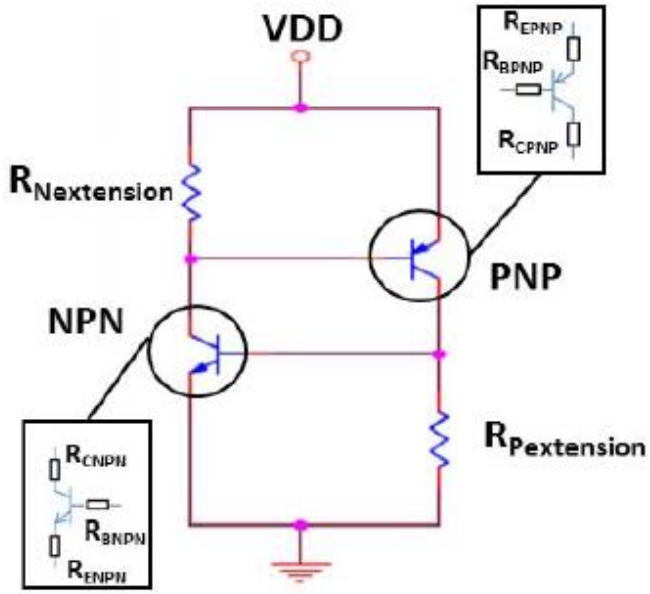

Figure 2.7 Schematic circuit of the PNPN structure as in [48]

We will analyze now the triggering mechanism according to [42], [43], [50]. In all these works, a particle hitting the n-well is taken as a reference. When a radiation particle strikes the structure, electron-hole pairs will be created through its passage. These pairs will drift towards the positive and negative potential sides [50], such that a current flows in the N-well. As the current flows, the potential of the N-well is reduced. Then, the potential at the N-well is not V_{DD} anymore. If the potential drop is sufficiently large, the vertical PNP transistor will be activated [43]. This step is clearly visible in Figure 2.8. In Figure 2.8 (a), it is shown the electrical potential before the strike. The potential is almost uniform in the N-well. In Figure 2.8 (b), the

electrostatic potential after the strike is shown. The electrostatic potential is reduced, so that the PNP transistor is triggered. Once the PNP is ON, holes are injected into the P-substrate. After that, the PNP tend to turn off because the electron base current is supplied by the electrons generated by the ion.

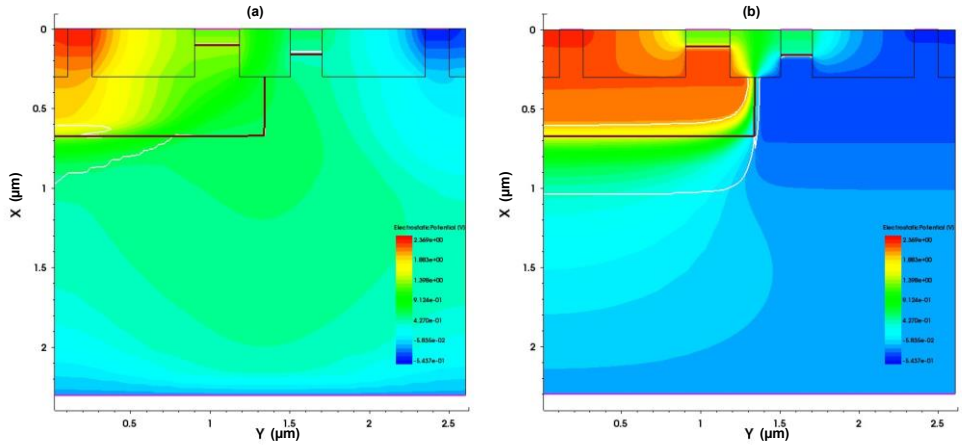

Figure 2.8 Electrostatic potential inside the PNPN structure. In (a) it is shown the electrostatic potential before the ion hits, in (b) it is shown the electrostatic potential after the strike. Simulations are performed with Sentaurus Synopsys.

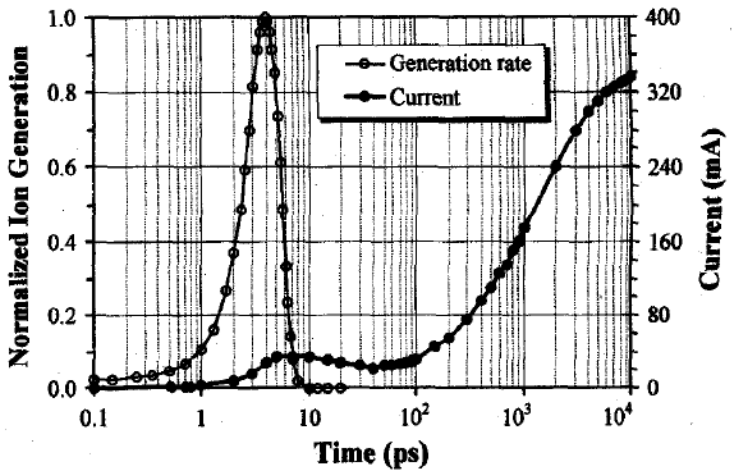

Figure 2.9 Latchup current at Source terminal and generation rate versus time as in [46]

This can be seen in Figure 2.9. At around 30-40 ps, a decrease in the current is visible, meaning that the PNP is turning off. However, the holes injected in the substrate are collected by the P-substrate terminal. If the resistance of

the substrate is high enough, the current will generate a potential change that will activate the NPN transistor. This is shown in Figure 2.10. The authors showed that the substrate potential increases, so to activate the NPN transitor. With the activation of the NPN, the PNP will be sustained by the current coming from the NPN. Once the transistors are sustaining each other, they saturate and will sustain the current at the terminals until the power supply is cut off. When this condition is met, a Single Event Latchup occurred to the device.

However, analysis of the dynamics of Single event Latchup are often not complete and miss some information. In Chapter 5, we will discuss deeper the dynamics of SEL.

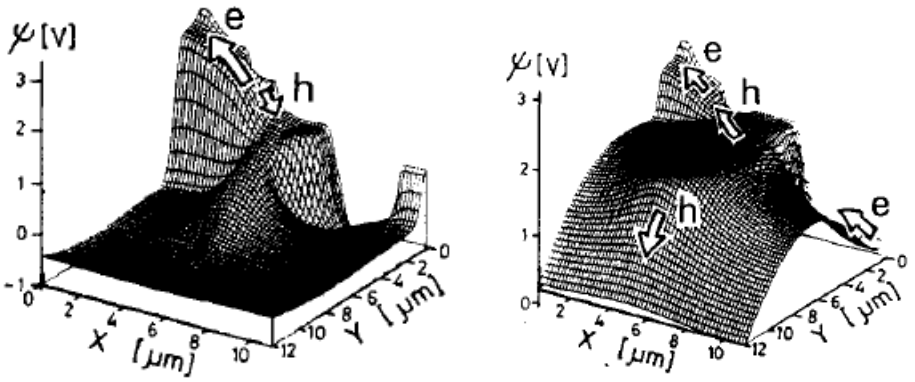

Figure 2.10 Potential increase in the substrate, before and after activation of the NPN transistor [50]

2.2.3 Effect of the temperature on Single Event Latchup

The next step on Single Event Latchup investigation is to highlight which parameters influence its sensitivity. The first parameter to mention is the temperature. Many works on this are present in the literature [51]–[55]. In general, it is known that an increase of temperature leads to a decrease of SEL sensitivity. However, this is not completely true. A first study on that was perform by Iwata and Ohzone [51]. Their work consisted in 2D simulation of a CMOS structure over a temperature range of 77-450 K. The simulations were performed with three different incident strikes: two

perpendiculars with different charge generation and one with a 45°-degree angle. The SEL threshold was calculated, defined as the minimum V_{DD} required to induce SEL. It has been found that, even though immunity decreases as temperature increases, this behavior reaches a peak around 120 K and decreases very rapidly as the temperature becomes less than 120 K. In Figure 2.11, it is shown this behavior for the three incident types. The authors of this work try to explain this behavior with the analysis of the ohmic potential drop and the potential barrier at the P-source after the ion strike. By calculating the built-in potential, the resistance and the current, the potential barrier resulted in 0.38 V for 77 K, 0.47 V for 120 K, 0.40 V for 300 K, and 0.37 V for 450 K. So, the barrier is the largest at 120 K and then it means that the Latchup threshold is higher as expected from the results they have obtained. Recently, this aspect has been investigated further. In 2010, Marshall *et al.* [53] reported the first observation of a SEL at cryogenic temperatures. Their conclusion is that the charges generated by the ion strike can initiate a shallow level impact ionization process (SLII). This process creates a large current flow and creates the condition to sustain a SEL. This conclusion has been obtained also in the paper of Al Youssef *et al.* [56] in which they combine TCAD simulation and experiments. The result is the relevance of SLII mechanism in SEL at cryogenic temperatures.

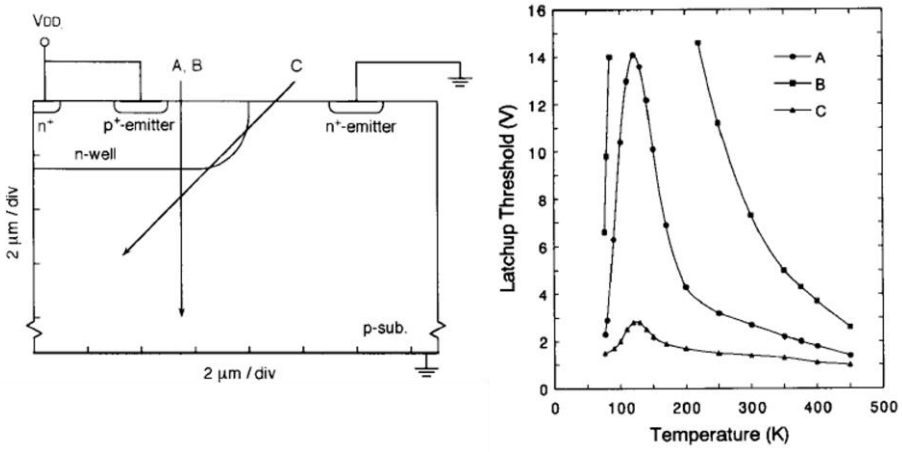

Figure 2.11 The Latchup threshold V_{DD} as a function of temperature for the three different strikes types [51].

Another aspect to consider is the impact of temperature on well and substrate resistances. This aspect has been investigated by Hutson [57]. He shows that by increasing the temperature, the voltage drops needed to turn on the parasitic transistor decrease with increasing temperature. Consequently, a lower current is needed in order to trigger the PNP transistor and therefore, a lower voltage is required to sustain SEL. Furthermore, as the temperature increases, well and substrate resistances increases. This means that for the same amount of current, a larger voltage drop will be caused, and this will lead to an increase in SEL vulnerability. This behavior is clearly visible in Figure 2.12, where the current versus the emitter-base voltage is shown.

Nonetheless, temperature affects many other parameters. In the work of Johnston *et al.* [55], the impact of temperature on factors that affect triggering of SEL is analyzed. Generally, the most affected is resistivity, that we have already highlighted. Then other physical parameters are affected by temperature. Lifetime of electron-hole pairs is also impacted, as the diffusion constant. In the Table 2.1, the results of [55] are shown.

In conclusion, temperature plays an important role in SEL sensitivity. Unfortunately, most of the time temperature cannot be chosen by the designer, but it is a requirement given by the mission or in general by the application of the device. In the next paragraph, mitigation techniques used to reduce SEL sensitivity are presented.

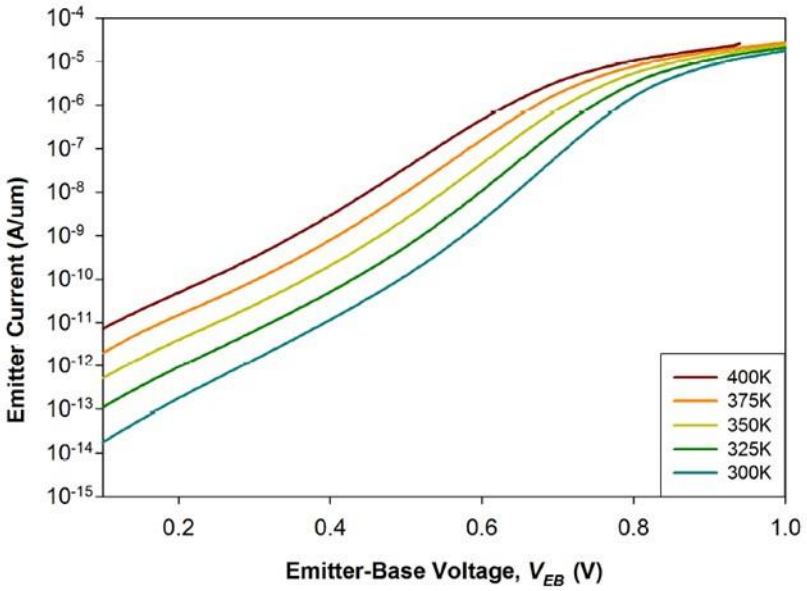

Figure 2.12 Current versus voltage curve for an emitter-base junction [52].

Table 2.1 Temperature-Dependent parameters [55]. The ratio is given by the value of the parameter at 125° C and at 25° C.

Parameter	Ratio (125° C/25° C)
Substrate resistivity	2
Well resistivity	2
Forward voltage drop	0.7
Lifetime	1.2-2
Diffusion constant	0.55
Transistor gain	2

2.2.4 Single Event Latchup mitigation techniques

In the previous paragraph, we have discussed the influence of temperature on SEL sensitivity. Unfortunately, temperature cannot be used as a parameter to make the device more hardened. In fact, its value is mostly related to the working condition of the device. Then, to create a more robust device, other techniques have to be considered. These techniques may involve the process stage or the design stage. Regardless the technique, every method will bring some drawbacks and then, a tradeoff must be done to choose the most appropriate method. In this paragraph, we are going to highlight some of the techniques used for SEL hardening.

Silicon on Insulator (SOI) is a technology fabrication of semiconductor devices in a layered silicon-insulator-silicon substate. In Figure 2.13, there is an example of CMOS SOI Technology. This technology has been reported as completely immune to SEL in previous works [58], [59]. The reason is the decoupling of the PMOS and the NMOS transistors, that means no PNPN path can exist. However, depending on the SOI process used, the decoupling may not happen [Figure 2.14]. Dodds *et al.* [60] have performed heavy ion test on SOI CMOS of this kind. They have demonstrated that SEL can occur in SOI if the transistors are not dielectrically isolated.

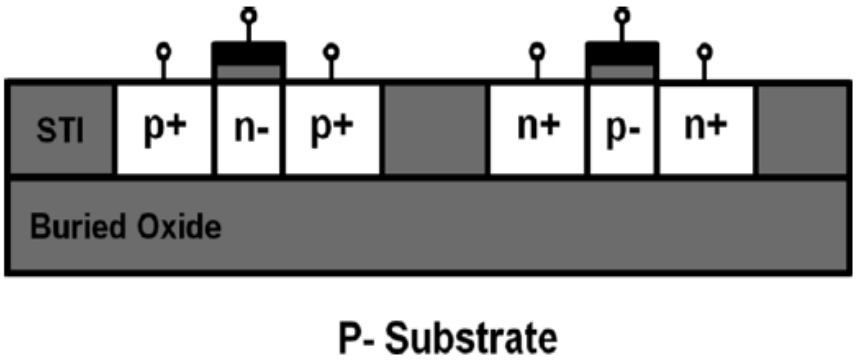

Figure 2.13 Cross setion of a floating-body CMOS SOI technology [60].

Also, triple well technology has been analyzed in Dodds' article. This is another technique for Single Event Latchup hardening [61], [62]. Usually,

the triple well technology consists in a n+ or p+ buried layer in a p or n substrate, respectively [Figure 2.15]. It has the same configuration of dual well structures, with a deep N-well layer in addition. With respect to dual well, triple well can be implemented without area penalty, which makes it attractive for single event Latchup hardening. In the literature [61]–[63] it has been claimed that triple well structures are more robust with respect to dual well. This has been confirmed by Dodds, which performed neutron and laser experiments. The reason is that the presence of the deep N-well layer reduces the capability of the PNP transistor to collect charges, because it removes them more effectively than dual well structures.

Lastly, even doping profile has some impact on SEL. The P-well doping profile influences the substrate resistance. Meanwhile, the N-well doping profile impacts the N-well resistance. A high value of concentration of those will reduce SEL sensitivity. According to [64], the P-well doping profile impact sensitivity more than the N-well.

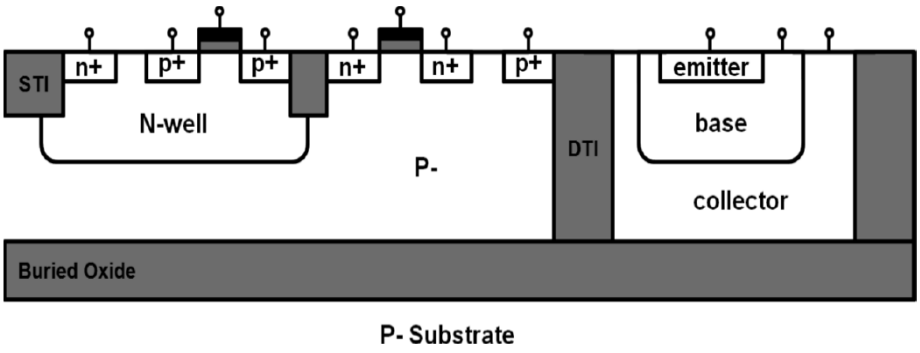

Figure 2.14 Cross section of a BiCMOS SOI technology [60].

These techniques involve process manufacturing of the device. But, when changing the process is not possible, other techniques are used. Mainly, design practices are employed to harden the component. One of these is the implementation of guard rings. They provide electrical and spatial isolation between the transistors and they act as a carrier sink, helping to remove the ion generated charges. According to Dodds [60], devices with guard rings have been tested and resulted immune to SEL. In their test, they have shown that a single guard ring can be used, also

considering that this leads to a lower area penalty with respect to dual guard rings.

Furthermore, a practice which is often used is to increase the distance between anode and cathode. With this method, the gain of the transistors is reduced as it has been proven experimentally by Voldman *et al.* [65]. Some results have been published by Rezzak and Wang [64]. In their study they have analyzed the LET threshold for single event Latchup for different value of spacing between the anode and the cathode. Increasing the distance leads to a more robust device and so to a higher LET threshold. Well and substrate taps placement is also a layout technique that can be used for SEL mitigation. In this case, when taps are placed closer to each other, the resistances of the parasitic transistor will be reduced. In this way, reducing this distance will increase SEL immunity.

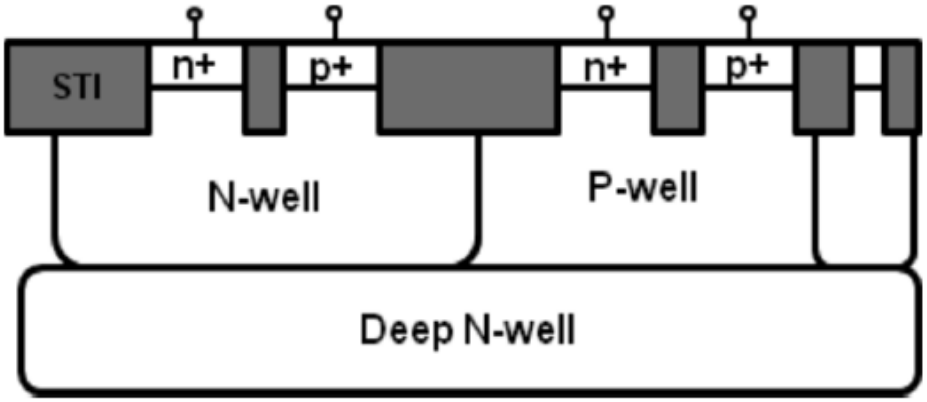

Figure 2.15 Cross section of triple well CMOS technology [60].

In the work of Rezzak and Wang, they concluded that well taps placement is more effective with respect to anode to cathode spacing, because of less area penalty. However, they have highlighted that the best technique must be chosen in accordance with the design. This is true for every technique we have reported. Every solution must be chosen carefully, depending on the scope of the device and on the process used for manufacturing.

2.3 Conclusion

In this chapter, we have presented Single Event Effects and, in more detail, Single Event Latchup, which is the topic of this dissertation. We have shown the parameters that influence SEL sensitivity and which are the techniques used to mitigate its effects. In the next chapter, we are going to present the results of TCAD simulations on the effects of doping profile, anode to cathode spacing and well-ties distance on Single Event Latchup sensitivity.

Chapter 3
Simulation tools

The effects of radiation on electronic components can be studied in two ways: by performing experiments in radiation facilities or by performing simulations, using the different tools available. Understandably, experiments allow to obtain results from real life component in real environments. For these reasons, they are mandatory for qualification or validation of the components. No electronic components can fly in space without being tested before. However, experiments are limited by the cost, the time, and the access to facilities. In fact, experiments have to be performed in specific radiation facilities. Thus, they have a cost and they have a limited access time. The cost can be relatively expensive and limited access time requires to perform the experiments in a specific time. Then, if a problem comes up, it can be solved only in the next access to the facilities, slowing down the process.

Meanwhile, simulations do not have these limitations. They can be used at any time, with a limited amount of investment for equipment (e.g. servers, computers). Moreover, simulations allow to perform destructive experiments, with no need for replacement. Also, they allow to investigate thoroughly a component, in a way that real life experiments do not permit. Internal parameters as charge generation, or charge diffusion can be investigated extensively with simulations. Of course, simulations have some drawbacks. Simulations use mathematical models to replicate the behavior of the actual physical phenomena. Hence, simulations are highly dependent on the model that are used. Furthermore, mathematical models calculation comes with errors and they can lead to misleading results. All that considered, simulations lead to an approximation of the reality. However, in the trade-off between simulations and experiments, the accuracy of the simulation can be high enough to overcome his drawbacks and to be preferable to experiments in certain stages of the study of a component or device.

From the beginning, Single Event Latchup has been studied with simulations. Of course, there exist different kinds of simulations. Here, we will highlight two of the main simulation tools that have been used to study Single Event Latchup: Technology Computer Aided Design (TCAD) tools and Simulation Program with Integrated Circuit Emphasis (SPICE) tools. Specifically, we will describe the main TCAD tools used in this work, Sentaurus Synopsys and ECORCE. We will provide an overview of the software, giving an insight on the preparation of a simulation experiment. We will discuss the main physical models available in the TCAD tools and the ones we used in our work. In this way, we want to give an indication of the tools and the physical model to use when Single event Latchup is involved.

3.1 TCAD

TCAD tools are software used to develop and optimize semiconductor technologies and devices. They model the behavior of semiconductor devices using the governing equation of semiconductor physics, as the continuity and Poisson equations. A typical TCAD software is composed by four parts (Figure 3.1): a process simulator, a device simulator, a plotting tool and a graphical user interface (GUI). The process simulator is used to create the device of interest, by modeling the different steps that are involved in semiconductor fabrication. Once the device is defined, it is used into the device simulator. In this step, the electrical, optical and thermal characteristics of the device are calculated by solving their governing equations. Usually, device simulators use 2D/3D finite element analysis to solve these equations. The finite element analysis allows to solve the differential equations that governs the phenomenon. In fact, the differential equations cannot be solved in a continuous medium. What is necessary, it is to divide the medium into smaller parts, called finite elements. Generally, these elements are geometrical shapes (i.e. triangles). By combining these elements, a structure called “mesh” is created (Figure 3.2). At each node of the mesh, the physical characteristics are applied. Then, the differential

equations are solved by mean of numerical methods. Because of the mesh, an important aspect to consider is the optimization of the simulation. A narrow mesh would produce more accurate results, whilst increasing the computational load. Vice versa, a broader mesh would lead to a reduction of computational load but also to a lower results accuracy. Thus, the mesh can be more dense in the area of the device where there are large variation of quantities (for instance, the junctions) and less dense where the characteristics are less variable. The results obtained by the device simulator are visualized in a plotting tool, where values can be analyzed at the electrode, or they can be evaluated in any point of the device. Results can also be exported to be analyzed with other tools. Eventually, TCAD tools usually provide a GUI in order to allow the user to interact with the different software easily.

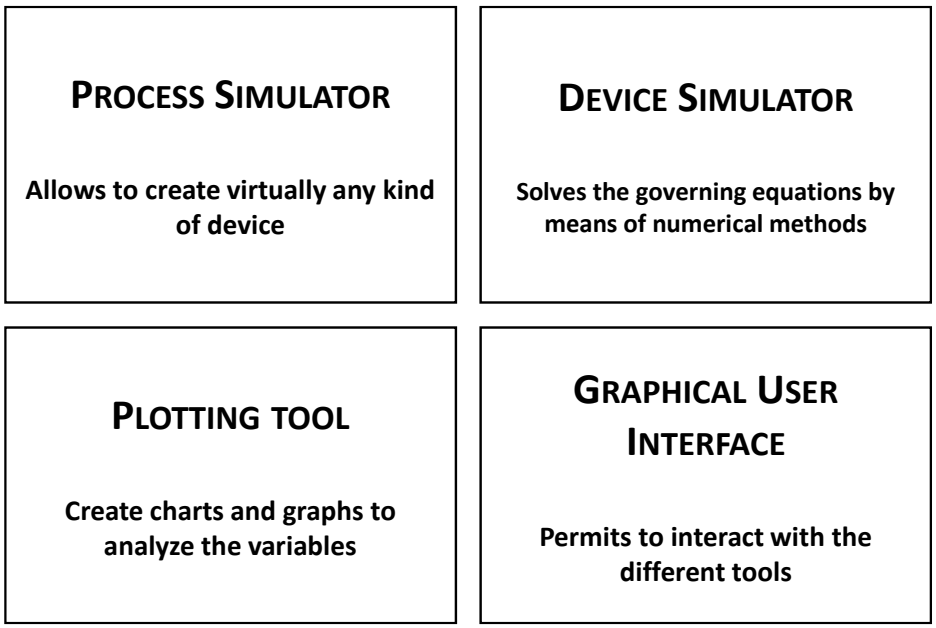

Figure 3.1 Typical TCAD components.

Historically, TCAD tools were born in the early 1970s. At first, a 1D approach was sufficient to deal with bipolar technology and early MOSFET technology [66]. Soon, simulations tools were made publicly available, such as CADDETH from Hitachi, SEDAN from Stanford University and MINIMOS from Vienna, even though these tools were dealing with specific effects,

respectively. With the increasing scaling of MOS technology, 1D approach soon became obsolete and not able to keep up the pace. Then, 2D approach became indispensable to simulate the process stage of this technology and to take into account the phenomena that appears with increasing scaling. Then other tools were developed, like PISCES II from Stanford University, DEVICE from AT&T Bell Laboratories and many more. Furthermore, these software have been further developed to perform 3D simulations. This has been necessary due to the increase of complexity of integrated circuits and due to the continuous downscaling of the technology.

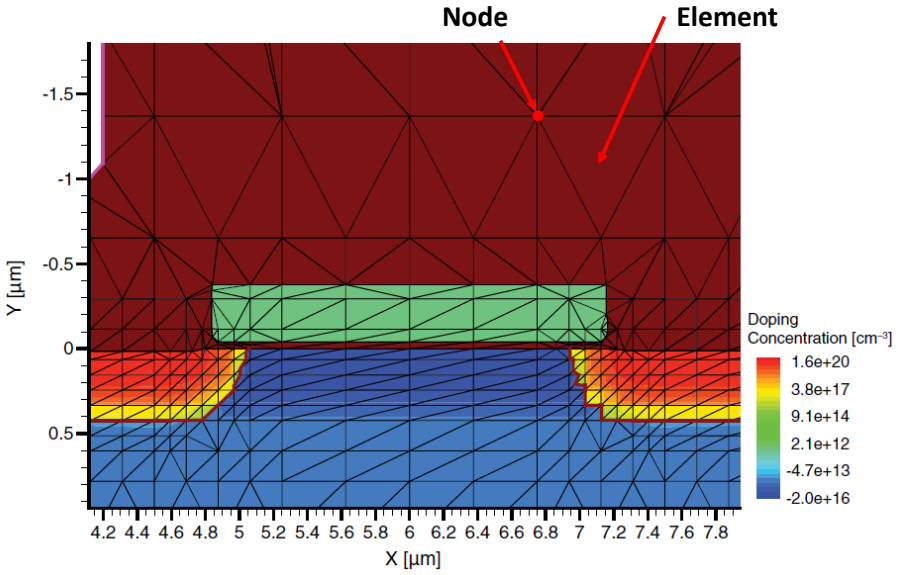

Figure 3.2 Mesh on an NMOS structure, where the node and the finite element are highlighted.

TCAD simulations have been used extensively for Single Event Latchup, both in 2D and in 3D. Many works have been already cited in this dissertation. Aoki [50] have used a 2D simulator named TRANAL to investigate the influence of different epitaxial wafers on Latchup sensitivity. He also investigated the dynamic of Single Event Latchup in PNPN structures. De la Rochette *et al.* [67] analyzed the effects of layout modification on Latchup triggering with the software called MEDICI. This aspect has been investigated also in early days by Hutson *et al.* [57] using Sentaurus. Also, Rezzak and Wang [64] investigated this aspect, considering

doping profile, well-ties distance and A-C spacing, with a 3D simulator developed by Robust Chip Inc.

Nowadays, two main commercial TCAD tools exist produced by Synopsys [68] and Silvaco [69]. Each tool contains the software dedicated to a particular aspect of the device, as depicted in Figure 3.1. For instance, the Silvaco Tool is composed by: ATHENA, process simulator; ATLAS, a 2D and 3D device simulator; VictoryProcess and VictoryDevice, a 3D process and device simulator. By combining these software, it is possible to predict the impact of process parameters on circuit characteristics and to perform simulation related to radiation effects, or electrical simulations in general. The other main software in TCAD has been developed by Synopsys and named Sentaurus and it will be discussed in the next section.

3.1.1 Sentaurus Synopsys

The base of this software was created in 1992, when it was known by the name ISE. At that time, the 1D and 2D process simulators TESIM and DIOS have been developed. Later, Synopsys, a company based on Mountain View, California, bought the software and rename it as Sentaurus. Nowadays, Sentaurus includes software for 2D and 3D process, device and system simulations and its application ranges from deep-submicron component, to optoelectronics.

Normally, a simulation flow in Sentaurus will include the steps shown in Figure 3.3. The first software which is used is **Sentaurus Workbench (SWB).** It includes a toolbar and a graphical interface for establishing and organizing the technical process flow [70] [Figure 3.3]. In the SWB, the user organizes the workflow of the experiments. Here, the user defines the other Sentaurus tools to be used (e.g. for process, for meshing), and sets the variable and the parameters of the simulations. The next software is **Sentaurus Device Editor (SDE).** It is the tool that creates the device geometric structure. It allows 2D and 3D structures. The drawing of the geometric structure can be done by script or by graphical interface. Once the structure is defined, meshing is necessary. In Sentaurus, meshing can be

done in two ways. First, it can be done directly on SDE. In this case the Device Editor will handle the meshing process. Otherwise, the tool **Sentaurus Mesh (SNMESH)** can be used.

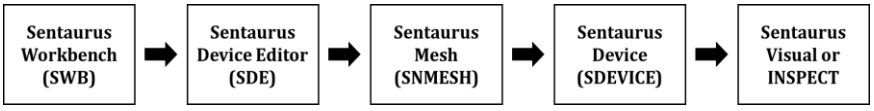

Figure 3.3 Flow of simulation tools by Sentaurus Synopsys.

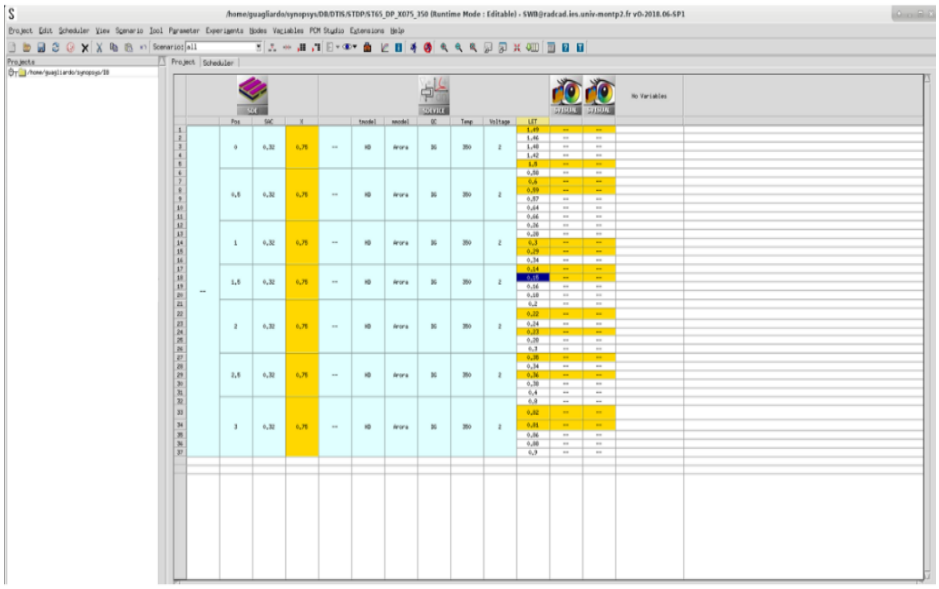

Figure 3.4 Sentaurus Workbench graphical user interface.

Once the device geometry is defined and the mesh has been created, the generated files are passed to the device simulator **Sentaurus Device (SDEVICE).** This simulator allows to perform simulation of memory devices, power electronic devices, optoelectronic device and more. In this tool, the user will define all the physical condition of his experiment, such as biasing condition, temperature, or radiation. All these inputs are contained into a command file. This file is divided into different sections:

- **File:** the input/output files needed for the simulation are specified here;
- **Electrode:** is used to defined the electrodes of the device and the initial condition;

- **Physics:** One of the most important section is the Physics section. In this part, the physical models to be applied are defined. The models are related to the charge transport, mobility, generation-recombination, etc. More details are provided in the section 3.1.1.1;
- **System:** because additional external circuitry can be included in the simulation, it is possible to add it to the System section of the command file;
- **Plot:** it defines which quantities to save and thus be plotted with the other tools;
- **Math:** in this section the user can defined the numerical methods to use to solve the set of differential equations;
- **Solve:** here the user defines the kind of analysis to perform. There are two main type of analysis: *Quasistationary* and *Transient*. In *Quasistationary* simulations, boundary conditions or parameter values are changed at each step. In *Transient* analysis, the simulation is performed by increasing time step and solving the device.

Once the results are obtained, they can be analyzed with **Sentaurus Visual (SVISUAL)** or **INSPECT**. Both tools are used for extracting data from the simulations and to create charts or contour maps of different variables (e.g. current, doping profile, charge generation). With all these tools, it is possible to perform a complete simulation, from process to electrical test, for a huge variety of devices and conditions.

3.1.1.1 Constitutive equations and physical models

As we mentioned earlier, Sentaurus calculates the physical quantities from a set of differential equations that govern the semiconductor physics. These equations are the Poisson equations and the continuity equation, that are:

$$\nabla \cdot (\varepsilon \nabla \phi + \vec{P}) = -q(p - n + N_D - N_A) - \rho_{trap} \qquad \text{Eq. 3.1}$$

And

$$\nabla \cdot \overrightarrow{J_n} = q\left(R_{net,n} - G_{net,n}\right) + q\frac{dn}{dt} \quad \text{Eq. 3.2}$$

$$-\nabla \cdot \overrightarrow{J_p} = q\left(R_{net,p} - G_{net,p}\right) + q\frac{dp}{dt} \quad \text{Eq. 3.3}$$

Where

- ε is the electrical permittivity
- Φ is the electrostatic potential
- $\vec{P}$ is the ferroelectric polarization
- q is the elementary charge
- n and p are the electron and hole densities
- ρ_{trap} is the charge contribution of fixed and traps charges
- R_{net} are the electron and hole recombination rate
- G_{net} are the electron and hole generation rate
- $\overrightarrow{J_n}$ and $\overrightarrow{J_p}$ are the electron and hole current densities
- N_D and N_A are the donor and acceptor concentrations

In the *Physics* section of the command file, different physical models regarding different aspects of semiconductor physics have to be selected. One of the main physical models to select is the carrier transport model. Three different models are available on Sentaurus, depending on the device that is investigated and on the level of accuracy required: the *drift-diffusion model*, the *thermodynamic* model and the *hydrodynamic model*. The transport models differ in the expressions used to compute $\overrightarrow{J_n}$ and $\overrightarrow{J_p}$. In the *drift-diffusion model* the current densities for electrons and holes are given by:

$$\overrightarrow{J_n} = \mu_n(n\nabla E_c - 1.5nkT\nabla lnm_n) + D_n(\nabla n - n\nabla ln\gamma_n) \quad \text{Eq. 3.4}$$

$$\overrightarrow{J_p} = \mu_p\left(p\nabla E_v - 1.5pkT\nabla lnm_p\right) + D_p(\nabla p - p\nabla ln\gamma_p) \quad \text{Eq. 3.5}$$

where E_V and E_C are the valence and conduction band energy, μ_p and μ_n are the hole and electron mobility, m_p and m_n is the hole and electron density-of-states mass, D_p and D_n the hole and electron diffusivity and γ_n and γ_p are the hole and electron degeneracy factor and T is the lattice temperature. The

first term represents the spatial variation of the electrostatic potential, the electron affinity, and the band gap, meanwhile the second term represents the contribution of the gradient of concentration. D and γ will depend on other models. The drift-diffusion models is used for isothermal simulation, and for low-power density devices with long active regions. Similar to the drift-diffusion model is the thermodynamic model, where the gradient of temperature is taken into account in the definition of the current densities.

$$\overrightarrow{J_n} = -nq\mu_n(\nabla\phi_n + P_n\nabla T) \quad \text{Eq. 3.6}$$

$$\overrightarrow{J_p} = -nq\mu_P(\nabla\phi_P + P_P\nabla T) \quad \text{Eq. 3.7}$$

On the other hand, the *hydrodynamic model* takes into account the energy transport of the carriers and it is applicable for small active regions. This makes this model applicable for deep-submicron devices and for simulations involving temperature. In the hydrodynamic model, the current densities are given by:

$$\overrightarrow{J_n} = \mu_n(n\nabla E_c + kT_n\nabla n - nkT_n\nabla ln\gamma_n + \lambda_n f_n^{td} kn\nabla T_n - 1.5nkT\nabla lnm_n) \quad \text{Eq. 3.8}$$

$$\overrightarrow{J_p} = \mu_p\big(p\nabla E_v + kT_p\nabla p - pkT_p\nabla ln\gamma_p + \lambda_p f_p^{td} kp\nabla T_p - 1.5pkT\nabla lnm_p\big) \quad \text{Eq. 3.9}$$

This equation takes into account the electrostatic potential variation, electron affinity and band gap (first part), then gradient of concentration, the carrier temperature gradients and the spatial variation of the effective masses. Thermal diffusions (f_n^{td} and f_p^{td}), D and γ, are defined by other models. Specifically, γ is defined by the Fermi statistics. The hydrodynamic model is preferred for sub-micron device simulations and thus it is the one we selected for this work.

The following aspect to consider is the modeling of the mobility. Sentaurus provides different mobility models, depending on the type of simulation to run. For undoped materials, the constant mobility model is

available, meanwhile for doped materials, there are several options for the user. These options cover a vast range of mobility models. For instance, the doping-dependent mobility model, that is used to take into account the carriers scatter with the impurities of the device. Moreover, there are models that describe the effect of carrier-carrier scattering and models that are useful to model the mobility degradation at interfaces. Eventually, the mobility degradation in high electric fields is taken into account by the High-Field saturation models. In Table 3.1, we report most of the models available on Sentaurus. Presenting the details of all these models would be outside the scope of this section. Instead, we will highlight some details of the one we have used in this work.

The model used in this work is the *Arora* model [71]. This model was chosen because it expresses the mobility as a function of the doping with concentration up to 10^{20} cm^{-3} and the temperature, in the range between 250 and 500 K. The mobility is defined by:

$$\mu_{dop} = \mu_{min} + \frac{\mu_d}{1 + ((N_{A,0} + N_{D,0})/N_0)^{A^*}} \qquad \text{Eq. 3.10}$$

Where:

$$\mu_{min} = A_{min} \cdot \left(\frac{T}{300K}\right)^{\alpha_n} \qquad \text{Eq. 3.11}$$

$$\mu_d = A_d \cdot \left(\frac{T}{300K}\right)^{\alpha_d} \qquad \text{Eq. 3.12}$$

$$N_0 = A_N \cdot \left(\frac{T}{300K}\right)^{\alpha_n} \qquad \text{Eq. 3.13}$$

$$A^* = A_a + \left(\frac{T}{300\ K}\right)^{\alpha_a} \qquad \text{Eq. 3.14}$$

The other coefficients (which are not defined here) are default values defined by Sentaurus, that can be found in the Sentaurus Device Manual [72].

Another key aspect in the physical models of TCAD tools is the recombination and generation mechanisms. These mechanisms are really

important especially in bipolar devices. For instance, recombination mechanisms are associated with the probability that a minority carrier will recombine. The higher the probability, then the lower the probability of a carrier to contribute to Single event Latchup. The first of this model is the *Shockley-Read-Hall (SRH) Generation-Recombination model*. It was first introduced in 1952 and it describes the generation and recombination of electron and hole pairs using the mechanism of trapping. That means that the transition through the conduction and valence band of an electron or an hole is assisted by the energy states create by the dopant or by a defect in the crystal lattice. This energy states are called traps. In Sentaurus, this model is implemented by:

$$R_{net}^{SRH} = \frac{np - n_{i,eff}^2}{\tau_p(n + n_1) + \tau_n(p + p_1)} \qquad \text{Eq. 3.15}$$

with:

$$n_1 = n_{i,eff}\exp\left(\frac{E_{trap}}{kT}\right) \qquad \text{Eq. 3.16}$$

$$p_1 = n_{i,eff}\exp\left(\frac{E_{trap}}{kT}\right) \qquad \text{Eq. 3.17}$$

Where E_{trap} is the difference between the defect level and the intrinsic level, which in silicon has a default value of 0, τ_p and τ_n are the lifetimes of the carriers and $n_{i,eff}$ is the effective intrinsic density.

When the doping concentration is high, the *Auger recombination model* is used. This is a non-radiative process which involves three particles. This happens when an electron and an hole recombine and either an electron is raised into the conduction band or an hole is pushed into the valence band. The model is expressed in Sentaurus by this formula:

$$R_{net}^{A} = (C_n n + C_p p)(np - n_{i,eff}^2) \qquad \text{Eq. 3.18}$$

Where C_n and C_p are temperature-dependent Auger coefficients [73]–[75]. The last model used is the Avalanche generation. This generation process is

important for Single Event Latchup because it can serve as a trigger condition. The generation rate is expressed as:

$$G_{ii} = \frac{1}{q}(\alpha_n|\overrightarrow{J_n}| + \alpha_p|\overrightarrow{J_p}|) \qquad \text{Eq. 3.19}$$

Where $\overrightarrow{J_n}$ and $\overrightarrow{J_p}$ are the electron and hole current density and α_n and α_p are called ionization coefficient.

Table 3.1 Mobility models available in Sentaurus.

Mobility due to phonon scattering	Constant model [65]
Doping dependent mobility	Masetti [66] Arora [67] University of Bologna [68], [69] Pmi_msc_mobility Pmi for bulk mobility Philips unified [70]
Carrier-Carrier scattering	Conwell-Weissokpf [71], [72] Brooks-Merring [73]
Mobility degradation at interfaces	Lombardi model [65] Inversion and accumulation layer model [74] University of Bologna [68], [69]
High Field saturation models	Canali model [75] Basic model Menerzhagen-Engl [76]

Obviously, the physical models present in Sentaurus are numerous and cover different aspects of the physical simulations. However, this would be out of the scope of this work. More information about the models can be found in the manual of Sentaurus [72].

3.1.1.2 Ion generation

Sentaurus allows to simulate different type of radiation, as gamma radiation, alpha particle and heavy ions. In this section we focus on heavy ions generation. The model used for the heavy ion collision is shown in Figure 3.5, meanwhile the generation rate is calculated by the formula:

$$G(l,w,t) = G_{LET}(l)R(w,l)T(t) \qquad \text{Eq. 3.20}$$

where G_{LET} is the linear energy transfer generation density and its unit is pairs/cm^3, $R(w,l)$ is a function describing the spatial variation of the generation rate and $T(t)$ is the temporal variation. $T(t)$ is defined as a Gaussian function:

$$T(t) = \frac{2 \cdot \exp\left(-\left(\frac{t-t_0}{\sqrt{2}-s_{hi}}\right)^2\right)}{\sqrt{2} \cdot s_{hi}\sqrt{\pi}\left(1 + erf\left(\frac{t_0}{\sqrt{2} \cdot s_{hi}}\right)\right)} \qquad \text{Eq. 3.21}$$

where t_0 is the timestep in which the ion penetrates the device and s_{hi} is the characteristics of the Gaussian function and it has a default value of 2 *ps*. On the other hand, $R(w,l)$ can be defined has an exponential function (Eq. *3.22*) or as a Gaussian function (Eq. *3.23*):

$$R(w,l) = exp\left(-\frac{w}{w_l(l)}\right) \qquad \text{Eq. 3.22}$$

$$R(w,l) = exp\left(-\left(-\frac{w}{w_l(l)}\right)^2\right) \qquad \text{Eq. 3.23}$$

where w is the radius of the track as defined in Figure 3.5 and $w_l(l)$ is a quantity defined by the user in the command file. The linear energy transfer generation density is defined as:

$$G_{LET}(l) = a_1 + a_2 l + a_3 e^{a_4 l} + k'[c_1(c_2 + c_3 l)^{c_4} + LET_f(l)] \quad \text{Eq. 3.24}$$

where $LET_f(l)$ is a function of the length, it is defined by the user and it can have units of $pairs/cm^3$ or $pC/\mu m$. Depending on the unit selection, k' can have different values to make the Eq. 3.24 dimensionally consistent. The other parameters are defined as following:

- $a_1 = 0$
- $a_2 = 0$
- $a_3 = 0$
- $a_4 = 0$
- $c_1 = 0$
- $c_2 = 1$
- $c_3 = 0$
- $c_4 = 1$

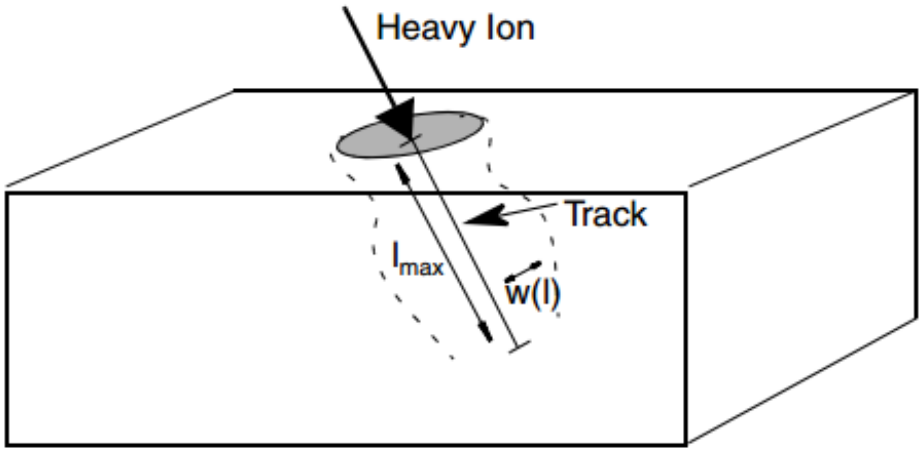

Figure 3.5 Ion strike definition in Sentaurus Synopsys [72].

3.1.2 ECORCE

Apart from the major software, there are available numerous TCAD tools, developed by companies, by universities, or in collaboration between companies and universities. One of these, it is a tool developed at the Université de Montpellier named ECORCE (Etude du COmportement sous

Radiation des Composants Electroniques) [76]. This software is based on a finite volume method and it can simulate 1D and 2D structures, as PN junctions, MOS transistors, bipolar transistors, IGBTs, and CMOS APS sensors. Here we will briefly highlight the key features of this software.

The software is based on the same governing equations, discussed in section 3.1.1.1. Then, Poisson's and continuity equation are solved, using the drift-diffusion model. Different recombination model can be used, as the SRH or the Auger model. Moreover, mobility as a function of doping concentration, electric field and carrier density can be selected. The geometry of the device is defined through a GUI, where all the geometrical characteristic of the device can be inserted. The doping profile can be fixed by the user, adding the donor and the acceptor concentration with a constant value or with a gaussian function. Meanwhile, the ion generation is defined by the formula:

$$G(x,y) = Density_{pairs}(x,y) \cdot W(t) \qquad \text{Eq. 3.25}$$

where the $Density_{pairs}(x,y)$ is the total density of pairs generated in a specific node by the ion and $W(t)$ is the time function of the ion generation defined as in Figure 3.6.

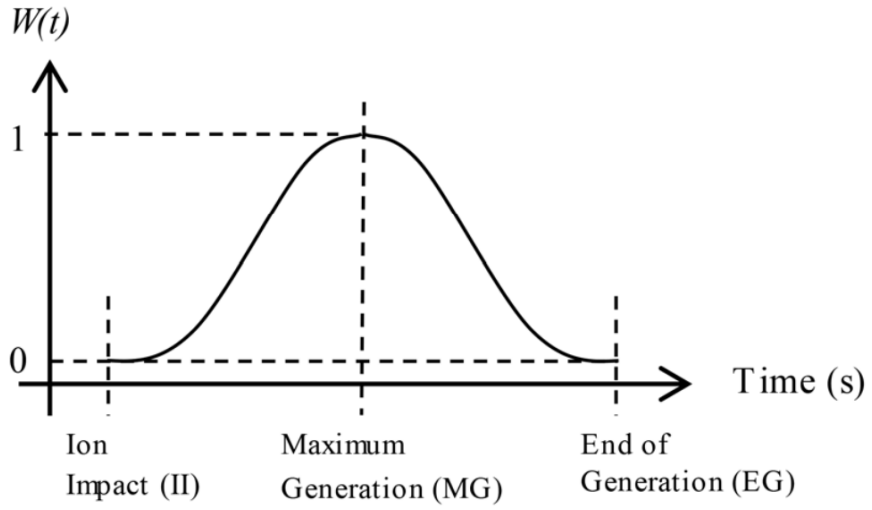

Figure 3.6 Temporal function for the ion generation in ECORCE [76].

The key difference of this TCAD tool compared to the other is that this software provides a dynamic mesh generator. This is truly important, because mesh is crucial for a correct simulation. Areas in which values can change by several order of magnitude requires a highly refined mesh, meanwhile areas with constant doping can be simulated with a coarse mesh. Usually, mesh is defined at the beginning of the simulation and cannot be change during it. Having a dynamic and automatic mesh generator allows to modify the mesh during the simulation, refining it where and when necessary. Avoiding refining the mesh when not necessary, it helps to save simulation time, because a more refined mesh requires more computational load.

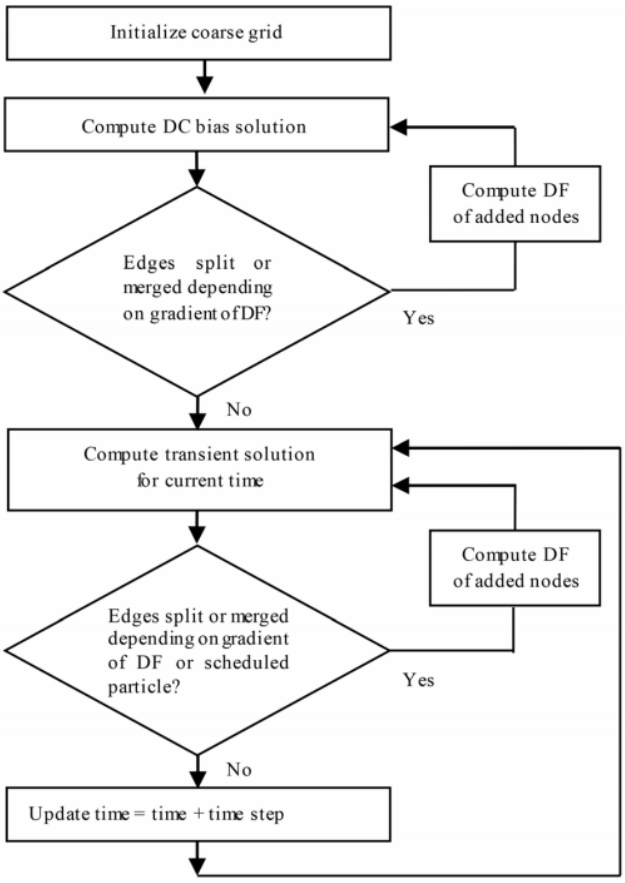

Figure 3.7 ECORCE's mesh design process [76] .

ECORCE locally refines and/or coarsens a single grid depending on the gradient of the Degrees of Freedom (DF, *i.e*. electron density) at each step

[76]. When the nodes are added, the value of the DF must be interpolated to obtain the value in the new node. However, errors may be introduces due to poor interpolation. To overcome this problem ECORCE solves the constitutive equations in the added nodes and then solves the equation in the new grid to improve precision of the solution, as explained in Figure 3.7.

3.2 SPICE

SPICE (Simulation Program with Integrated Circuit Emphasis) was developed in the 1970s at the Electronics Research Laboratory of the University of California, Berkeley. It was derived from another software called CANCER [77]. The first version, SPICE1, was presented in the 1973 [78]. However, the real popularity of SPICE started with SPICE2, which was released in 1975 [79]. SPICE2 is an improved version with more circuital elements than its predecessor. The last iteration is SPICE3 and it was developed by Thomas Quarles [80] in 1989, and it was the first version of SPICE developed in C, rather than in FORTRAN as the previous versions.

SPICE has become an essential tool for electrical engineers and has become important even for radiation effects studies. It is a software that simulates the electrical performance of electronic circuits. The simulations are performed by solving equations based on the Kirchhoff's current and voltage laws, using nodal point analysis. The vast database of the models for the common circuit components allows to perform simulations of most of electronic circuits.

The structure of a SPICE simulation consists of five major subprograms [81]: input, setup, analysis, output and utility. In the input step, the user has to define the circuit to be simulated. Each node of the circuit is defined by a unique integer numbers, except zero which is reserved for the ground. Then, at each element of the circuit is assign a unique name. The elements available in SPICE are shown in Table 3.2. Each element is identified with a letter. For example, a resistor will always be identified by an R.

Table 3.2 Circuit elements present in SPICE

Linear elements	Resistor (R)
	Capacitor (C)
	Inductor (L)
	Mutual Inductor (K)
	Independent Voltage Source (V)
	Independent Current Source (I)
	Linear Voltage-Controlled Current Source (G)
Non-linear elements	Non-linear Voltage-Controlled Current Source (N)
	Diode (D)
	Bipolar Junction Transistor (Q)
	Junction Field-Effect Transistor (J)
	Insulated-Gate Field-Effect Transistor (M)

The final result is what is called a SPICE input deck. We can see an example in Figure 3.8. The first line is what is called the title card and it is used as the heading for the various sections of the output. The following lines define the circuit we want to simulate. For instance, in the second line, VCC defines an independent voltage source, which has the positive node connected to the node 7, the negative is connected to the ground and the source value is 12 Volts.

The linear elements requires only that parameters to be completely specified, meanwhile the four semiconductor devices need more parameters. Thus, a separate line is used to specify the device model parameters. For instance, the BJTs in this example (Figure 3.8) are defined by the model MOD1, which is defined later in the input deck.

```
SIMPLE DIFFERENTIAL PAIR
VCC 7 0 12
VEE 8 0 -12
VIN 1 0 AC 1
RS1 1 2 1K
RS2 6 0 1K
Q1 3 2 4 MOD1
Q2 5 6 4 MOD1
RC1 7 3 10K
RC2 7 5 10K
RE 4 8 10K
 .MODEL MOD1 NPN BF=50 VAF=50 IS=1.E-12 RB=100 CJC=.5PF TF=.6NS
 .TF V(5) VIN
 .AC DEC 10 1 100MEG
 .PLOT AC VM(5) VP(5)
 .PRINT AC VM(5) VP(5)
 .END
```

Figure 3.8 Example of a SPICE input deck

Once the electrical circuit elements are defined, the user needs to define the type of analysis to be performed and the output to be generated. SPICE allows ten different analysis type, which are shown in Table 3.3. Then the input deck is terminated with the line .END.

Table 3.3 Type of analysis available in SPICE.

DC analysis	DC operating point
	Linearized device model parameterization
	Small-signal transfer function
	Small-signal sensitivities
	DC transfer curves
Transient analysis	Time-domain Response
	Fourier analysis
AC analysis	Small-signal Frequency-Domain Response
	Noise analysis
	Distortion analysis

After the input file is written, the input subprograms reads the input file and checks the circuit for possible errors. Then, the data subprogram constructs

additional data that are required by the following subprogram. The analysis subprogram performs the circuit analysis as it is specified in the input file and it generates the results that will be processed by the output subprogram.

3.3 Conclusion

In this chapter, we have presented the software that we have used in this work. Specifically, we have discussed the features of two TCAD tools, Sentaurus and ECORCE. We have focused our attention on the physical models used in Sentaurus, as it is the main tool used in this work. We have presented how it works, in order to give an indication for Single event Latchup simulations. Eventually, we have presented another tool used in this work, called SPICE.

In the next chapter, we will see how we used Sentaurus in this work. We will show our results on the effects of geometry and design parameters on the sensitivity of Single Event Latchup.

Chapter 4

Single Event Latchup cross section calculation from TCAD simulations

The topic of this work is the prediction of Single Event Latchup, considering the effect of design and temperature. As we mentioned before, SEL is a potential catastrophic condition that affects CMOS technology. It arises from parasitic bipolar transistors that are structurally intrinsic to this technology. If a radiation particle hits the component, electron-hole pairs are generated in the structure and thus they can lead to the activation of the parasitic thyristors if the deposited energy is large enough. However, the deposited energy by the radiation particle is not the only parameter to consider as far as SEL sensitivity is concerned.

Then, as a first step, we have analysed the effect of few of these parameters. We have investigated the effect of the modification of the doping profile, the anode to cathode spacing (A-C spacing) and the well and substrate distance (W-S distance). In the literature, different works have investigated the effect of the doping profile, the anode to cathode spacing and the well and substrate distance. For instance, doping profile variation has been analyzed in the work of Rezzak *et al.* [64]. In this study, 3D simulations are used to investigate and harden Single-Event Latchup occurring in embedded SRAMs. P-well doping and the N-well doping variation has been investigated. The results showed how the increased in the doping hardens the components. Furthermore, anode to cathode spacing has been investigated in [64] and in Youssef *et al.* [82]. In both works, increasing the spacing leads to a lower SEL sensitivity.

Nonetheless, temperature has an important role in SEL sensitivity and so it is also interesting to analyze the behaviour of cross section when design parameters variation and temperature variation are combined. So, firstly we

have analyzed the effect of the variation of the design parameters (doping profile, substrate and well taps placement and anode to cathode spacing) on SEL sensitivity. Then, we have investigated, considering a specific range of temperatures, what is the role of temperature on SEL sensitivity when other parameters are modified.

In order to achieve our goal, we have extended the investigation to SEL cross section and not only to threshold LET. The investigation has been performed by TCAD tools, with 2D simulations. With that, SEL cross section has been calculated and the effect of these parameters on SEL sensitivity has been studied. From these curves, we have estimated the in-orbit SEL rate for Geostationary Earth Orbit (GEO). In this way, we have used the SEL rate to study the effects of the parameters for the whole LET range and not only in term of threshold LET. Hence, when specific parameters are selected for a design, these results can indicate if temperature variation will strongly modify the behaviour of SEL sensitivity.

The structure of this chapter is the following. First, we will describe the methodology used in this work. We will discuss about the simulated structure and how we have calculated the cross section and the SEL rate. Then, we will focus on two aspects: on one side, we will analyze the effect of the layout modification on SEL sensitivity and on the other side, the effect of the temperature on the layout modification will be investigated. Then, both effects will be discussed.

4.1 Methodology

As mentioned earlier, we thus used TCAD simulations. They have been widely used in the literature [83], [84] and provide an insight view of the mechanism of Single Event Latchup. In our work, we have performed 2D simulation, using Sentaurus Synopsys tools. Even though SEL is a 3D effect, in order to save calculation time, it is possible to perform 2D simulations. As a matter of fact, it has been shown that SEL sensitivity in 3D simulations follows the same trend as in 2D simulation [83], [85]. Furthermore, with

TCAD simulations it is possible to evaluate the importance of the parameters that influence SEL sensitivity. It is important to understand the relevance of each of these parameters, because knowing how much they influence SEL sensitivity, could be helpful during the design of the components but also for the development of a predictive tool. Nonetheless, TCAD simulations provide information only about electrical characteristic like current or voltage, or about doping profiles and carrier characteristics. Hence, parameters that are strictly related to radiation sensitivity, like cross section, must be retrieved by these data, as we have performed in our work.

Here, we focused our analysis on the effects of temperature, A-C spacing, doping profiles variation and well and substrate distance. The aim is to quantify the influence of these parameters on SEL sensitivity, not only in term of threshold LET In fact, threshold LET would give information only about the LET needed to trigger SEL in the most sensitive position of the device Meanwhile, we wanted to consider all device and what value of LET is needed to trigger SEL in other positions. To achieve this goal, the cross sections obtained through 2D simulations have been used. This method combines the opportunity to run fast 2D simulations while obtaining a key parameter to measure SEL sensitivity. The results can be helpful to understand which parameter must be carefully chosen for the design of a CMOS component or for the creation of an SEL predictive tool.

4.1.1 Simulated structure

As aforementioned, Single-Event Latchup affects CMOS devices. However, the simulation of the full CMOS component is not necessary. Single-Event Latchup can be studied by using only two of the parasitic transistors, that are present in the CMOS [42]. Then, for this work, an PNPN structure formed by a PMOS source and an NMOS source is used (Figure 4.1).

The structure is based on a 65 nm CMOS inverter. The inverter is created in Cadence Virtuoso, following the 65nm design rules. Therefore, the 2D NPNP is retrieved by cutting the CMOS inverter as shown in Figure 4.2. The component has a width of 3 μm and a depth of 0.88 μm. The distance

between the anode and the cathode spacing is set at 0.32 µm, the doping profiles is based on a commercial bulk 65nm process and the well and substrate taps placement, indicated by their distance, is set to 1.25 µm. A V_{DD} of 2 V is applied to the N-well and to P-source, meanwhile the other terminals are grounded. Eventually, all these data are used in Sentaurus Structure Editor to create the structure shown in Figure 4.1.

After creating the structure, it is necessary to generate a mesh. As mentioned in section 3.1, we need a finer mesh close to the junctions and broader mesh where it is not important to have an accurate calculation.. In our case, a broad mesh is applied to the substrate, because the doping profile variation is modest, and it is not relevant for the SEL. A coarser mesh is applied to the N-well and the diffusions, where most of the charge transport is happening. Eventually, a more refined mesh is applied in the ion track because it is the area in which the charge generation is happening. In Figure 4.3, it is shown the mesh used in this work.

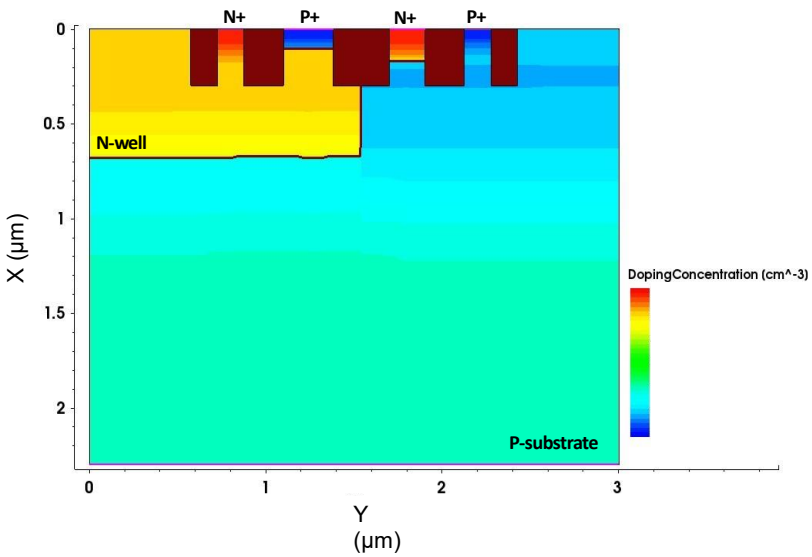

Figure 4.1 2D structure of the PNPN built with Sentaurus Structure editor

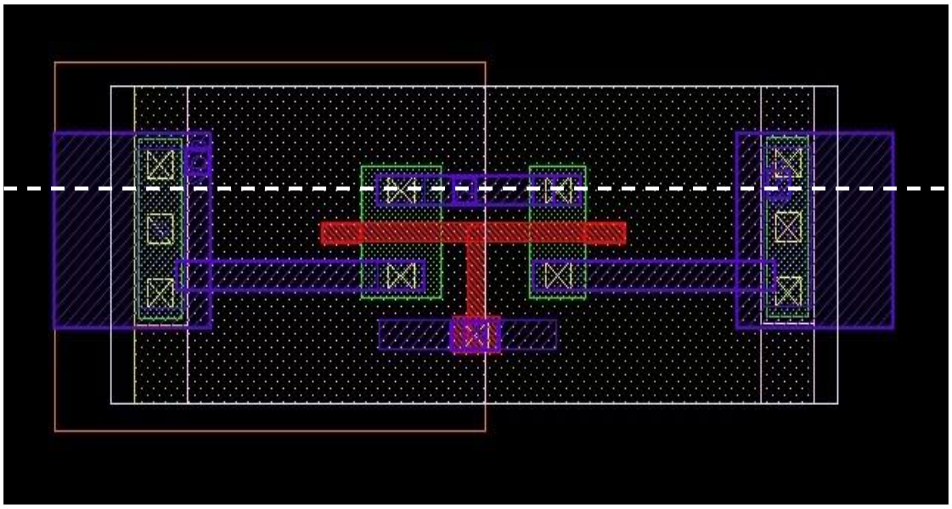

Figure 4.2 Top view of a 65nm based CMOS inverter developed in Cadence Virtuoso

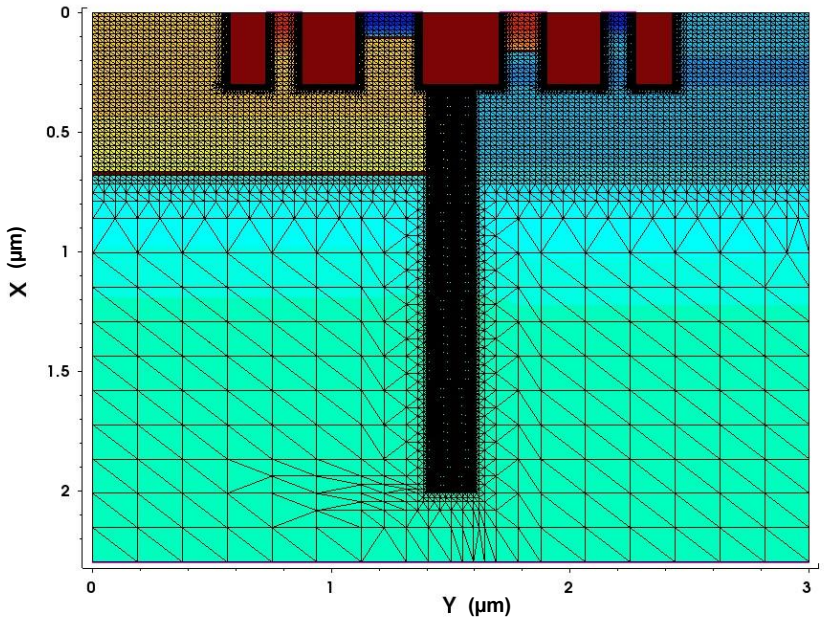

Figure 4.3 2D structure of the NPNP with the different mesh used.

4.1.2 Parameter variation

The reference value for each parameter are varied, to evaluate the effects of the variation of each single parameter. The A-C spacing is varied and the following values have been chosen: 0.25, 0.27, 0.37 and 0.40 µm. The

reference doping profile is varied by multiplying the reference profile respectively times 0.75, 0.85, 1.15 and 1.25. Well to substrate distance is modified using these parameters: 1.05, 1.55, 1.85 and 2.15 μm. In this way, we move taps symmetrically further from the center of the component as we increase their distance. Eventually, we have chosen four values of temperature, 350 K, 375 K, 400 K and 425 K. This range was chosen because it allows to obtain a Single event Latchup in most of the simulations. A summary of the parameters used is reported in Table 4.1. Also, in Figure 4.4 we depict the parameters we have considered in the PNPN structure.

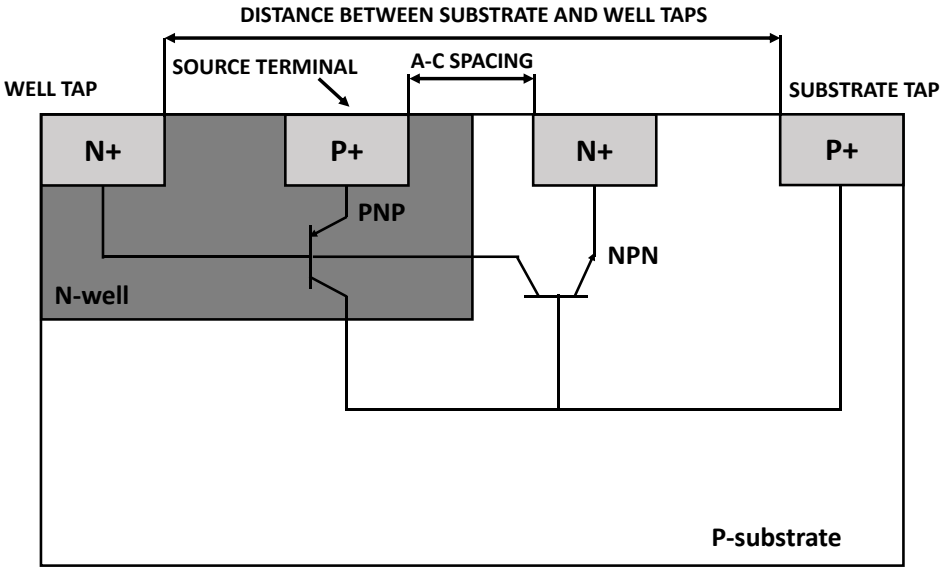

Figure 4.4 PNPN structure with the parameters considered in our simulations and representing the parasitic transistors.

Table 4.1 Summary of the parameters used in the simulations

Doping profile factor	A-C Spacing (μm)	W-S Distance (μm)
x0.75	0.25	1.05
x0.85	0.27	**1.25 (Reference)**
Reference	**0.32 (Reference)**	1.55
x1.15	0.37	1.85
x1.25	0.40	2.15

4.1.3 Cross section calculation

From the ion simulations, SEL cross section has been calculated. To estimate the cross section, the method as reported in [86] has been used. The strike position of the ions was simulated in different parts of the structure along its width. The aim was to obtain the minimum LET value necessary in order to trigger SEL in each simulated location. To obtain this value, we have performed simulation by increasing the LET with 1 *MeV.cm²/mg* step (Figure 4.5). To analyze if the SEL occurred or not, we have measured the current at the source terminal. When the LET is sufficient to trigger SEL, the measured current will increase exponentially and then it will reach a plateau. This means that the SEL is triggered. This value is then stored and after that, a chart with minimum LET versus position of the strike has been created as in Figure 4.6. From this chart, by using a LET_x value that range from 2 to 250 *MeV.cm²/mg*, we calculated two values, X_1 and X_2. Considering that we used a finite number of strike positions, if a specific LET_x value did not correspond to the LET value of a simulated strike position, X_1 and X_2 are calculated by interpolation of the available data. So, the value X_2- X_1 represents the width of the sensitive zone for each value of

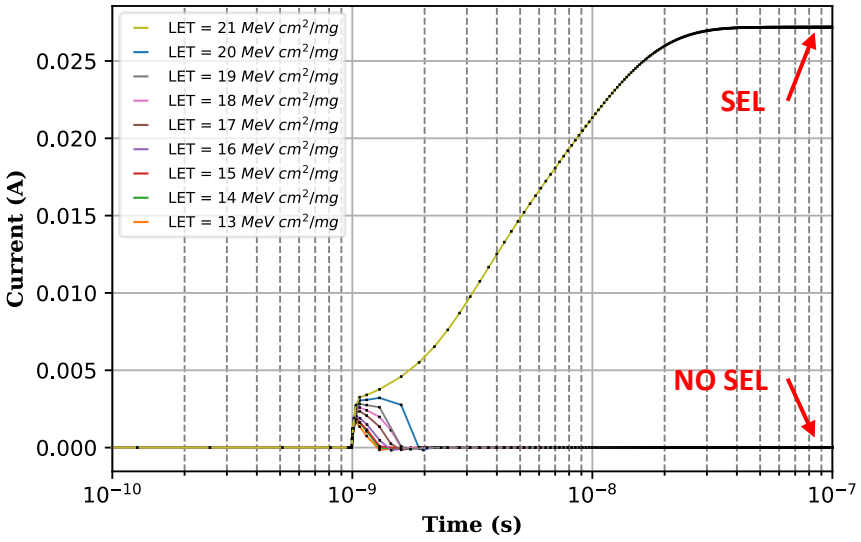

Figure 4.5 Source current versus time for different LET values.

LET_x. It means, that for any strike in the sensitive zone with an LET value equal to LET_x, SEL will be induced. Eventually, cross section is calculated by multiplying the sensitive zone by the width of the component, obtaining a curve as in Figure 4.7.

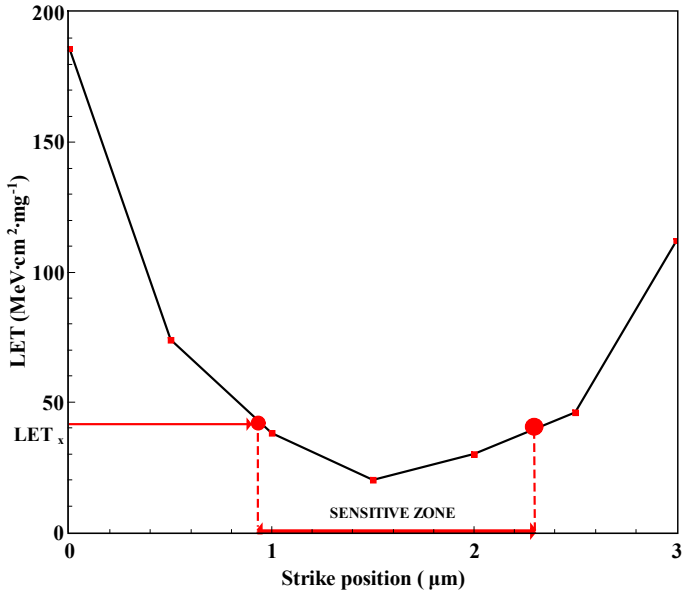

Figure 4.6 Minimum LET value versus position.

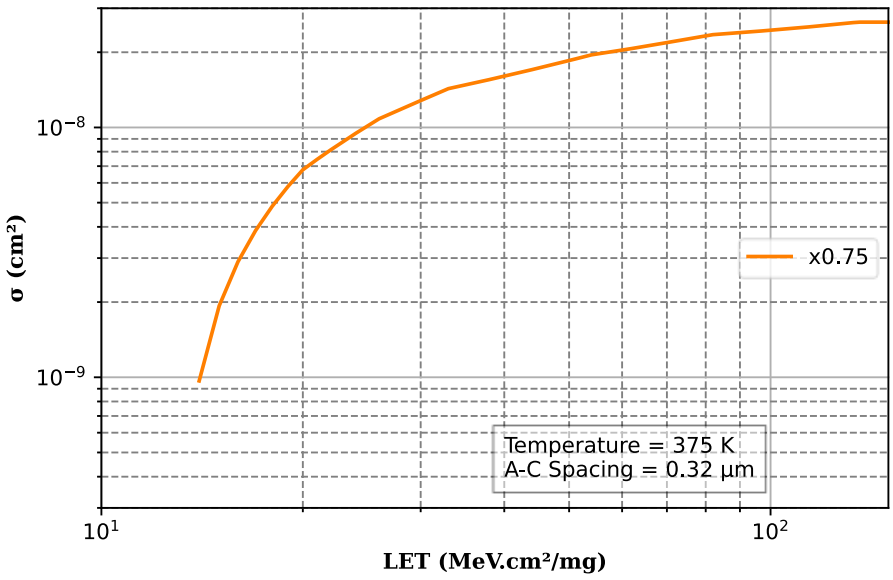

Figure 4.7 Example of SEL cross section calculated with our methodology.

4.1.4 SEL Rate

Once the SEL cross section is calculated, we have been able to use it to calculate the SEL Rate. This rate estimates the probability of a SEL in a given space environment. In this work, we have estimated the in-orbit SEL rate for the Low Earth Orbit (LEO) and for the Geostationary Orbit (GEO). To do so, we have used the software OMERE [87]. This software is a tool dedicated to the analysis of the space environment and radiation effects on electronics developed by TRAD and CNES. The OMERE software uses the Integral Rectangular Parallelepiped (IRPP) approach to predict SEL rate, and it is calculated by using heavy ion cross section data, given by the user, in combination with the flux in a specific space environment, given by the software. This approach is suggested by the handbook issued by the European Cooperation for Space Standardization (ECSS) [41].

In more detail, the chosen orbits were the standard orbits that the software provides. The GEO orbit is considered at an altitude of 35784 km, meanwhile the LEO orbit is the standard orbit for the International Space Station, with an apogee and perigee of 400 km and an inclination of 51.6°. The space environment was modelled by the international standard ISO 15390 model, which is used for Galactic Cosmic Rays fluxes.

4.1.5 Simulation physics and ion track

In section 3.1.1.1, we have discussed the physics behind the Sentaurus Synopsys simulator. Here, we recap the models we have chosen for our work:

- 2D NPNP structure based on a 65nm CMOS inverter
- Sentaurus Physics:
    - Hydrodynamic model
    - Fermi statistics
    - Mobility model: Arora
    - Recombination: doping dependent Shockley-Read-Hall, Auger recombination and avalanche generation

- Bandgap narrowing

As far as the ion track is concerned, we have run simulations with SRIM [33]. Using as a reference the ions cocktail available in a typical heavy ion facility, we found that the LET was constant along the component. So, linear energy transfer has been chosen constant and the range is 2.3 µm to cover the entire structure. The radial distribution has been set with a Gaussian profile with a 50 nm radius, according to previous works [72],[73].

4.2 Effects of layout modification

The first aspect we have analyzed is the impact of layout modification on SEL sensitivity (Table 4.1). The Figure 4.8 shows a recap of the procedure we have used.

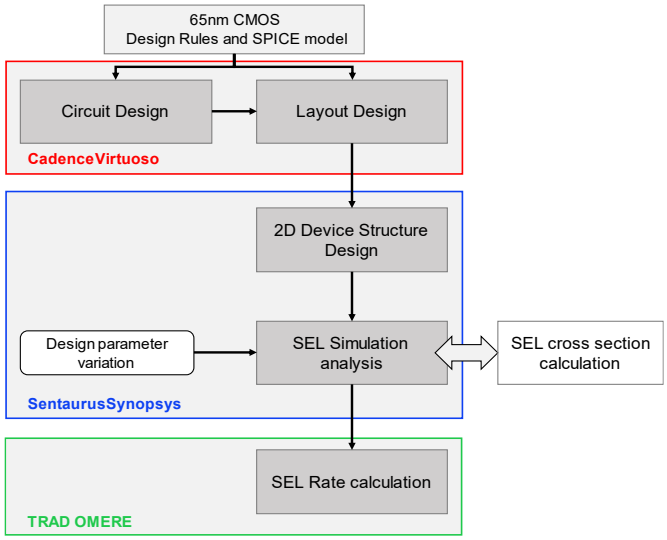

Figure 4.8 The methodology used to calculate the effect of the design parameter variation.

But, to start with, we have investigated the effect of temperature on the SEL cross section (Figure 4.9) It is widely known that temperature is a key parameter for Single Event Latchup [51], [55]. From the simulations we obtained results that agree with the literature that is to say that CMOS components become more sensitive to SEL when the temperature increases. So, for the same value of LET, cross section increases for higher

temperatures. Then, we moved our attention to the three parameters we decided to investigate.

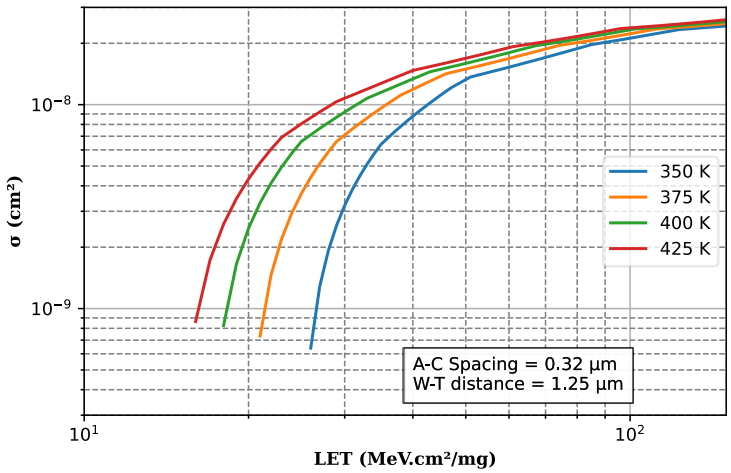

Figure 4.9 SEL cross section for temperature

First in Figure 4.10 - (*top*), the threshold LET trend for different A-C spacing is shown. It ranges from a value of 16 MeV.cm^2/mg for the smallest value of A-C spacing to 26 MeV.cm^2/mg for the higher value. Increasing the A-C spacing by 25% leads to a threshold LET increase of 30%. Conversely, decreasing A-C by around 20%, the threshold LET is also decreased by 20%. Thus, an increment of A-C spacing leads to a decrease of SEL sensitivity. This trend is confirmed by the literature [56]. Moreover, the same trend is obtained for the saturation LET (which we consider as the LET value at which saturation cross section is reached) is achieved. Indeed, as for the minimum LET, the lowest value is 174 MeV.cm^2/mg and it is obtained for the smallest A-C spacing, whereas a value of 198 MeV.cm^2/mg is reached for the highest value of A-C spacing (0.40 µm). Then, we show the trend of cross section in Figure 4.10 - (*bottom*). It is important to remark that these curves follow the same trend as the threshold LET. So, in this case, even for higher LET, increasing A-C spacing leads to a lower sensitivity and so a lower cross section.

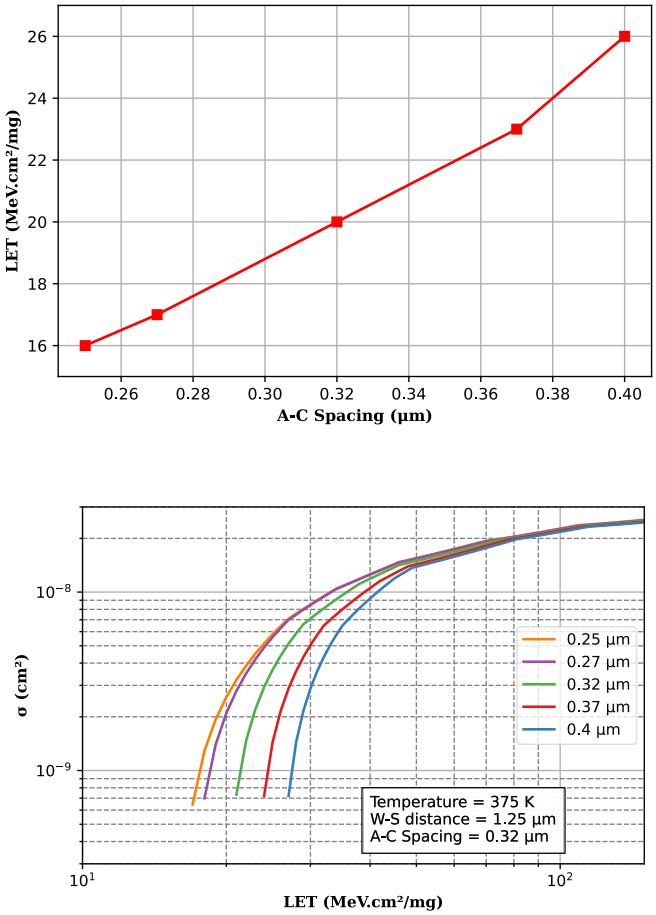

Figure 4.10 SEL threshold LET (top) and cross section for Anode to cathode spacing (bottom)

Secondly, the doping profile variations effects are investigated. As in the previous case, the threshold LET is shown in Figure 4.11 - (*top*). In this case, the LET threshold goes from 14 MeV.cm²/mg to 32 MeV.cm²/mg. An increment of 25% leads to a LET threshold increment of 60%, meanwhile a 25% decrease leads to a 40% reduction of threshold LET. Thus, in this case, the component with a higher doping profile results in a more hardened one. Even in this case, results agree with literature [89]. As for the A-C spacing, the saturation LET follows the same trend of the LET threshold. It ranges from a value of 136 MeV.cm²/mg when the doping profile is 75% of the reference and increases to a value of 246 MeV.cm²/mg when the doping profile is 125% of the reference. Even in this case, the cross section is calculated (Figure 4.11 - *bottom*). What has been seen for A-C spacing is

confirmed for the doping profile. In fact, the trend of the cross section follows the trend of the threshold LET.

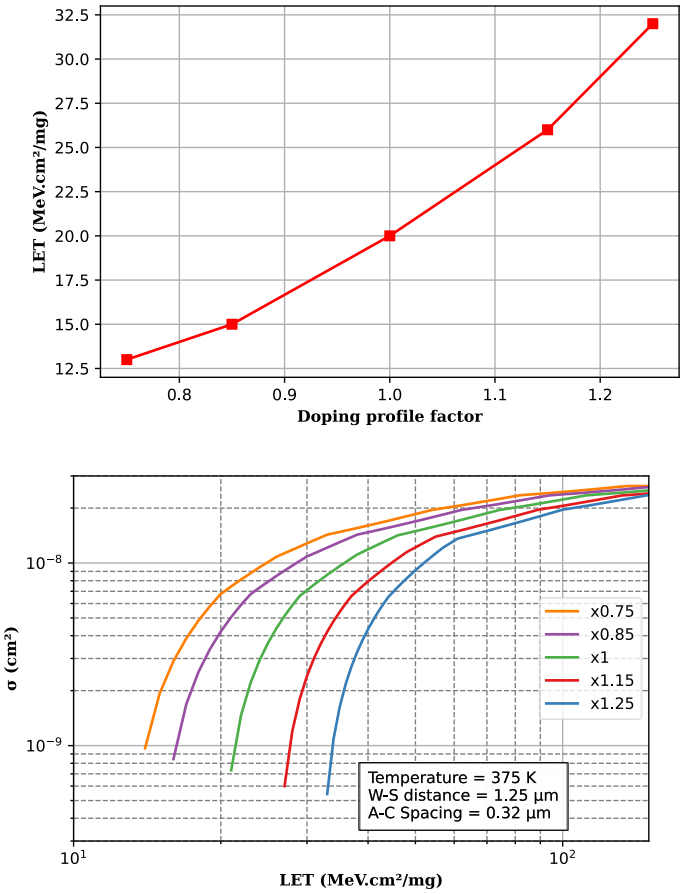

Figure 4.11 SEL threshold LET (top) and cross section for doping profile factor (bottom).

Finally, the influence of the placement of the substrate and well taps is investigated (Figure 4.12 - *top*). The LET threshold ranges from 10 *MeV.cm²/mg* to 28 *MeV.cm²/mg*. Increasing the distance by 50% reduces the threshold LET by 40% and decreasing it by 15% increases the LET threshold by 40%. As expected from the literature [43], [57] placing substrate and well taps further from the center of the component will result in a lower value of LET threshold. Equally, saturation ranges from 154 *MeV.cm²/mg* to 220 *MeV.cm²/mg*. Lastly, we present a cross section chart regarding substrate and well taps placement (Figure 4.12- *bottom*). Again, calculating the cross

section allows us to know that the trend for higher LET does not change and follows the threshold LET behavior.

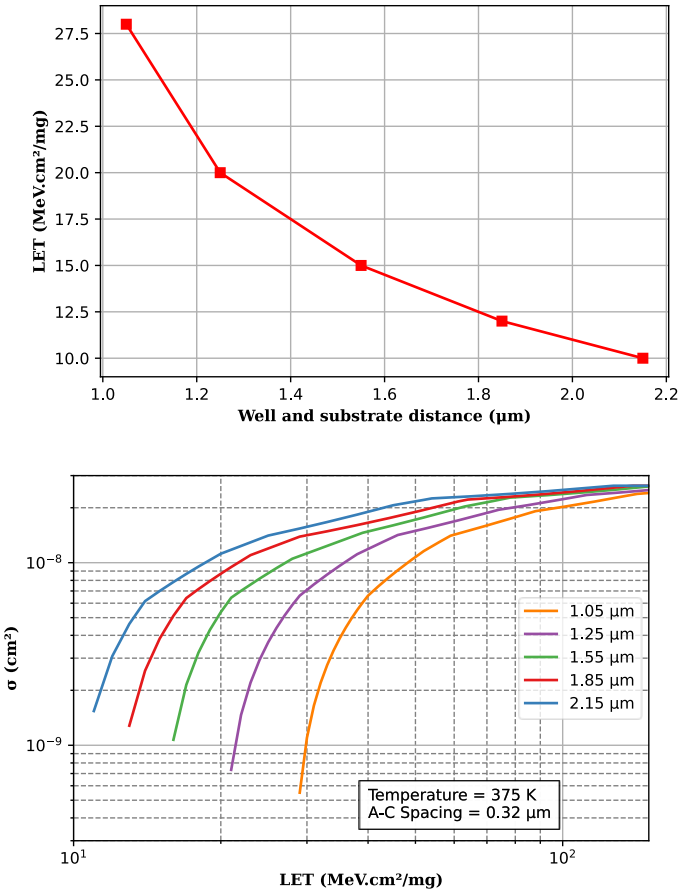

Figure 4.12 SEL threshold LET (top) and cross section for substrate and well taps placement (bottom).

Furthermore, we have used the cross section to calculate the SEL rate. That allows us to investigate the SEL immunity more deeply. In this case, it has been calculated using software OMERE, a free software dedicated to space environments [87], considering International Space Station orbit. In Table 4.2, we present the SEL rate for the previous parameters, that follows the same trend of the cross section. The units are in *SEL/device/day* because for sake of simplicity we have chosen to use only in our simulations. It is necessary to multiply by the number of devices to obtain *SEL/day.*

Table 4.2 SEL Rate calculated for different parameters.

Doping profile	SEL/device/day	A-C spacing (µm)	SEL/device/day
x0.75	$8.10 \cdot 10^{-10}$	**0.25**	$3.97 \cdot 10^{-10}$
x0.85	$5.07 \cdot 10^{-10}$	**0.27**	$3.28 \cdot 10^{-10}$
x1	$2.54 \cdot 10^{-10}$	**0.32**	$2.54 \cdot 10^{-10}$
x1.15	$1.01 \cdot 10^{-10}$	**0.37**	$1.60 \cdot 10^{-10}$
x1.25	$4.44 \cdot 10^{-11}$	**0.40**	$1.14 \cdot 10^{-10}$
Taps distance (µm)	**SEL/device/day**	**Temperature (K)**	**SEL/device/day**
1.05	$7.46 \cdot 10^{-11}$	**350**	$1.09 \cdot 10^{-10}$
1.25	$2.54 \cdot 10^{-10}$	**375**	$2.54 \cdot 10^{-10}$
1.55	$5.80 \cdot 10^{-10}$	**400**	$3.55 \cdot 10^{-10}$
1.85	$1.03 \cdot 10^{-09}$	**425**	$5.02 \cdot 10^{-10}$
2.15	$1.69 \cdot 10^{-09}$		

4.3 Temperature effects

The second aspect we have investigated is the impact of temperature on the layout modification. In Figure 4.13 we recap the methodology we have used. We have used the same design parameter variation as in section 4.2 and we added the temperature variation.

Table 4.3 Summary of the parameters used in the simulations

Temperature (K)	350	375	400	425
DP Factor	x0.75 – x0.85 – x1 – x1.15 – x1.25			
A-C Spacing (µm)	0.25 – 0.27 – 0.32 – 0.37 – 0.40			
W-S distance (µm)	1.05 – 1.25 – 1.55 – 1.85 - 2.05			

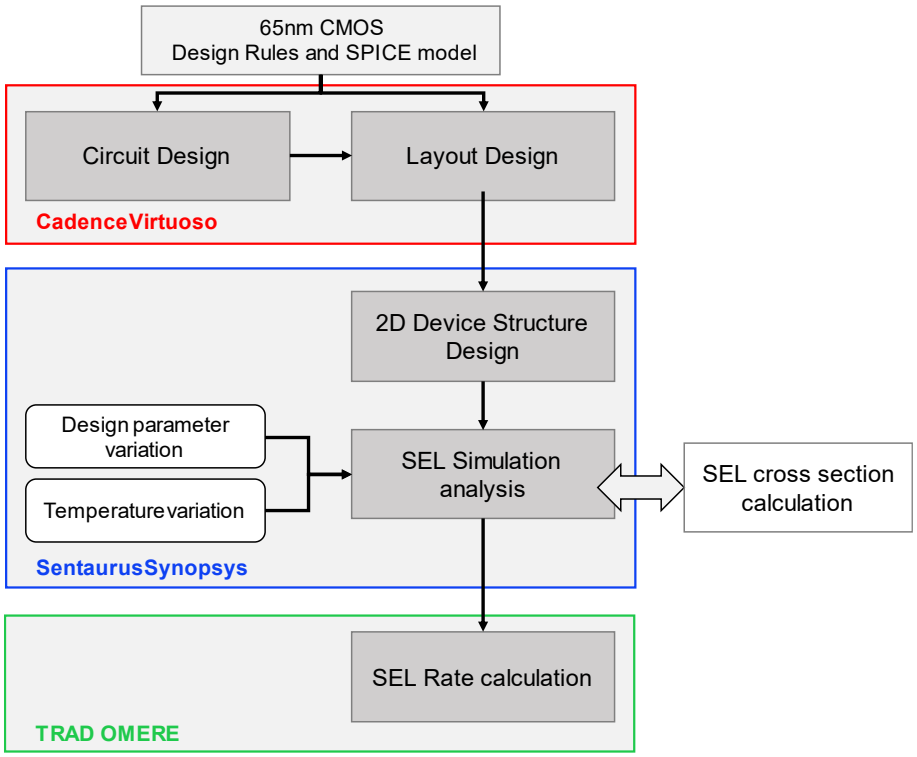

Figure 4.13 The methodology used to calculate the effect of the temperature variation.

In the next sections, we are going to analyze the results obtained by our simulations. Results are shown by using a chart and a table. The first one represent the threshold LET or the SEL rate versus the parameter considered (*i.e.* well to substrate distance). Following the chart, we use a table to show how the threshold LET or the SEL rate vary as the temperature increases for the same parameter value. To explain this, we show an example taken from Figure 4.14 and Table 4.4. In Figure 4.14, we see that there is a 22% relative difference between the threshold LET at 425 K and at 400 K. Meanwhile, between 375 K and 400 K, there is a 27% relative difference, reported in the table. Then, if no SEL occurs at a certain temperature, the value is indicated by a NO SEL text, because it is not possible to calculate a difference. The colors are used to give a quick insight on the variation of the threshold LET or SEL rate according to the temperature and the parameter variation, meanwhile are used to quantify the relative difference between each items.

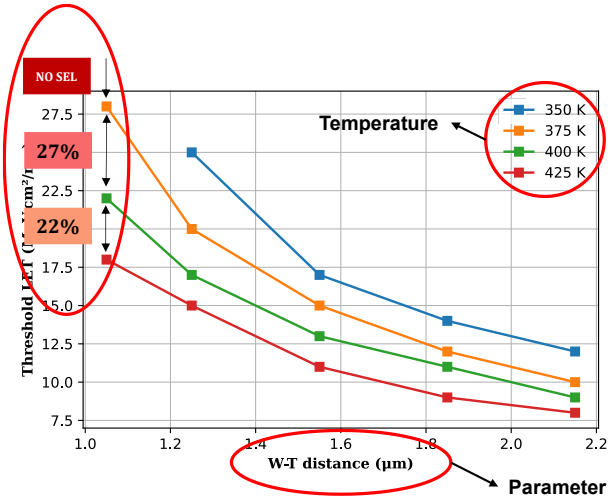

Figure 4.14 Example of the charts used in this chapter.

Table 4.4 Example of the tables used in this chapter.

	1.05 µm	1.25 µm	1.55 µm	1.85 µm	2.05 µm
350 K	NO SEL	25%	13%	17%	20%
375 K	27%	18%	15%	9%	11%
400 K	22%	13%	18%	22%	13%
425 K	0%	0%	0%	0%	0%

4.3.1 Threshold LET analysis

First, in Figure 4.15, the threshold LET trend for doping profiles is shown. Specifically, it is shown the trend for the range of temperature considered. As expected, threshold LET decreases as the temperature increases and increases with the doping profile [64]. Moreover, it is interesting to focus on the trend. If we consider the condition in which the device design is more favorable to induce Single-Event Latchup, as the worst-case scenario (lowest threshold LET, i.e. lower doping level) and the best-case scenario as the opposite, we can observe that the threshold LET increases more for lower temperatures. Eventually, at 350 K, no SEL is

achieved for x1.15 and x1.25, which are conditions less favorable to SEL. In Table 4.5, we show this trend, considering the actual values. In this table, it is shown the relative difference of the threshold LET, with respect to the previous case (and then for the same temperature), starting from 425 K, which is the temperature condition more favorable to Single-Event Latchup. Here, we can see clearly, that the more we approach the worst condition (i.e. lower temperature and higher doping profile), the more the threshold LET difference is higher. For instance, for the x0.75 case, the maximum difference obtained is the 18%, and it increases as we increase the doping profile, reaching for the x1.25 case a 33% difference, plus no SEL at 350 K.

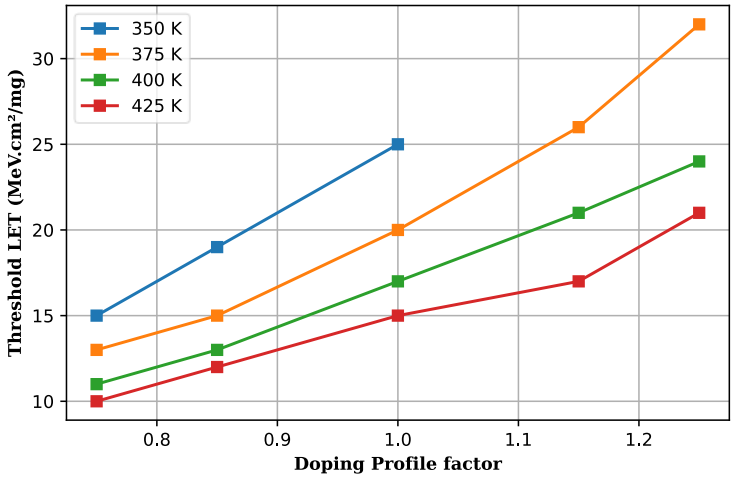

Figure 4.15 Threshold LET versus the doping profile factor for four different temperatures (350 K, 375 K, 400 K, 425 K).

Table 4.5 Summary results for threshold LET relative difference for the doping profile factors.

	x0.75	x0.85	x1	x1.15	x1.25
350 K	15%	27%	25%	NO SEL	NO SEL
375 K	18%	15%	18%	24%	33%
400 K	10%	8%	13%	17%	20%
425 K	0%	0%	0%	0%	0%

In Figure 4.16, threshold LET curves for substrate and well taps placement are shown. Thresholds decrease as the temperature increases and it is higher as taps are placed closer to the center of the device, which is confirmed by literature [64]. Furthermore, we can analyze the influence of temperature by looking at Table 4.6. In this case, the effect of the temperature is less important for 1.55 µm, 1.85 µm and 2.05 µm. The difference does not always increase as the temperature decreases. Nonetheless, the effect of temperature is more relevant for the worst-case scenario, where a 27% difference is achieved, and at the same time, no SEL is obtained at 350 K for this case.

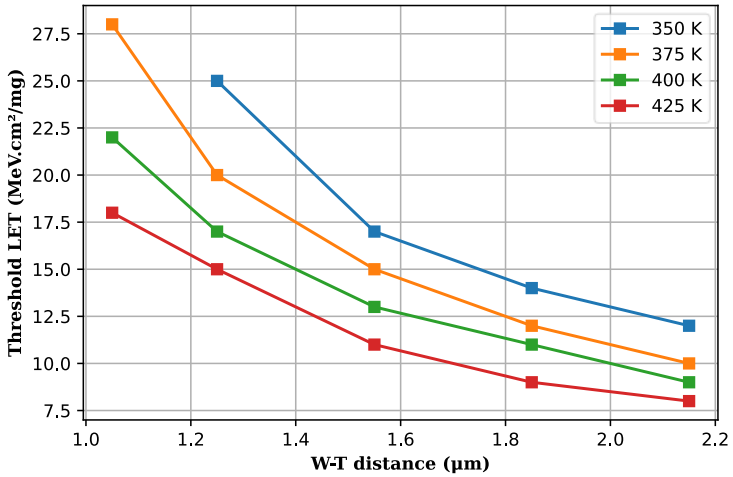

Figure 4.16 Threshold LET versus the anode to cathode spacing for four different temperatures (350 K, 375 K, 400 K, 425 K).

Table 4.6 Summary results for threshold LET relative difference for the well and substrate taps placement.

	1.05 µm	1.25 µm	1.55 µm	1.85 µm	2.05 µm
350 K	NO SEL	25%	13%	17%	20%
375 K	27%	18%	15%	9%	11%
400 K	22%	13%	18%	22%	13%
425 K	0%	0%	0%	0%	0%

Eventually, in Figure 4.17 threshold LET curves for anode to cathode spacing are shown. The trend that has been observed for the previous parameters is also confirmed for the A-C spacing. Regarding this condition, in the worst case, the relative threshold LET difference is 19%, meanwhile, as expected, a higher value is reach at the best-case scenario (30%) and SEL is not reached for 350 K. In this case, the difference is smaller with respect to previous examples. The reason may be that the effects of anode to cathode spacing variation is lower with respect to the other parameters. In conclusion, for all the conditions investigated parameters. In conclusion, for all the conditions investigated, temperature influence on SEL sensitivity is lower when conditions are more favorable to SEL and increases as parameters are modified to make the component less sensitive.

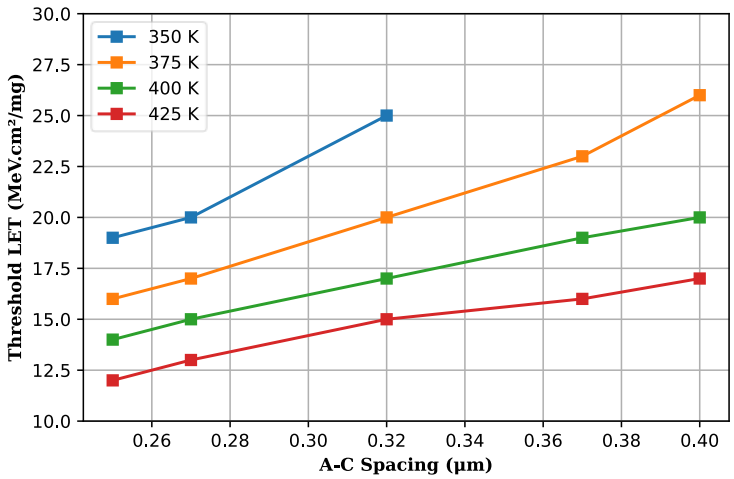

Figure 4.17 Threshold LET versus the well and substrate taps distance for four different temperatures (350 K, 375 K, 400 K, 425 K).

Table 4.7 Summary results for threshold LET relative difference for the anode to cathode spacing.

	0.25 µm	0.27 µm	0.32 µm	0.37 µm	0.40 µm
350 K	19%	18%	25%	NO SEL	NO SEL
375 K	14%	13%	18%	21%	30%
400 K	17%	15%	13%	19%	18%
425 K	0%	0%	0%	0%	0%

4.3.2 SEL rate analysis

To further investigate this trend, we have calculated the SEL rate for two orbits, using OMERE, a free software dedicated to space environments. We have considered GEO orbit and LEO orbit. First, we consider the GEO orbit. Cross sections calculated with the 2D approach have been used to calculate the SEL rate. Regarding the doping profile, in Figure 4.18, it can be seen that SEL rate follow the same trend observed for threshold LET. Considering that SEL rate takes into consideration the whole cross section, it means that the trend that has been seen for the threshold LET is present even for higher LET. In Table 4.8, we show the SEL rate relative difference for increasing temperature, for the same case, starting at 425 K. At the lowest temperature (*i.e.* best-case scenario), the relative difference increases from 39%, for the lowest doping profile, to 80% for the reference doping profile. Meanwhile, for the higher doping profiles, no SEL is achieved, but at 375 K, the relative difference is 73% and 97% for the x1.15 and x1.25 respectively.

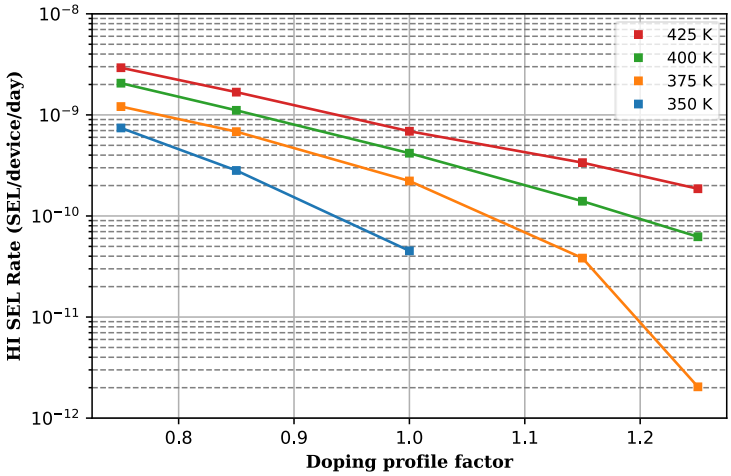

Figure 4.18 Heavy Ion SEL rate at GEO orbit versus the doping profile factor for four different temperatures (350 K, 375 K, 400 K, 425 K).

Table 4.8 SEL rate difference at GEO orbit for the doping profile variation, starting from 425 K.

	x0.75	x0.85	x1	x1.15	x1.25
425 K	0%	0%	0%	0%	0%
400 K	-30%	-34%	-39%	-58%	-67%
375 K	-41%	-38%	-47%	-73%	-97%
350 K	-39%	-59%	-80%	NO SEL	NO SEL

In Figure 4.19, it is shown the SEL rate for substrate and well taps placement. Even in this case, the trend is confirmed. The relative difference SEL rate increases from 39% for the best-case scenario at 350 K to 81% at the reference value for the same temperature, plus no SEL in the worst-case scenario for 350 K (Table 4.9). Eventually, SEL rate for A-C spacing is presented (Figure 4.20). SEL rate relative difference varies from 67% to 97% for the best case and from 30% to 39% in the worst case. The trend of the cross section follows the trend of the threshold LET.

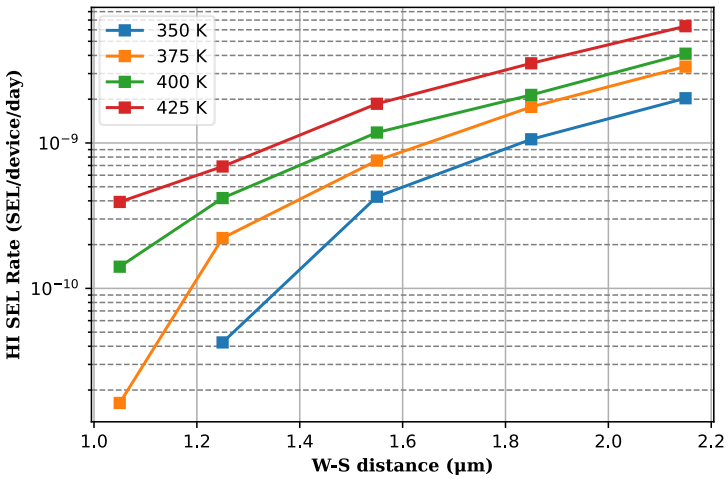

Figure 4.19 Heavy Ion SEL rate at GEO orbit versus the well and substrate taps distance for four different temperatures (350 K, 375 K, 400 K, 425 K).

Table 4.9 SEL rate difference at GEO orbit for the well and substrate taps distance, starting from 425 K.

	1.05 µm	1.25 µm	1.55 µm	1.85 µm	2.05 µm
425 K	0%	0%	0%	0%	0%
400 K	-64%	-39%	-37%	-39%	-35%
375 K	-88%	-47%	-36%	-17%	-18%
350 K	NO SEL	-81%	-44%	-40%	-39%

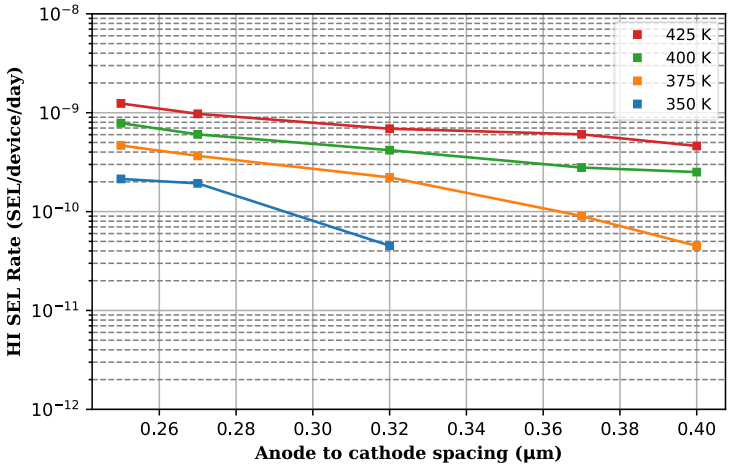

Figure 4.20 Heavy Ion SEL rate at GEO orbit versus the anode to cathode spacing for four different temperatures (350 K, 375 K, 400 K, 425 K).

Table 4.10 SEL rate difference at GEO orbit for the anode to cathode spacing, starting from 425 K.

	0.25 µm	0.27 µm	0.32 µm	0.37 µm	0.40 µm
425 K	0%	0%	0%	0%	0%
400 K	-37%	-38%	-39%	-54%	-46%
375 K	-40%	-39%	-47%	-68%	-82%
350 K	-54%	-47%	-80%	NO SEL	NO SEL

The second chosen orbit is the LEO orbit for ISS. The procedure is the same as for GEO orbit. In Figure 4.21, the doping profile variation is investigated. The trend is as in the GEO orbit. The highest relative difference is obtained in the best conditions, i.e. lower temperature and higher doping profile (Table 4.11). No difference is shown for the anode to cathode spacing. In Figure 4.22, the heavy ion SEL rate is shown and in Table 4.12 we show the value of the relative difference between the SEL rates. Again, for the best condition (higher spacing), the temperature effect is stronger compared to the lower spacing. Eventually, the trend for the well and substrate taps

distance is shown (Figure 4.23). As in the previous cases, the LEO orbit trend is similar to the GEO orbit.

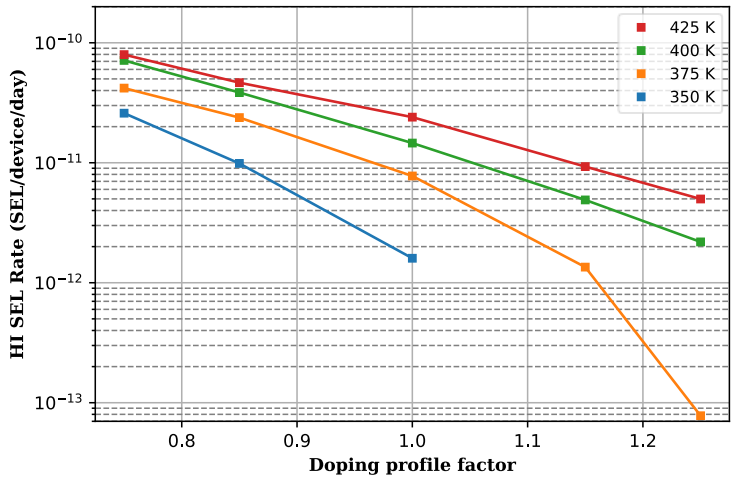

Figure 4.21 Heavy Ion SEL rate at LEO orbit versus the doping profile factor for four different temperatures (350 K, 375 K, 400 K, 425 K).

Table 4.11 SEL rate difference at LEO orbit for the doping profile variation, starting from 425 K.

	x0.75	x0.85	x1	x1.15	x1.25
425 K	0%	0%	0%	0%	0%
400 K	-11%	-17%	-39%	-47%	-56%
375 K	-41%	-38%	-47%	-72%	-96%
350 K	-38%	-59%	-79%	NO SEL	NO SEL

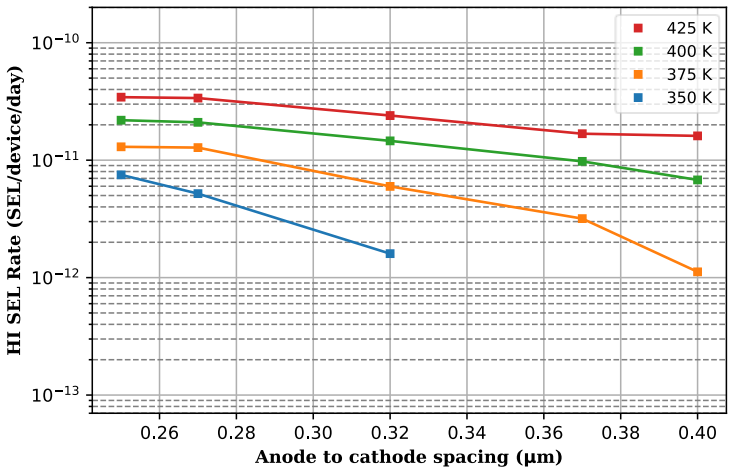

Figure 4.22 Heavy Ion SEL rate at LEO orbit versus the anode to cathode spacing for four different temperatures (350 K, 375 K, 400 K, 425 K).

Table 4.12 SEL rate difference at LEO orbit for the anode to cathode spacing, starting from 425 K.

	0.25 µm	0.27 µm	0.32 µm	0.37 µm	0.40 µm
425 K	0%	0%	0%	0%	0%
400 K	-36%	-38%	-39%	-42%	-58%
375 K	-41%	-39%	-59%	-67%	-84%
350 K	-42%	-59%	-73%	NO SEL	NO SEL

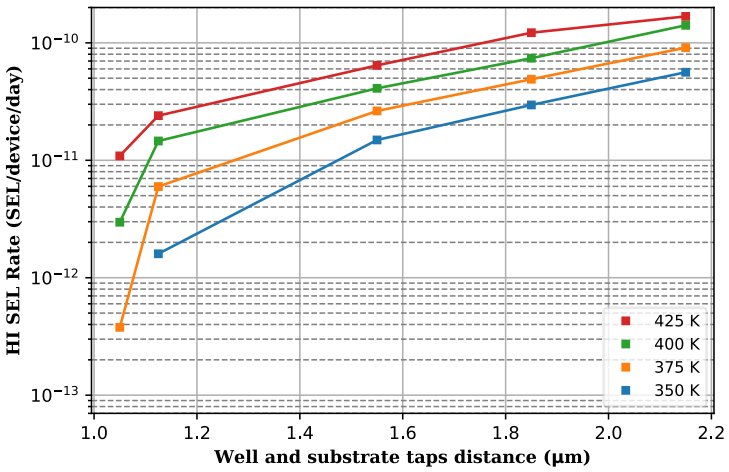

Figure 4.23 Heavy Ion SEL rate at LEO orbit versus the well and substrate taps distance for four different temperatures (350 K, 375 K, 400 K, 425 K).

Table 4.13 SEL rate difference at LEO orbit for the well and substrate taps distance, starting from 425 K.

	1.05 µm	1.25 µm	1.55 µm	1.85 µm	2.05 µm
425 K	0%	0%	0%	0%	0%
400 K	-73%	-39%	-36%	-39%	-16%
375 K	-87%	-59%	-36%	-34%	-35%
350 K	NO SEL	-73%	-43%	-40%	-38%

4.4 Discussion

We have seen from the results the impact of the design parameters and of the temperature on SEL sensitivity. In this section, we will discuss each parameter singularly but before that we need to recap the SEL triggering conditions. As aforementioned, the structure of the CMOS creates two parasitic bipolar transistors inside it. The activation of these transistors is the initial step for Single-Event Latchup. Hence, a parasitic circuit is created inside the structure as depicted by [42]. Certainly, the characteristic of the circuit is related to the design of the device and then, a variation of a

parameter leads to a variation of the response of the circuit and then to a variation on SEL sensitivity

We start with the doping profile. We have seen that if we increase the doping profile, the device becomes less sensitive to SEL. So, we will need an higher LET in order to trigger Single event Latchup. In the work of Rezzak *et al.* [64], the authors have analyzed the influence of the p-well and the n-well separately. The p-well doping profile will influence the NPN transistor gain and the substrate resistance by reducing them, meanwhile the n-well doping profile will influence the PNP transistor gain and the n-well resistance, also by reducing their values [90]. This has been seen experimentally in the work of Voldman *et al.* [91]. In addition, they have seen that the n-well has an higher impact on the threshold LET with respect to the p-well. In our case, we have modified the whole doping profile. Then, the two effects are combined and the same behaviour is found.

Also the A-C spacing has an impact on the SEL sensitivity. As the doping profile, modifying the spacing influences the transistor gain and the resistance of the device [64]. Also, by increasing the anode and the cathode contacts distance, the two parasitic transistors are decoupled. In this way, it is harder for one of the two transistor to trigger the second. This is confirmed by our results. As we increase the spacing, the threshold LET increases. However, the impact of A-C spacing is lower with respect to the doping profile. In fact, as reported in the work in Johnston *et al*. [43], the distance between the contacts modifies the resistance in the device logarithmically. So, its impact is lower with respect to the doping profile.

Eventually, the third parameter we have investigate is the well to substrate distance. This parameter influences the resistances in the device [64]. If the resistance is reduced, the SEL sensitivity of the structure will be reduced too [83]. Decreasing the distance between the well and substrate contacts, will reduce the resistance. Then, in order to cause a potential drop sufficient to trigger the parasitic transistors, as the resistance reduces, we need an higher current. In fact, our results show that as we decrease the distance, the threshold LET increases.

However, the main goal of this work is to prove this trend also for higher LET. In previous works, the analysis has been performed by investigating only the threshold LET. Meanwhile, by calculating the cross section, we are able to confirm that the trend is equivalent also with an higher LET and is visible for all the three parameters. In addition, we have evaluated the impact of the parameter variation on the sensitivity. According to our simulations, we have seen that for a small variation of doping profile and of well and substrate taps placement, there is a sensible variation of SEL immunity, meanwhile a variation of A-C spacing is less relevant. This aspect can be taken into consideration in the design phase of a component or in the simulation process. Especially when performing simulations, most of the time the exact doping profile is not available and this can lead to a wrong prediction of SEL immunity. Moreover, concerning the design phase, all these methods can be used for hardening the component, but all come with drawbacks. In fact, increasing A-C spacing or substrate and well taps placement leads to an area penalty, whereas variation of the doping profiles may not be possible because of process related issues. So, a compromise must be made for the hardening of the CMOS components.

On the second part of this work, we have investigated the effect of temperature. In this case, we have combined the effect of the temperature variation with the variation of the three parameters (doping profile, A-C spacing, W-S distance). In this way, we could measure the impact of temperature for different kind of device solutions. As we have seen, SEL sensitivity is dependent to a combination of all the effects of the layout parameters. However, this work shows that for all the parameters (doping profile, substrate and well taps placement and A-C spacing) temperature has a more relevant impact on the variation of threshold LET and SEL rate for the best-case scenario, with respect to the worst-case scenario. On first consideration, we can say that in the best-case scenario, conditions are already favorable to SEL immunity and then the decrease of temperature will help to increase SEL immunity of the device. Meanwhile, in the worst-case scenario, the device situation is already on SEL favor. Then, temperature will have a lower impact on SEL sensitivity.

In conclusion, it is important to remark that the temperature impact has to be considered not equal in all conditions and it is not independent from device design. This information can be useful whenever a device is facing different temperature conditions.

4.5 Conclusion

In this chapter, a comparison between the effects on SEL sensitivity from four different parameters has been made. Cross sections for each parameter have been calculated using 2D TCAD simulations. This approach allows to perform fast simulations and to calculate an important value to estimate SEL sensitivity.

First, we have investigated the effects of temperature on SEL sensitivity. As demonstrated in other works, we have shown that for higher temperatures, the SEL sensitivity increases. Similarly, the increase of doping profiles increases the SEL sensitivity while increasing A-C spacing decreases it [Figure 4.24]. Then, we observed that doping profiles variations have a stronger impact on SEL sensitivity compared to A-C spacing variation. Eventually, we have shown that substrate and well taps location has a similar impact as doping profiles variation to latchup sensitivity. This result is highly important in design phase to decide which strategies can be adopted to harden the component.

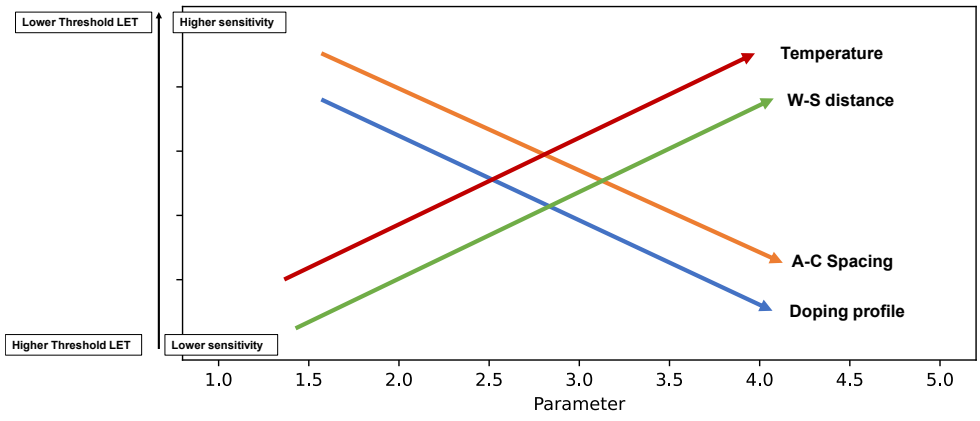

Figure 4.24 Recap of the parameters influence on SEL sensitivity.

Then, we have investigated the effect of temperature on four different parameters. Cross-section curves for each parameter have been calculated using 2D TCAD simulations and then SEL rate for GEO and LEO orbits has been estimated from these curves. For each parameter, we have modified its value and then for each single case we have investigated temperature effects, for a chosen temperature range. At first, threshold LET is investigated. We have observed, for every case, that when the component is less sensitive to SEL, temperature has a stronger impact on threshold LET, with respect to the opposite case. To further investigate this trend, we have calculated SEL rate for the GEO and LEO orbits. Indeed, the same trend has been observed for SEL rate.

Chapter 5

Single Event Latchup prediction using TCAD and SPICE simulations

In Chapter 2, we have analyzed the basic mechanism of Single Event Latchup. Understanding the mechanism of SEL is crucial when the goal is prediction of the event. Unfortunately, there is a lack of literature that explains the details of Single Event Latchup mechanism. Then, one of the goal of this chapter is to address this problem and contribute to provide a detailed overview of the electrical behavior of Single Event Latchup. To do it, we have analyzed the current at the five different terminals of the device. In this way, we could investigate the different steps that are taking place in Single Event Latchup. Once we have obtained this information, we have used it to design a SPICE circuit, that is able to mimic Single Event Latchup in SPICE simulations. This circuit can be used for prediction of SEL via SPICE.

On the other hand, in Chapter 4 we have seen that different values of LET are needed to trigger SEL, depending on the position. In fact, in the work of Johnston *et al.* [43] they show that the n-well/p-substrate junction is the most sensitive area for Single Event Latchup. Then, the sensitivity to SEL is dependent on the position. So, we have decided to investigate it further. Instead of using a classic long ion track, we have decided to inject charges due to radiation in a precise point of the structure (that we call *short track*). In this way, we could precisely calculate the sensitivity associated to a specific point and compare it with others points in the structure.

The structure of the chapter is the following. First, we will discuss about the setup of the simulations we have performed. Then, we will analyze the results of the simulations and we will discuss about the dynamics of SEL. Consequently, we will compare the results by simulating a short track with respect to a long track and then, we will compare the results obtained by

two different TCAD tools, Sentaurus and ECORCE. Eventually, we will introduce our model for SPICE simulation. In the second part of the chapter, we will present the simulations we have performed about the different sensitivity depending on the position.

5.1 Prediction of SEL using TCAD and SPICE simulations

As we mentioned, the details of Single Event Latchup mechanism are not always disclosed. Thus, in this section, the goal was to simulate SEL in PNPN structure with TCAD tools. We have extracted the current and we have analyzed their shape in order to understand the steps that leads to SEL. Then, to validate this steps we have compared these results with a different TCAD tool, ECORCE, and different configurations of ion track. The last goal was, starting from TCAD simulations, to design a model circuit in SPICE, that is able to perform the same steps found in TCAD simulations. Eventually, this circuit could be used for SEL prediction.

Before we move on to the mechanism, we give the characteristics of the simulations we have performed and some clarifications about some concepts that we will use in the following chapter.

5.1.1 Simulated structure and short track

The simulated structure is similar to the one in section 4.1.1. It is a PNPN structure, formed by five terminals: the p-substrate (BP+), the n-source (SP+), the n-well (BN+), the p-source (BP+) and the substrate (Sub). The component has a width of 2.3 μm and a depth of 0.88 μm. As for the previous structure, the doping profiles is based on a commercial bulk 65nm process.

As explained in 3.1.1.2, the ion track is defined, among the others parameters, by its length. Usually, this value is the range of the particle on the device and it can be obtained by other tools, as SRIM [33]. In SRIM, it is possible to select an ion, simulates its passage through a specific material to obtain the range of this ion in the material. The range is then used as the length in Sentaurus. If the goal of the simulations is to study the effects of a

specific ion, this is the process to use. However, the scope of this chapter is not to investigate a specific ion, but to study the dynamics of Single Event Latchup. For this reason, we used what we called a "short track" (Figure 5.1). Instead of using a range value obtained by SRIM for a specific ion, we have used a constant and short range of 10 nm. In this way, we could target a specific point of the structure and eliminate the influence of other parts of the structure. We have selected different points, named by letters. These points are highlighted in Figure 5.2. The points A, B and C are placed in the p-substrate, meanwhile point G, H, I are in the n-well. In the Table 5.1, the coordinates of the points are shown.

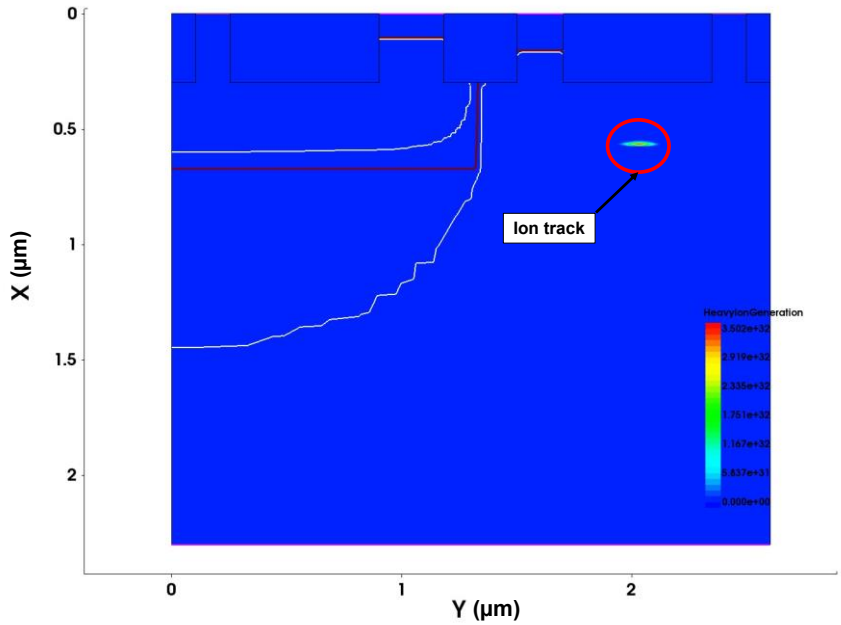

Figure 5.1 Heavy ion generation in Sentaurus. Circled in red is the ion track in point B.

5.1.2 Current sign

Due to the fact that in the next section we will show current plots, another aspect to clarify is the current sign convention in the simulation. As per definition, the current is the movement of charged particles (either electrons or ions) through an electrical conductor or space and it is calculated as the net rate of flow of electrical charge through a surface. The

conventional direction of the current is defined as the direction in which positive charges flow. Then, when negative charges are involved, the sign of the current is opposite to the sign of the flow.

So, based on this definition we define the current signs in our simulations. As represented in Figure 5.3, when the current is positive, if electrons are involved the contact is collection electrons, meanwhile, holes are injected. The opposite happens when the current is negative (Figure 5.4). When holes are involved, there are collected by the contact, meanwhile electrons are injected.

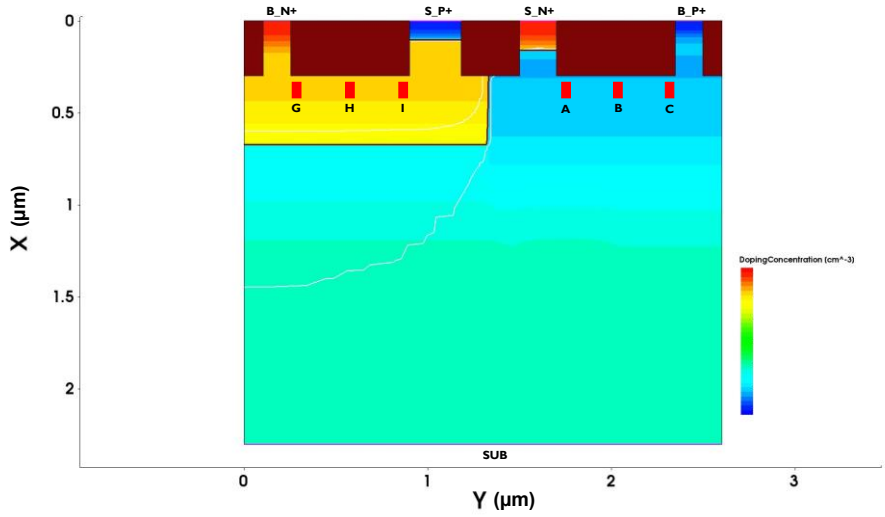

Figure 5.2 The injection points (red rectangles) highlighted in the PNPN structure

Table 5.1 Coordinates of the points used in the simulations.

	x (µm)	y (µm)		x (µm)	y (µm)
A	0.31	1.74	**G**	0.31	0.30
B	0.31	2.03	**H**	0.31	0.59
C	0.31	2.32	**I**	0.31	0.88

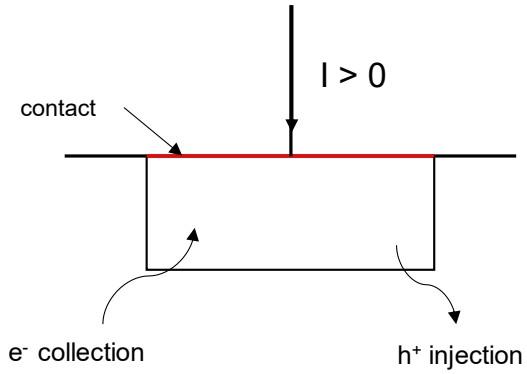

Figure 5.3 Convention sign when I>0.

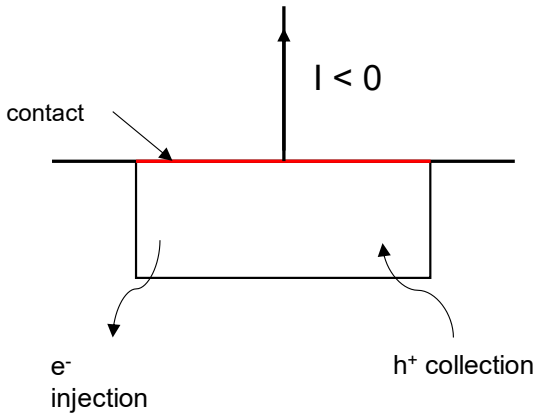

Figure 5.4 Convention sign when I<0.

5.1.3 Single Event Latchup mechanism

In order to analyze the mechanism of Single Event Latchup, we have registered the current at the five terminals. To be more specific, we have considered the electron and the hole currents. In this way, we could analyze the activation of the parasitic transistors that are involved in Single Event Latchup. Before moving on to the charts, for sake of clarity, in Figure 5.5 we show an example of the chart we will see in the next pages. On the left of the chart, it is written the contact in which the current is measured. Then two charts per contact are shown: the electron current, on the left, and the hole current, on the right. On the top of the chart, it is written the point in which the ion is injected (i.e. Point B). To represent the different phases of SEL

mechanism, in each chart, three different currents are shown. First of all, we are interested in what happens at the threshold LET for SEL for that specific position. So, the green curve represents the current when a SEL occurs. Instead, the orange curve represents the current when no SEL occurs, right below the threshold value. The difference between the two values is 0.001 pC/µm, which is also the accuracy. A third curve is shown, colored in blue. This curve represents when no SEL occur, but for a lower LET value. The reason for this curve is to show the behavior of the two transistors for lower LET and it will be explain in the following pages.

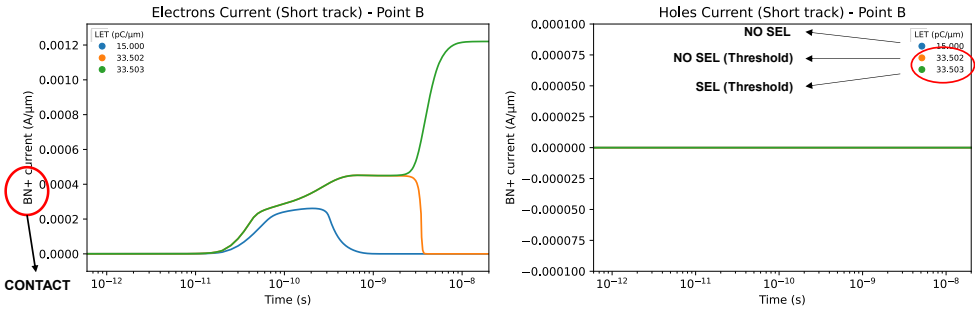

Figure 5.5 Example of the current charts. On the left of the chart we show the contact. Then, three different LET are used.

Once we have explained the charts, we can see the complete plot, with the current at the five terminals. In this case, we have analyzed an ion injected in the n-well in the B position (Figure 5.6) and an ion injected in the p-substrate in the H position (Figure 5.7). The first thing to notice is that the hole current of BN+, the electron current of BP+ and Sub, is zero (expect a small current for point B at low LET). This is due to the fact that these are the base and the collector of the parasitic transistor. So, the only current is passing by is due to the majority carrier in that terminal. So, for instance, BN+ is the contact of the n-well, and so only electrons will be present. Vice versa, BP+ is the contact of the p-substrate and then, mainly holes will be present.

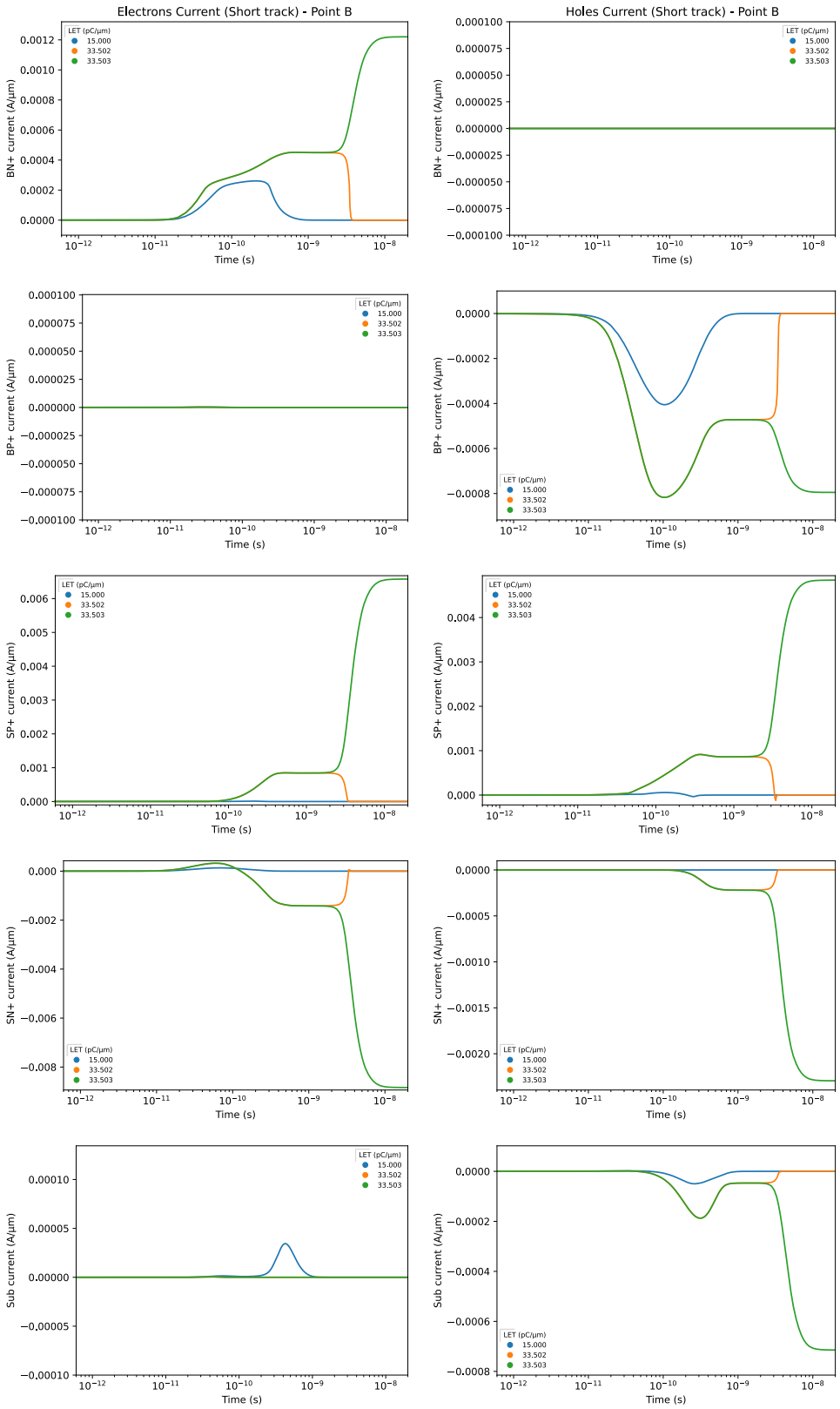

Figure 5.6 Complete current charts for point B.

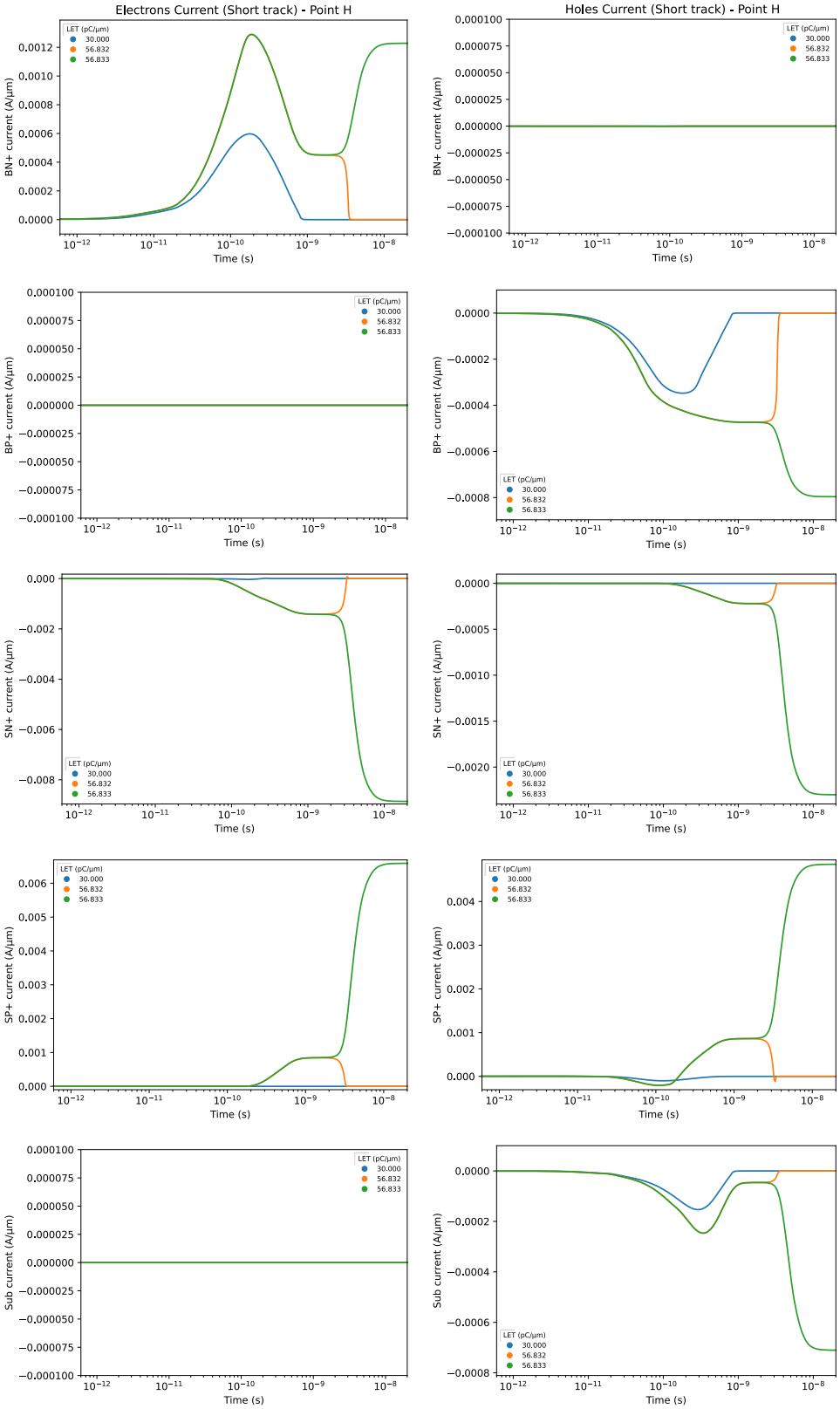

Figure 5.7 Complete current charts for point H.

Now, we will discuss the different steps of SEL, considering the two points, B and H. The other point will be shown in appendix, as they have the same behavior.

- **Step 1**

The initial time of the ion injection is at 10^{-12} *s.* After the ion impact with the device, **an initial current flows between BN+ and BP+**. To clarify this, we magnify the chart related to these terminals. We can see this behavior for all the three values of LET calculated in our simulations, for both point B and point H (Figure 5.8 and Figure 5.9, respectively).

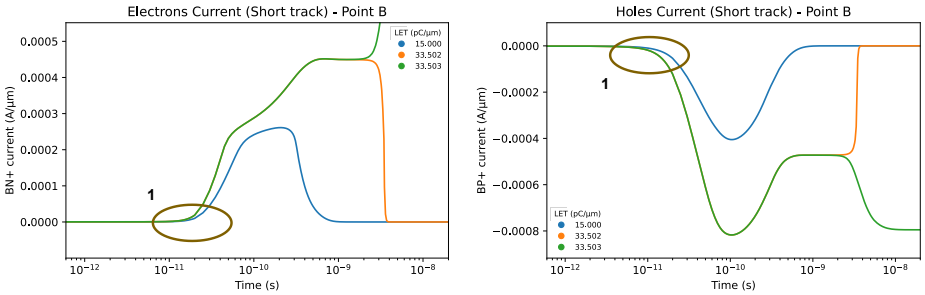

Figure 5.8 BN+ electrons and holes current for point B. Step 1 is circled.

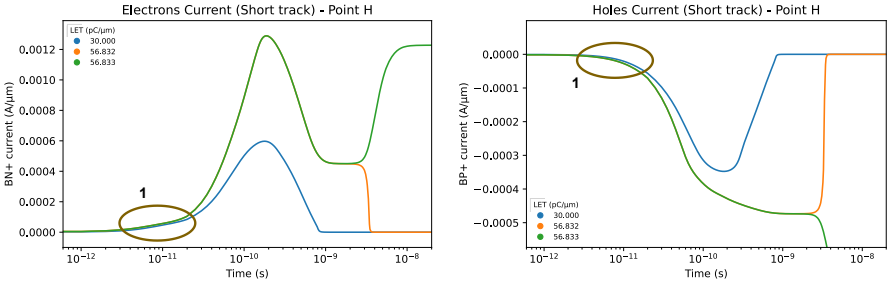

Figure 5.9 BP+ electrons and holes current for point H. Step 1 is circled

- **Step 2**

Once this flow starts, we can see **the activation of one of the transistors around 6x10^{-11} s**. The identity of this transistor will depend on the location of the ion impact. For point B (ion in the n-well) the first transistor to activate is the PNP transistor, starting from the SP+. Indeed, the hole current of the SP+ is rising and it is positive (Figure 5.10). Because, the SP+ is the emitter of the PNP transistor and a positive current means injection of holes in the device, so the PNP transistor is activated. At the same time, the emitter of the second parasitic transistor, the NPN, is not active and it is collecting electrons.

For point H, the first transistor to activate is the NPN. This is visible in Figure 5.11. As for the previous case, there is an initial increase in the current. In this case, SN+ is injecting electron in the device, and so the current is negative. In both cases, the initial current is due only to the major carrier, then holes for SP+ and electrons for SN+. Also, for low LET the current increases (whether is positive or negative) but after few hundredth of picoseconds it returns to zero.

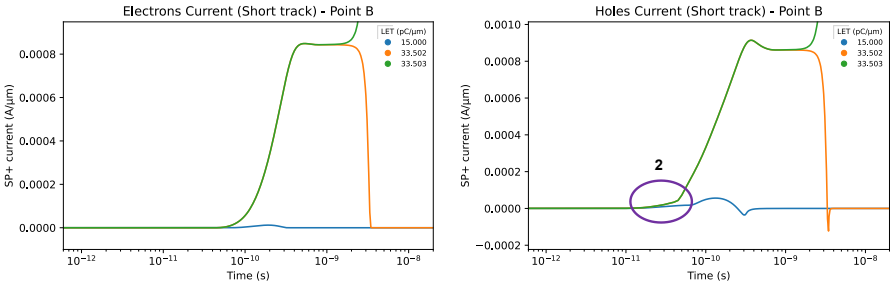

Figure 5.10 SP+ electrons and holes current for point B. Step 2 is circled.

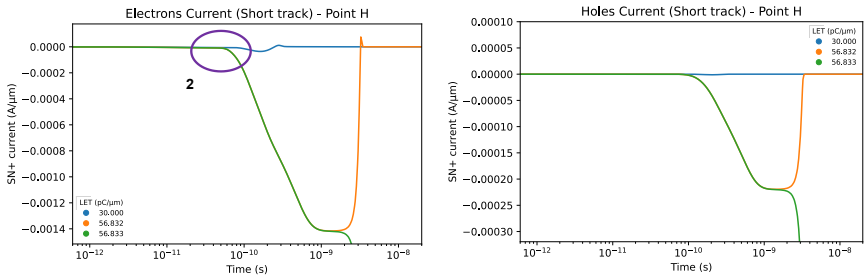

Figure 5.11 SN+ electrons and holes current in point H. Step 2 is circled.

- **Step 3**

In Figure 5.12, for point B, we can see that the electron current of SN+ is positive at first. Recalling the sign convention, it means that **the SN+ electrode is collecting electrons**. At around $2x10^{-11}$ *s*, the current switches to negative (Step 3*), meaning the injection of electrons in the device and then, the activation of the NPN transistor. However, the same behavior is not observed for low LET. In this case, there is an initial collection of electrons, but then the current returns to zero and the NPN never activates.

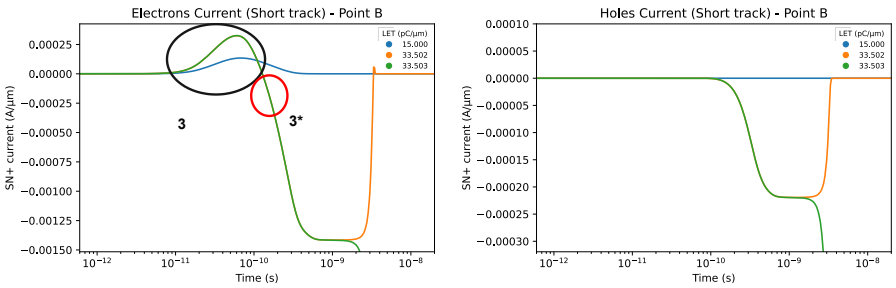

Figure 5.12 SN+ electrons and holes current for point B. Step 3 and Step 3* is circled.

In Figure 5.13, we show the current for SP+ and point H. The behavior is specular to what happen in point B. Here, the SP+ is collecting holes (negative current), and then, at the threshold, switches to positive current (so injection). Instead, for low LET, as in the previous case, the SP+ collects holes and then it returns to zero, so it never activates.

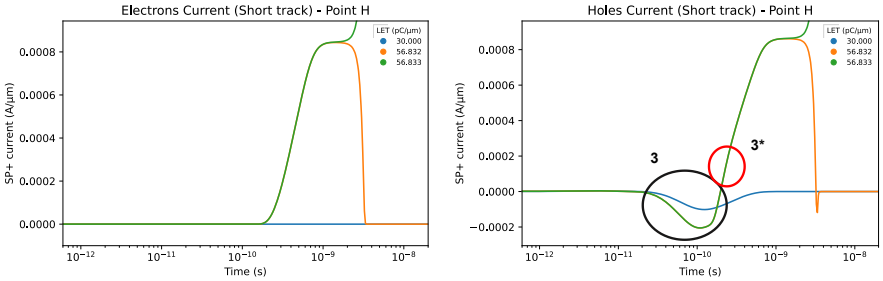

Figure 5.13 SP+ electrons and holes current for point H

- **Step 4**

Once both transistors are active, the two transistors create a regenerative loop that sustain each other. **For point B**, we can see that **the hole current at SN+ increases at the same time (around $2x10^{-10}$ s) when the electron current switches from positive to negative**. This is due to the activation of the other transistor. At the same time, at SP+, when the loop is on, the electron current increases.

For point H, the situation is the opposite. After Step 3*, the SP+ hole current switches from negative to positive. At the same time, **the SP+ electron current increases**. Vice versa for SN+, which is active from Step 2, the electron current continues to increase, meanwhile the hole current starts after the activation of the second transistor.

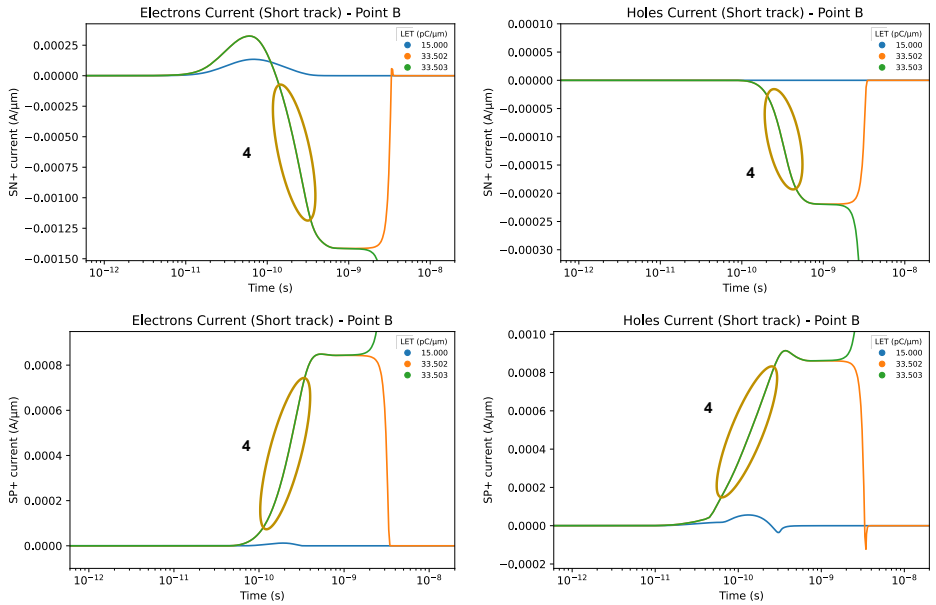

Figure 5.14 SN+ electrons and holes current on the top, and SP+ electrons and holes current on the bottom for point B. Step 4 is circled.

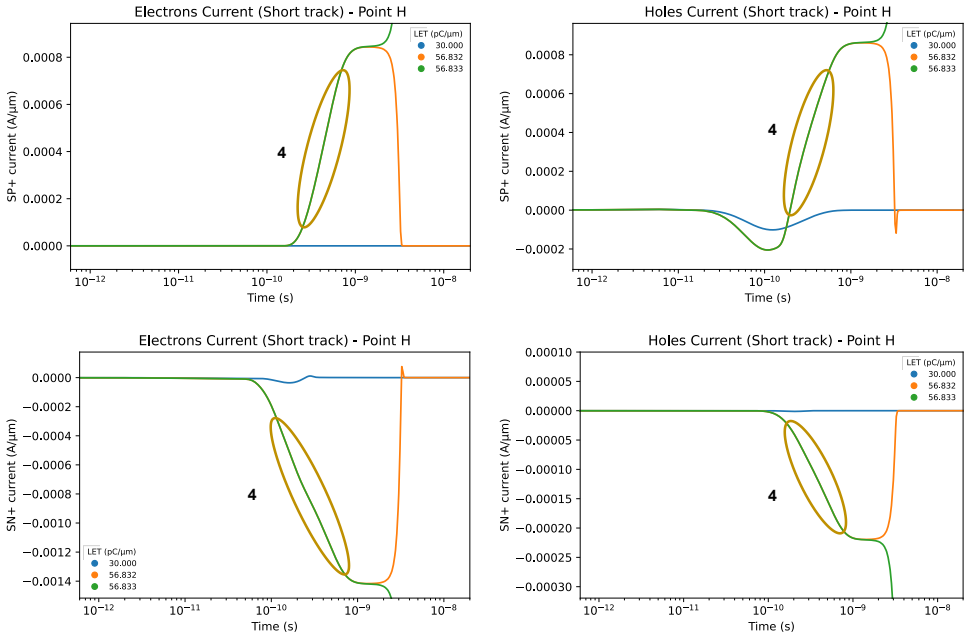

Figure 5.15 SP+ electrons and holes current on the top, and SN+ electrons and holes current on the bottom for point H. Step 4 is circled.

- **Step 5 and Step 6**

After Step 4, the current in all the contacts increases, but it doesn't increase indefinitely. Around $8x10^{-10}$ s, the currents reach a plateau. The two transistor reached saturation but **the SEL is not occurred yet**. The same happens for point B and point H. Indeed, at around $2x10^{-9}$ s, if the loop established at Step 4 is still sustained, the SEL will occur (green curve in Figure 5.16, Step 6_A). Meanwhile, if the electrical conditions are no longer sufficient to sustain the loop, the SEL will not occur (orange curve in Figure 5.16, Step 6_B).

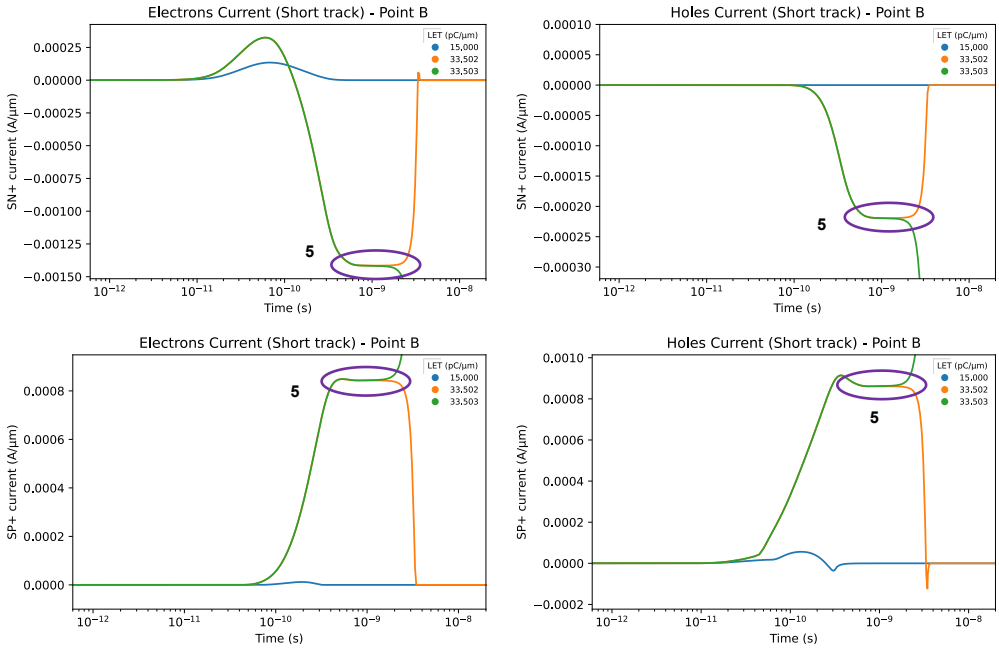

Figure 5.16 SN+ electrons and holes current on the top, and SP+ electrons and holes current on the bottom for point B. Step 5 is circled.

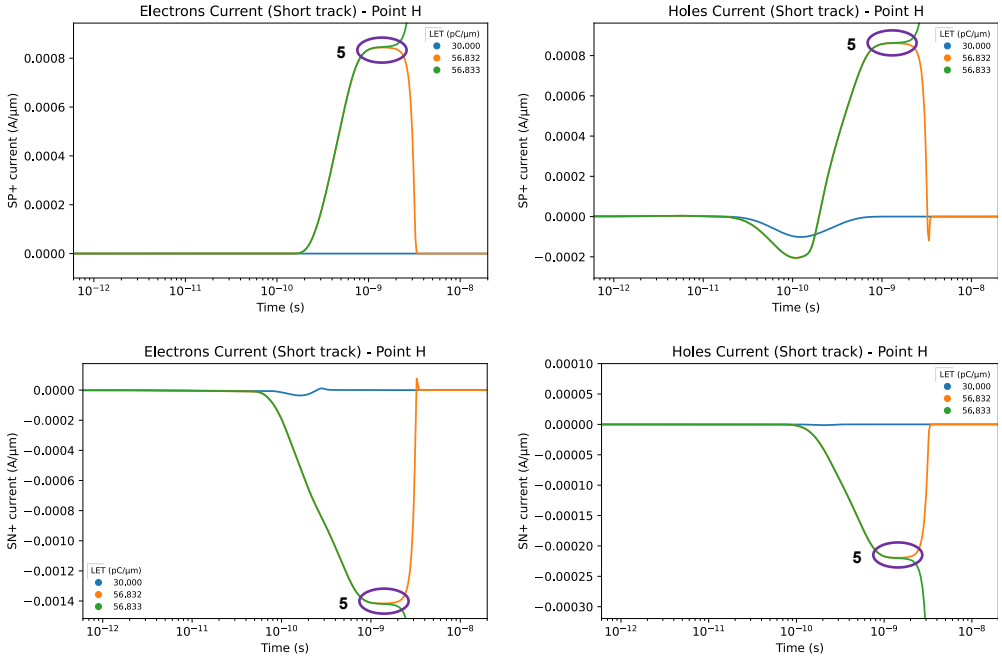

Figure 5.17 SP+ electrons and holes current on the top, and SN+ electrons and holes current on the bottom for point H. Step 5 is circled.

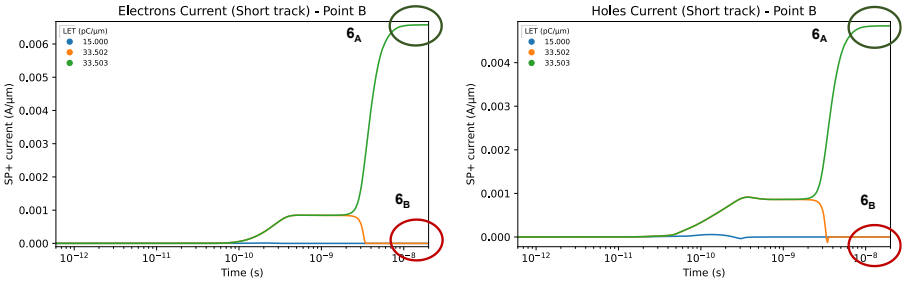

Figure 5.18 SP+ electrons and holes current for point B. Step 6_A and 6_B are circled.

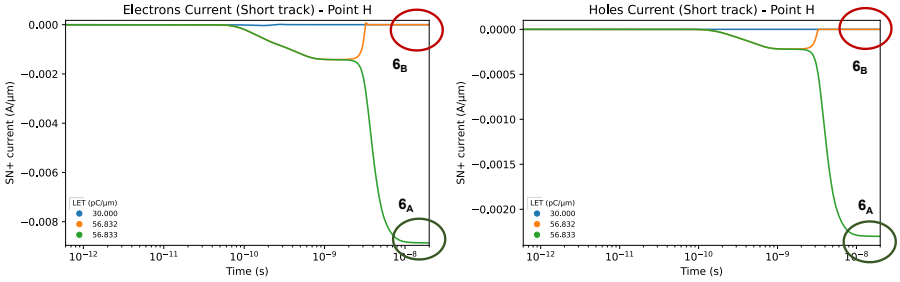

Figure 5.19 SN+ electrons and holes current for point B. Step 6_A and 6_B are circled.

5.1.4 Comparison between Sentaurus and ECORCE

Once we have analyzed the different steps of SEL with Sentaurus, we have decided to compare these results, with another TCAD tool, ECORCE (see section 3.1.2). In this way, we could investigate if the same steps are found, if another tool is used. The structure of the device is the same as in Sentaurus. However, some difference on the doping profile is present due to the different insertion methods present in the two software. Moreover, the ion track is the same as in Sentaurus and it is injected in point B (see Figure 5.2). More differences are present due to the physical models used in the simulation. In fact, not every model used in Sentaurus is present in ECORCE. Then, where possible, we have used the same physical models, otherwise the model was not included in the ECORCE simulation. In addition, in this case we will analyze just the current at the threshold and the LET value at threshold is different in the two tools.

- **Step 1**

The ion impacts with the device at 10^{-12} s in point B. As in Sentaurus, a current starts to flow in BN+ and BP+. However, a small difference between Sentaurus and ECORCE is found about the time evolution and it will be clearer for the other steps. For Step 1, the difference is small. For Sentaurus, the current increases around 10^{-11} s, meanwhile for ECORCE is around $2x10^{-11}$ s. It has to be said that, a different amount of charge is injected in the device. This may be due to the different models available in ECORCE and to the small difference for the doping profile. Then, this could be the cause of the small discrepancy in the timing.

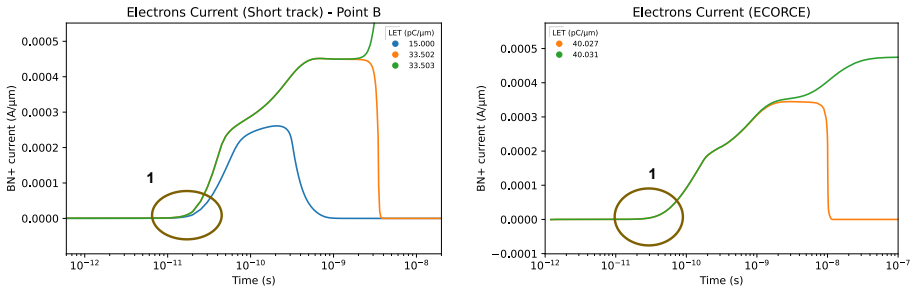

Figure 5.20 BN+ electrons current in Sentaurus (left) and ECORCE (right). Step 1 is circled.

- **Step 2**

For Step 2 the different timing becomes more clear. There is an initial increase in current, that, as we mentioned, means the activation of the PNP transistor. However, in Sentaurus the first increase last from 10^{-11} s to $4x10^{-11}$, meanwhile in ECORCE it starts around 10^{-11} s and finishes around $2x10^{-10}$ s. So, this step lasts longer in ECORCE.

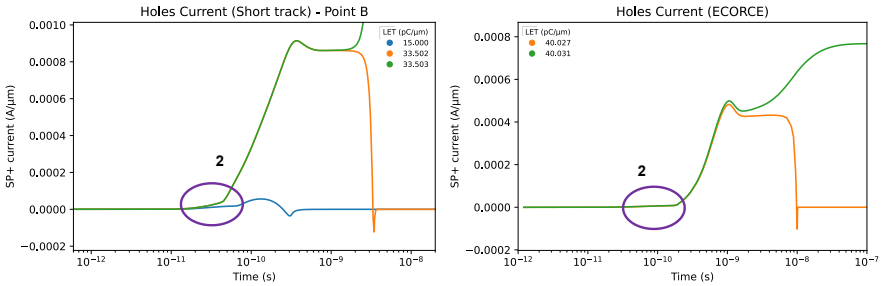

Figure 5.21 SP+ electrons current in Sentaurus (left) and ECORCE (right). Step 2 is circled

- **Step 3**

As we have seen, Step 3 involves the activation of the second transistor (NPN in this case). With ECORCE we obtain the same tendency for current SN+. But again, timing is different. In Sentaurus the switch between collection and injection happens around $1.1x10^{-10}$ s, meanwhile for ECORCE the switch is at $5x10^{-10}$ s.

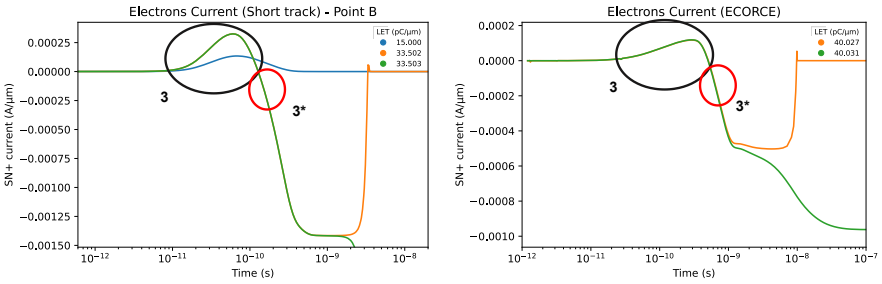

Figure 5.22 SN+ electrons current in Sentaurus (left) and ECORCE (right). Step 3 is circled

- **Step 4, Step 5 and Step 6**

Step 4, 5 and 6 are found to be similar between Sentaurus and ECORCE. However, as seen for the other steps, timing is not the same. For instance, we can see that Step 5 finishes at around $3x10^{-9}$ s for Sentaurus, meanwhile in ECORCE it finishes at 10^{-8} s.

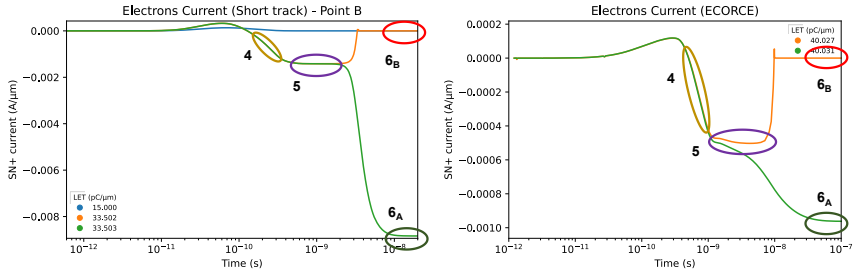

Figure 5.23 SN+ electrons current in Sentaurus (left) and ECORCE (right). Step 4, 5 and 6 are circled

However, despite the timing difference, that may be caused by the small difference between the two tools, the SEL steps are the same whether we use Sentaurus or ECORCE.

5.1.5 Comparison between short track and long track

In the previous sections, we have used a so called "short track" to analyze the dynamic of SEL. The short track allows us to target a specific position and to isolate as much as possible, the effects of the ion itself. However, the short track that we used is not representative of what a real ion can do in the device. Then, we have compared the steps discussed for the short track, with the one of the long track. Specifically, we have compared the short track in point B with a long track that traverses the full device length at the y value of point B (Figure 5.24). Also for the long track, we have determined three LET values where to extract the current. A LET value well above the threshold (blue curve) and two values at the threshold; one when the SEL occurs (green curve), and one when it does not occur (orange curve).

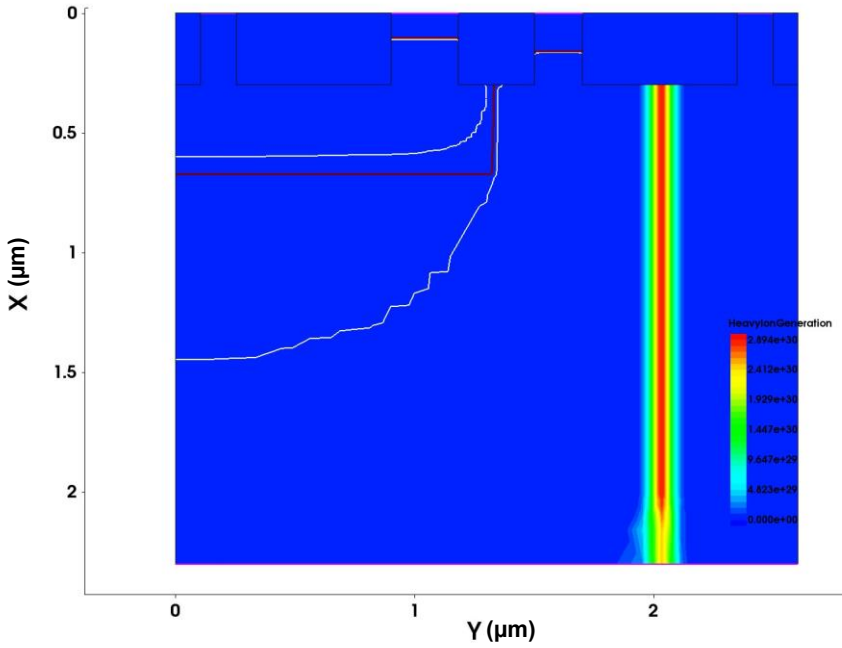

Figure 5.24 Heavy ion generation in Sentaurus for the long track. The red line is the ion track generated by the software.

We will compare just point B and not point H. The reason is that a long track at point H would generated electron-hole pairs both in the n-well and in the p-substrate, meanwhile the short track generates charges just in the n-well. So, a comparison would not possible as electron-hole pairs would be

generated in two different locations, with two different doping. Meanwhile, for point B, both the short and long track configuration would generate charges inside the same location (the p-substrate), making meaningful the comparison between the two configurations.

- **Step 1**

As for the short track, after the ion impact with the device, the current starts to flow in the contact BN+ and BP+. In Figure 5.25, we can see the comparison between the short track (on the left) and the long track (on the right, for BN+ electrons current and in Figure 5.26 the BP+ holes current.

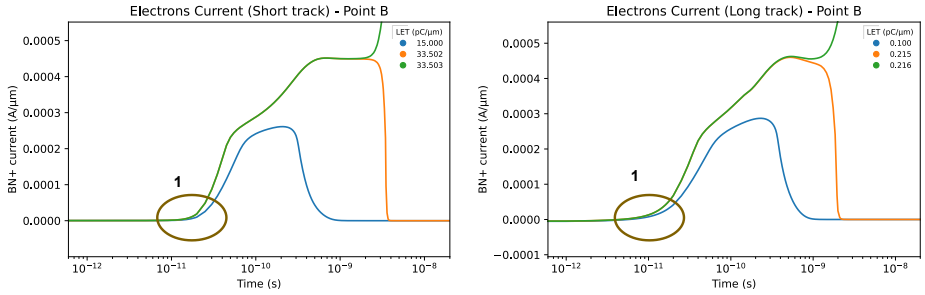

Figure 5.25 BN+ electrons current for the short track (left) and long track (right) for point B. Step 1 is circled.

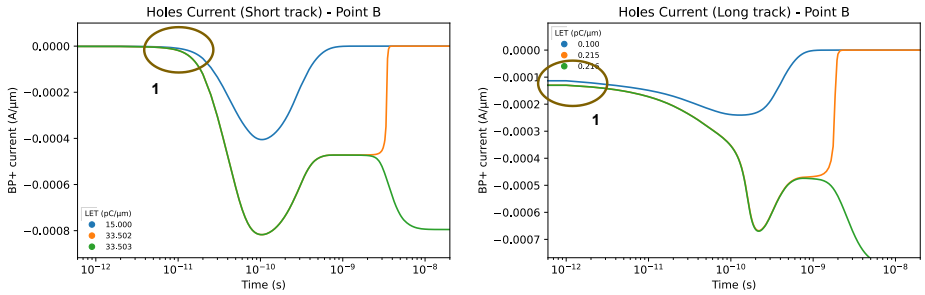

Figure 5.26 BP+ electrons current for the short track (left) and long track (right) for point B. Step 1 is circled.

- **Step 2**

Once the flow starts, the first transistor activates. As the ion impact in the substrate, the first transistor to activate is the PNP, as it happens for the short track. We can see from Figure 5.27 that the time evolution of the

current is similar between the short track and the long track, as well as the magnitude of the current.

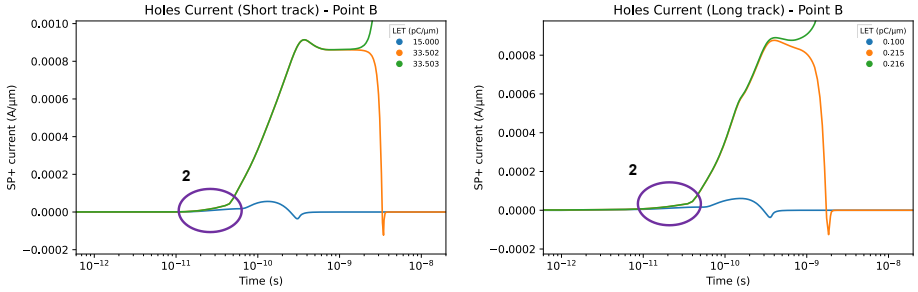

Figure 5.27 SP+ holes current for the short track (left) and long track (right) for point B. Step 2 is circled.

- **Step 3**

After the PNP transistor activates, the NPN transistor collects electron and then it turns on. Also for this step, the behavior between short track and long track is the same. The collection starts at approximately the same timestep, and the current magnitude is of the same order.

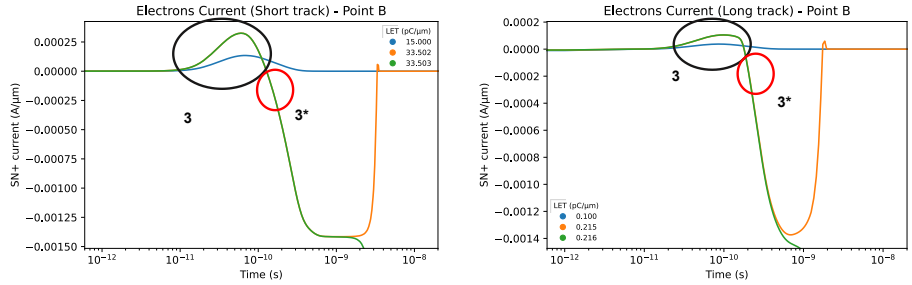

Figure 5.28 SN+ electrons current for the short track (left) and long track (right) for point B. Step 3 is circled.

- **Step 4**

Once the two transistors activate, as we have seen in the short track, it follows a current increase for all the four terminal. For sake of space, we show it just for SN+.

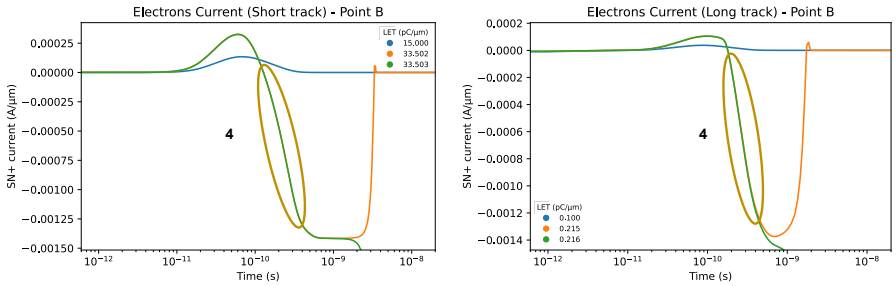

Figure 5.29 SN+ electrons current for the short track (left) and long track (right) for point B. Step 4 is circled.

- **Step 5 and Step 6**

The only difference between the short track and long track is found on Step 5. In the short track, a plateau is reached. Instead, in the long track, the plateau is reached and maintained very shortly (BP+) or is not maintained (all the other contacts). However, what is not different, is that this step is crucial for SEL. In facts, it is at this step that the device will either turn off (Step 6_A) or will starts a SEL (Step 6_B).

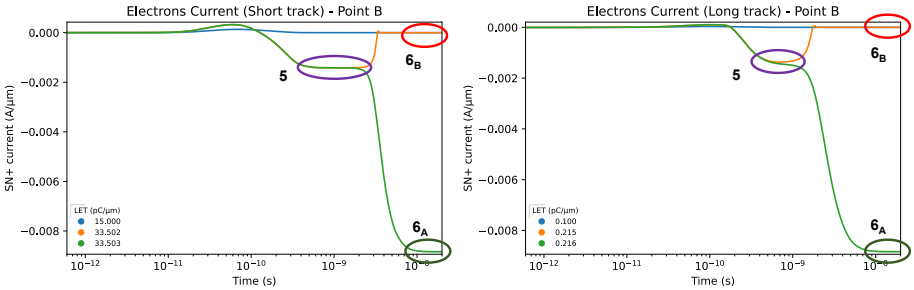

Figure 5.30 SN+ electrons current for the short track (left) and long track (right) for point B. Step 5 and 6 are circled.

In conclusion, there is no much difference between the short track and the long track configuration. Even though, the short track is not representative of a real ion, it gives a good idea of the steps that are involved in SEL it allows to select a specific target and it is simpler to simulate

5.1.6 Single Event Latchup electrical simulations with SPICE

In the first part of this chapter, we have discussed and analyzed the different steps that lead to SEL in a device. In this part, we are going to study how we can predict SEL based on the knowledge acquired in the previous section. To do so, we have used SPICE simulations (see 3.2).

So far, we had a look just at the current at the electrodes. However, one key point to determine if the circuit will trigger or not is to model the way the charges produced by a particle are injected in the circuit. In Figure 5.31, we show the PNPN structure with the different current names for the five existing electrodes. The green areas indicate the depletion layers (at least initially) and therefore the zones where there is an electric field likely to separate the

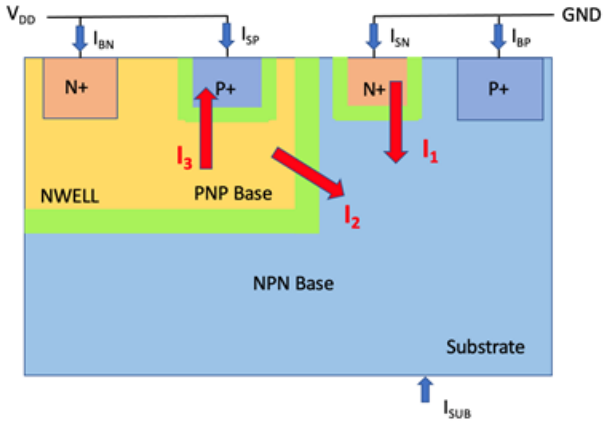

Figure 5.31 PNPN structure showing the electron-hole pair separation and the electrode currents. Green zones represent depletion layer. I_1 , I_2 and I_3 are the currents due to separation of electron-hole pairs.

electron-hole pairs created by an ionizing particle. The first zone is located at the junction between the substrate and the N+ region. For this zone, the separation of pairs will generate a current between the substrate and the N+ region (I_1). This current appears when electron-hole pairs are created in the substrate. Similarly, if electron-hole pairs are created in the NWELL region, they can be separated at the P+/NWELL junction (corresponding to emitter and base of the PNP transistor) leading to the current named I_3. In any case,

the Substrate/NWELL junction will separate the pairs leading to a current flowing from the PNP base to the NPN base. This current is named I_2. These three current sources can be added to our circuit to model the passage of a particle in the structure. The resulting circuit modeling is given Figure 5.32. In this circuit, we have used two well known transistors, 2N2222A and 2N2907A. Even though they are not representative of a real CMOS circuit, they are very useful to understand the triggering of SEL.

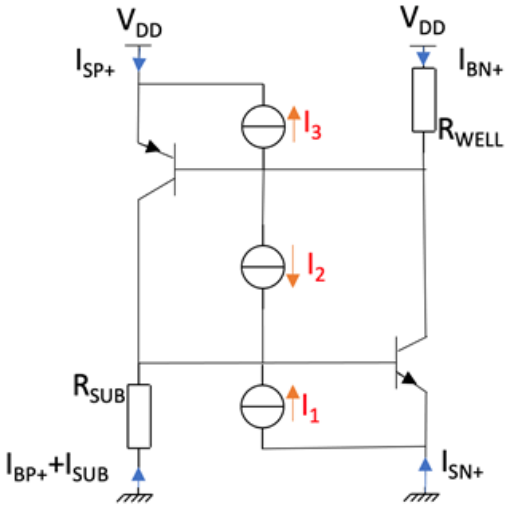

Figure 5.32 Schematic circuit of the PNPN structure. I_1 , I_2 and I_3 represent the injection of charges at the junctions (electron-hole pair separation)

Once the equivalent circuit is determined (Figure 5.32) we need to use a pulse current in each of the three source currents. For simplicity, we consider that the ion is in the substrate. Consequently, only I_1 and I_2 are at play and we investigated the case when they are equal (meaning that the ion track is approximately at the same distance from both depletion region). Moreover, we consider rectangular pulses as represented in Figure 5.33 and we may vary the amplitude of the pulse to investigate different situations. The first situation is when the amplitude is just enough to trigger an SEL (this is called threshold). The second one is just below the threshold and the last one is well below the threshold.

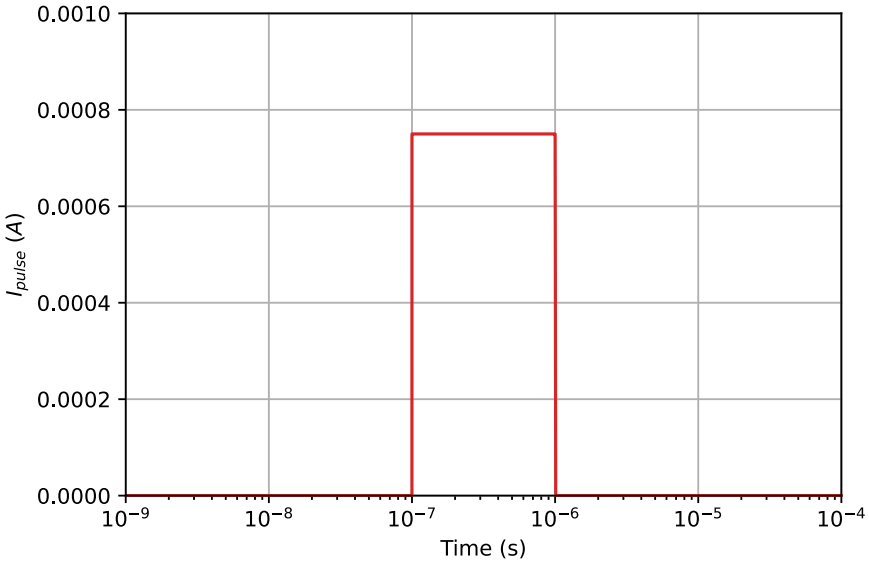

Figure 5.33 Pulse current used in our SPICE simulations in order to mimic the electron-hole pair separation. Threshold is obtained by varying the amplitude of the pulse.

The left side of Figure 5.34 plots for the three situations, the four currents of interest in the circuit, the currents at the terminals. In order to validate our modeling, the shapes of these currents can be compared to Sentaurus simulations that are reported in the right side of Figure 5.34. Despite some discrepancies, the currents exhibit the same trends in the three conditions. It shows that our modeling together with an injection of simple pulses in the structure can reproduce the complex behavior of the parasitic circuit. However, some improvement is necessary for this model. First, we would need a more realistic pulse current generated by the ion. In particular, the amplitude and the pulse width of the pulses must be representative of the ion kind of the location of the track. For this purpose, we would think that ambipolar diffusion model could be used for this scope. The ambipolar diffusion expresses the density of electron-hole pairs as a function of time [92]:

$$n(r,t) = N_0 \frac{e^{-\frac{r^2}{4Dt\tau}}}{(4\pi Dt)^{3/2}} \qquad \text{Eq. 5.1}$$

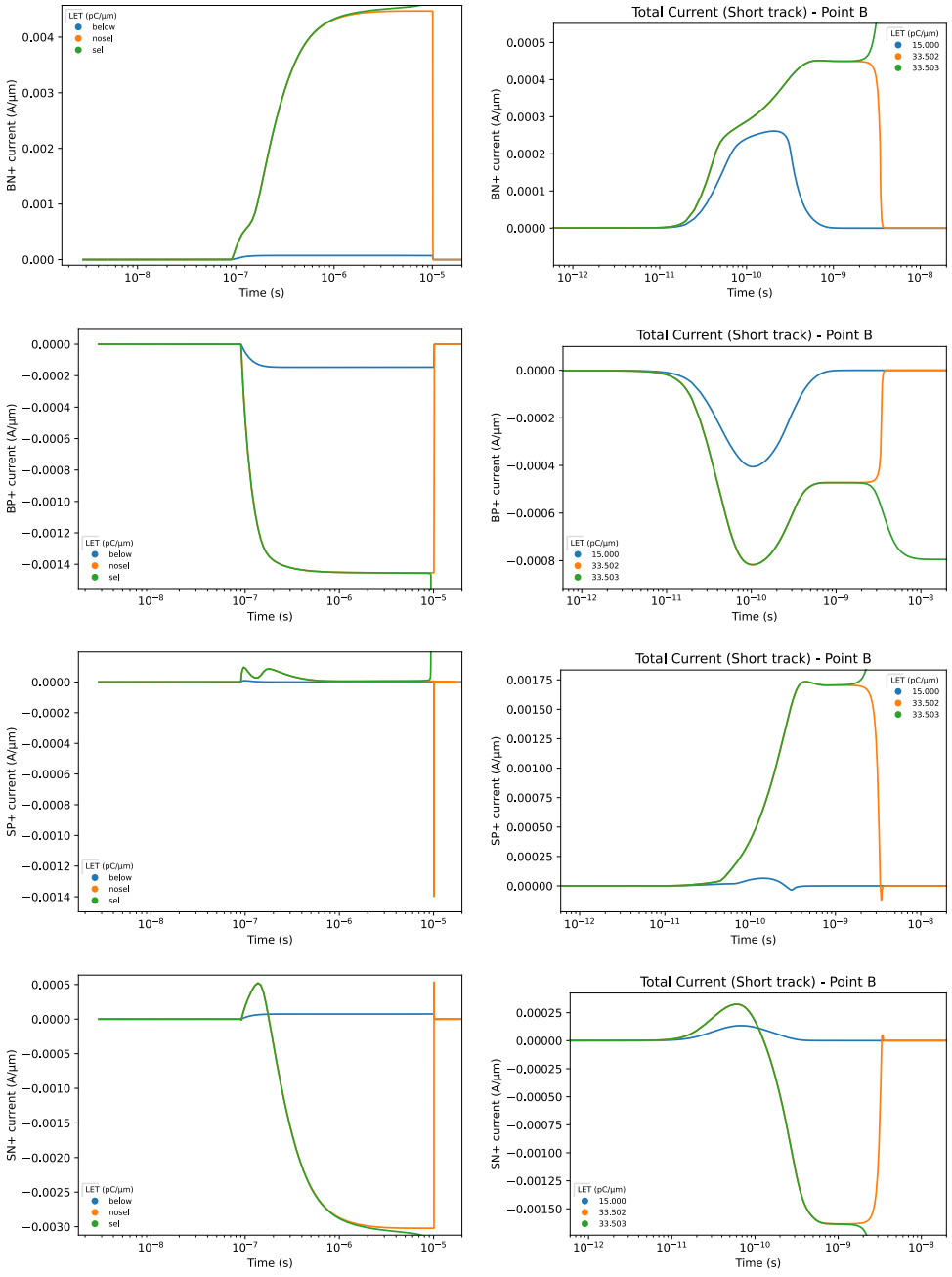

Figure 5.34 Current at the four terminal (BP+ and Sub are sum) for SPICE simulations (left) and Sentaurus short track configuration simulations (right)

where:

- N_0 is the number of the electron-hole pairs that have been created
- r is the distance to the point of generation
- t is the time
- D is the ambipolar diffusion constant
- τ is the recombination time costant

To this density, a current is associated, which is expressed by:

$$\boldsymbol{j} = eD\boldsymbol{\nabla}\mathrm{n} = -\mathrm{e}\frac{r}{2t}n(r,t) \qquad \text{Eq. 5.2}$$

And then, the current will be:

$$I = \iint_{depletion\ layer\ surface} \boldsymbol{j}d\boldsymbol{S} = e\frac{r}{2t}n(r,t)|\boldsymbol{u}.\boldsymbol{S}| \qquad \text{Eq. 5.3}$$

Using this formula, a different kind of pulse current would be obtained, like the one in Figure 5.35.

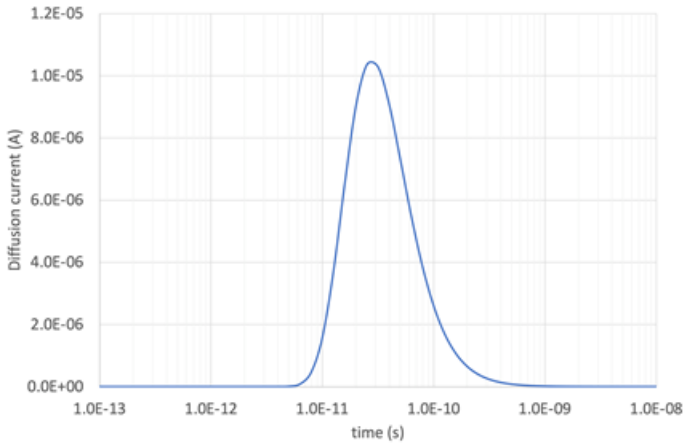

Figure 5.35 Typical pulse current obtained with the diffusion model. Here N0=62500 pairs, r=1μm, the depletion area is 1μm^2, D=36 cm^2/s and recombination were assumed to be negligible.

In addition, more information on the features of the both bipolar transistors, would be important to evaluate the incidence of a given pulse on the parasitic circuit. For instance, the values of R_{well} and $R_{substrate}$ resistance, would be crucial to have a better prediction. However, the investigation of

the effects of these improvements given here are out of the scope of this work.

5.2 Prediction of SEL using TCAD simulations

In the previous section we have analyzed the dynamic behavior of Single Event Latchup and we have discussed how to use it for prediction of it. On the other hand, in this section we are going to analyze how could be possible to predict SEL considering only the charge collected and deposited in the device, discarding the dynamic and the time dependence of SEL. The idea is that, as electron-hole pairs are created inside the device, they will diffuse by ambipolar diffusion, due to the low electric field inside the device, and it will be collected in a region where the electric field is more relevant, as the junction between n-well and p-substrate. Then, the goal is to find a correlation between the deposited charge and the occurrence of SEL.

5.2.1 Methodology

Simulation have been performed with the structure discussed in section 4.1.1. Using the short track method, we have injected several ions in the device. In Figure 5.36, we recap the entirety of the points (that we call, deposition points).

Table 5.2 Coordinates of deposition points for the under n-well group

Y (μm)	X (μm)								
0.455									
0.81									
1.06	0.30	0.40	0.50	0.59	0.69	0.79	0.88	1.11	1.31
1.56									
1.81									

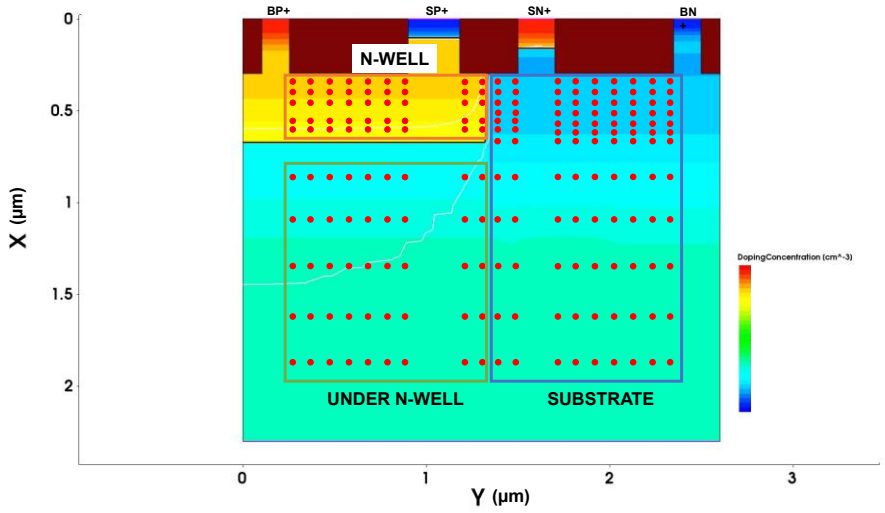

Figure 5.36 Set of deposition points used in the TCAD simulations. We have divided the points in three groups: substrate, n-well and under n-well

Table 5.3 Coordinates of deposition points for the substrate group.

Y (µm)	X (µm)									
0.31	1.35	1.40	1.74	1.81	1.84	1.94	2.03	2.13	2.23	2.32
0.35										
0.41										
0.455										
0.56										
0.81										
1.06										
1.31										
1.56										

Table 5.4 Coordinates of deposition points for the n-well group.

Y (µm)	X (µm)								
0.31	0.30	0.40	0.50	0.59	0.69	0.79	0.88	1.11	1.31
0.35									
0.41									
0.51									

Meanwhile, in Table 5.3, Table 5.4, Table 5.2 we show the coordinates of each points. Every dot represents a simulation. For each simulation, the threshold LET has been found. Then, we need to define the point in which the charge collected is responsible of triggering SEL. As we mentioned, we have considered an area close to the n-well/p-substrate junction, where the electric field is higher (Figure 5.37). Then, we have taken three collection points: point C_1, placed in the substrate which is used when the ion impacts in the substrate; point C_2, placed in the n-well, utilized when we consider an impact in the n-well; point C_3, placed in the substrate, that is used when the track is placed under the n-well. In Table 5.5, the three points coordinates are written.

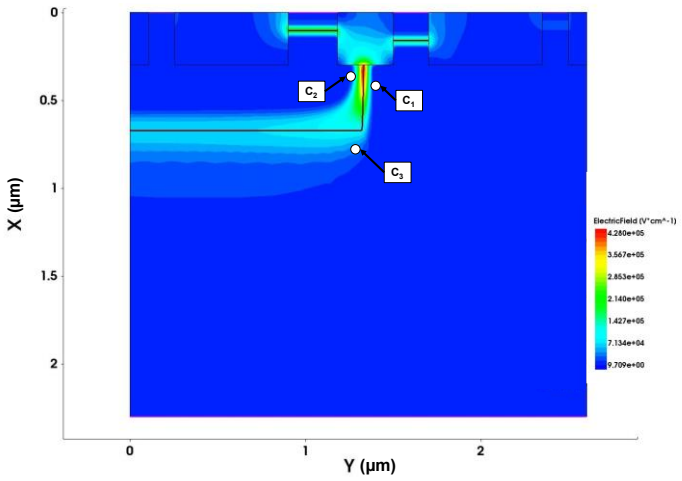

Figure 5.37 Electric field color maps from Sentaurus. The collection point C_1,C_2,C_3 are shown.

In addition, we are interested in two values: the threshold deposited charge Q_{th}, which is the minimum deposited charge in the deposition points, that will trigger SEL; and the critical charge Q_{crit}, which is the minimum charge collected in the collection points.

Table 5.5 Coordinates of the collection points.

	X (μm)	**Y** (μm)
Point C_1	0.45525	1.35
Point C_2	0.44	1.13
Point C_3	0.70	1.30

5.2.2 Results and analysis

Our simulations allow us to calculate just Q_{th}, so we need to link Q_{th} to Q_{crit}. Normally, in 2D simulations, the collected charge is proportional to the deposited charge divided by the distance between these two points.

$$Q_{coll} = \lambda \frac{Q_{dep}}{r} \qquad \text{Eq. 5.4}$$

where λ expresses a length on which the collection occurs and r is the distance between the deposition point and the collection point. Consequently, at the threshold, Eq. 5.4 becomes:

$$Q_{crit} = \lambda \frac{Q_{th}}{r} \qquad \text{Eq. 5.5}$$

or:

$$Q_{th} = \frac{Q_{crit}}{\lambda} r \qquad \text{Eq. 5.6}$$

Now, we will show the results divided in three groups, depending on the position of the ion injection (Figure 5.38, Figure 5.39, Figure 5.40). Each figure shows the threshold charge for each single deposition points in the substrate, n-well and under n-well respectively. In each figure is reported

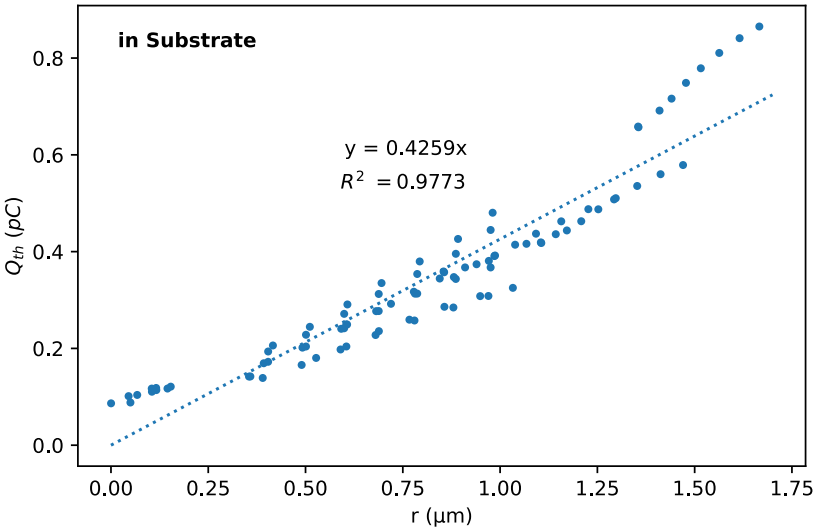

Figure 5.38 Threshold charge versus r (distance of the deposition point from the collection point C_1) for the substrate group. The dotted line represents the linear trendline. The equation and the R^2 value are annotated in the chart.

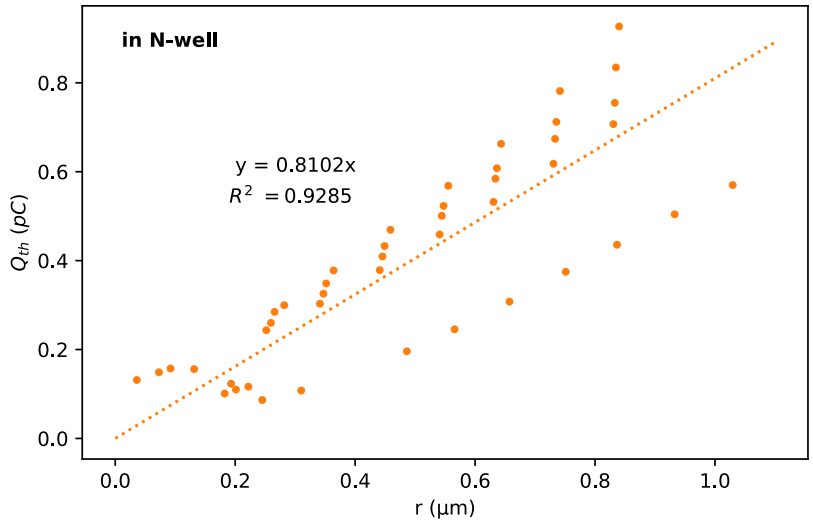

Figure 5.39 Threshold charge versus r (distance of the deposition point from the collection point C_2) for the n-well group. The dotted line represents the linear trendline. The equation and the R^2 value are annotated in the chart.

the linear trendline equation and the R^2 value. We can see that we obtained a proportionality law between the threshold charge and the distance as in Eq. 5.6. However, there is a discrepancy between the theoretical linear law

and the simulations, probably because the electric field is not totally negligible, neither recombination and also because the collection does not occur at a single point as assumed for sake of simplicity.

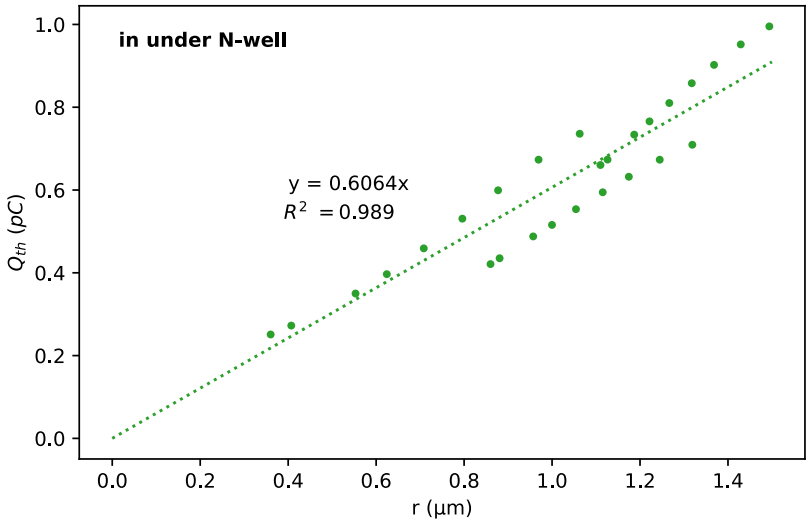

Figure 5.40 Threshold charge versus r (distance of the deposition point from the collection point C_3) for the under n-well group. The dotted line represents the linear trendline. The equation and the R^2 value are annotated in the chart.

To understand this discrepancy, first we need to focus our attention on only one group, in this case we use the substrate group. As we mentioned, collection can be influenced by different parameters. So, once we have calculated the trendline for one group, we can calculate the efficiency η of collection for each single point, with respect to the trendline, obtaining for the substrate group:

$$\eta_{sub} = \frac{0.4259\, r}{Q_{th}} \qquad \text{Eq. 5.7}$$

If we plot the efficiency versus the x position (which in our case is opposite with respect the usual convention on x and y axes, see Figure 5.36), we can see that for X higher than 0.81, the efficiency is dependent mainly on X (Figure 5.41). Meanwhile, for X lower than 0.81, there is no clear

dependency. This could be due to the fact that for X lower than 0.81, points are closer to the collection point and then other effects should be taken into account. Another proof of this is in Figure 5.42. In this figure, we have plotted the efficiency versus the distance from the collection point. Then, each point is colored depending on his X position. We can see that except for deposition points close to the collection point (distance lower than 0.2 um), the efficiency will depend only mainly on the X position, and it is ranged between 0.82 and 1.35.

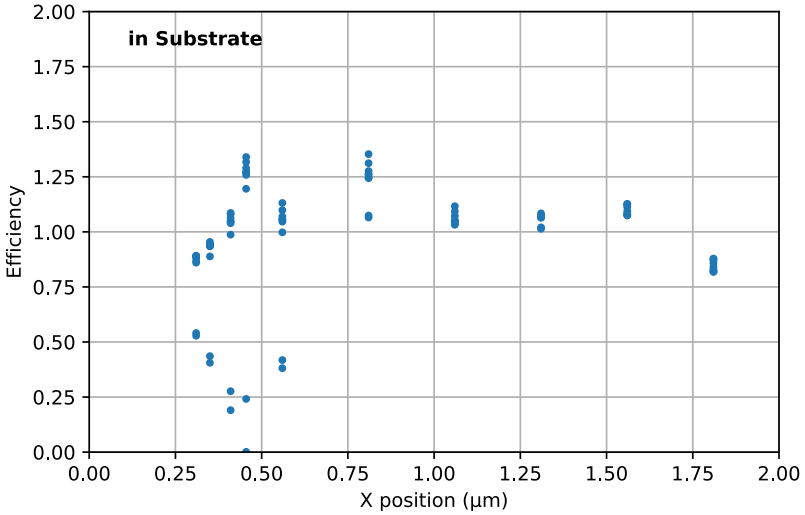

Figure 5.41 Efficiency factor versus X position for the substrate group.

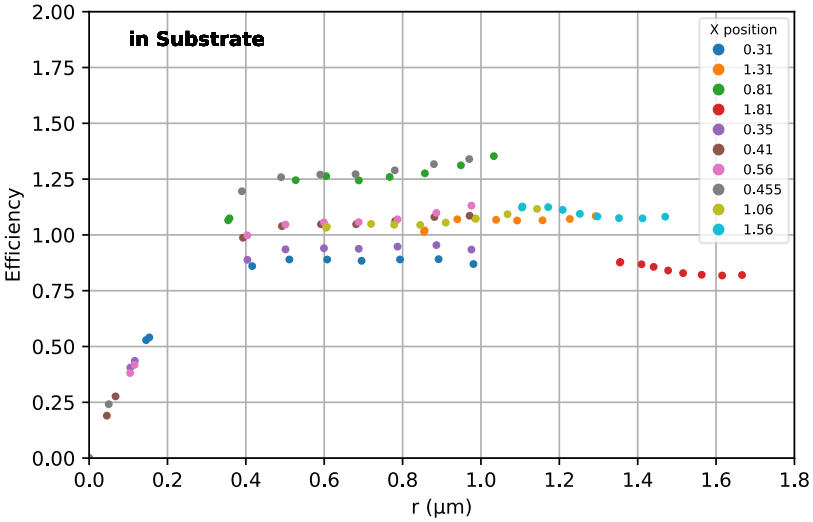

Figure 5.42 Efficiency factor versus r for the substrate group. The colours represents points from the same X position.

Now, we can see this behavior also for the other two groups. First, we start with the under n-well group. In Figure 5.43, we plot the efficiency versus the X position. In this case, the X dependency is clear because we have no deposition point close to the collection points, so the efficiency depends mainly on X. We can see that also in Figure 5.44 , where the efficiency versus the distance (r) is plot. In this case, the efficiency is ranging between 0.855 and 1.20.

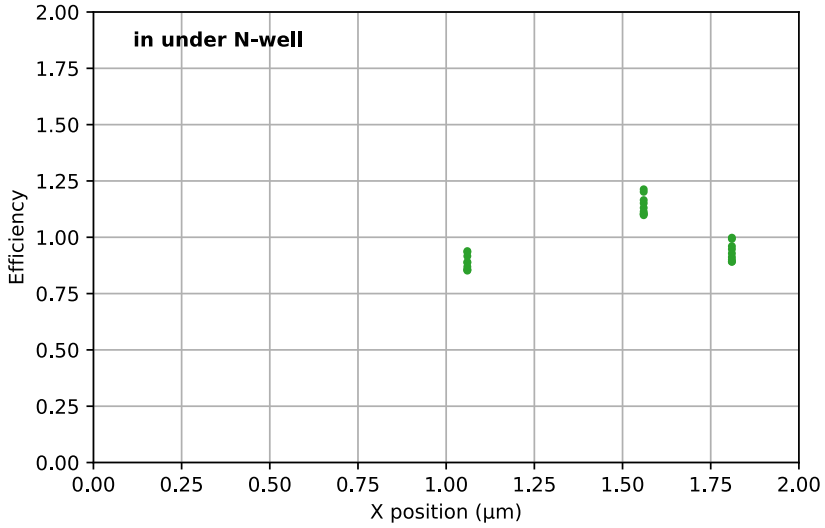

Figure 5.43 Efficiency factor versus X position for the under n-well group.

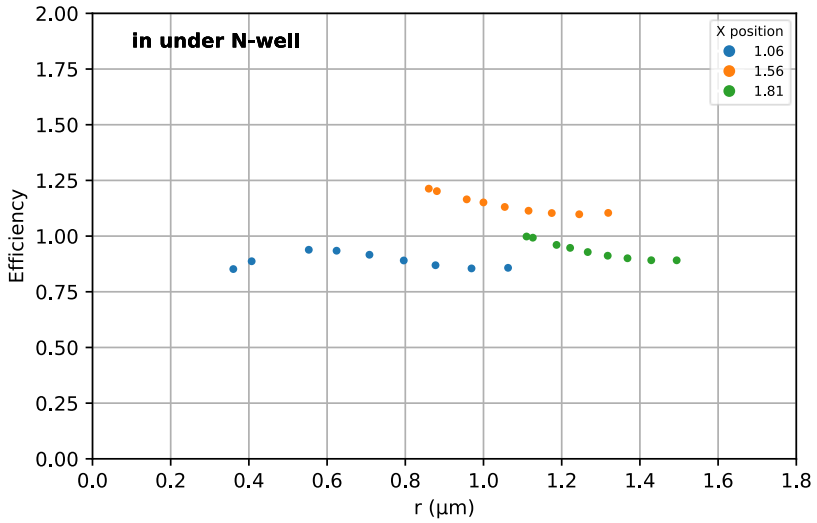

Figure 5.44 Efficiency factor versus r for the under n-well group. The colours represents points from the same X position.

Then, we move on to the n-well group. In this case, deposition points cannot be very far from the collection points, due to the dimension of the n-well. So, when we plot the efficiency versus the X position, the efficiency ranges from 0.260 to 1.809. However, when we plot the efficiency versus the distance from the collection point, we can see that the behavior is the same as the other groups. Below 0.2 µm, the dependence on X is not visible, meanwhile as we place further from the collection point, the dependency becomes more clear, and the efficiency ranges from 0.755 to 1.125.

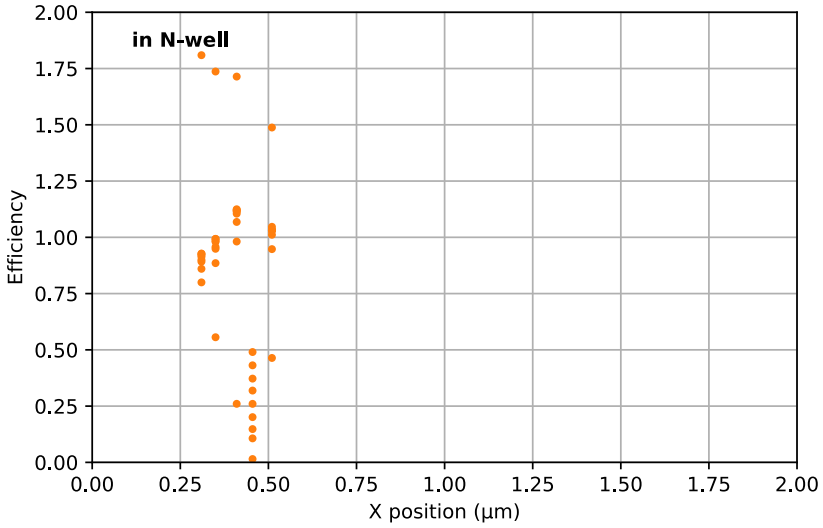

Figure 5.45 Efficiency factor versus X position for the n-well group.

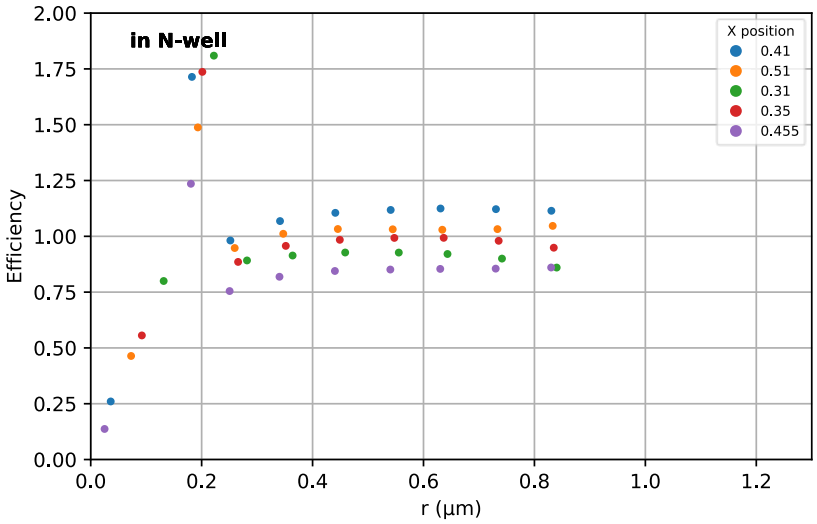

Figure 5.46 Efficiency factor versus r for the n-well group. The colours represents points from the same X position

In conclusion, we have seen that it is possible to correlate the deposited charge in a specific deposition point, with the distance from the collection point. Nonetheless, we have found that some efficiency factor must be used in order to obtain a more accurate relation between the two values. In any case, with this method, knowing the deposition point, we can be able to predict the charge needed for the triggering of SEL in most of the cases, especially if the deposition point is far from the junction. This information can be used as the foundation of a fast predictive tool. In fact, instead of using complex TCAD simulations that requires too much CPU time, we can consider that the device is characterized by just 2 parameters, Q_{crit} and λ. With these parameters we should be able to predict SEL cross-sections. However, some improvements is necessary. For instance, more simulation could be ran in order to investigate what happen for low values of distance r. In addition, different collection points could be tested. In fact, we have to consider that these collection points have been chosen arbitrarily, but their choice could be improved if more simulations are available. Once these improvements are done, simulations could be extended to the long track and to 3D simulations.

5.3 Conclusions

In this chapter, we have investigated two methodologies to predict Single Event Latchup. These methodologies starts from two different ideas. In the first method, we used TCAD simulations to study the dynamic of SEL and then we used SPICE simulations. So, in this method we highly rely on the time evolution of SEL. Meanwhile, in the second method we do not take into consideration the time evolution of SEL, but instead we try to correlate the charge deposited in the device and the occurrence of SEL.

With the first method we have performed TCAD simulations, using what we called short track. We injected the short track in the n-well and in the p-substrate and we have analyzed the current at the five terminals of the device. By analyzing the currents, we have highlighted six steps that leads to Single Event Latchup. Then, we have compared these results with another

TCAD tool, ECORCE. The comparison showed that the same steps were found in ECORCE, although some difference in timing and current magnitude was found, probably due to the different physical models that were used. In addition, we have compared the short track simulations with the long track simulations. Even in this case, we have found the same steps for SEL. Eventually, we used this knowledge to implement a SPICE simulation. According to the behavior found in TCAD simulations, we have created a circuit model for SEL. This model follows the steps that we have found in the TCAD simulations. Further steps would be to tune the SPICE parameters with the characteristics of the actual parasitic transistor that we simulate in TCAD.

Also with the second method we have used TCAD simulations. At first, we have selected several deposition points where to inject the ion. Then, depending on the position of the deposition points, we have defined three collection points. By calculating the distance between the deposition points and the collection points, we could relate the charge deposited in the deposition point to the distance with the collection points. We have seen that there is a linear correlation between these two values, even though some discrepancies are present. These discrepancies are due to the different X position of the deposition points. In fact, we have calculated an efficiency factor to match the calculated threshold charge and the trendline. Then, we have seen that the efficiency factor, except that for low distance, is dependent mainly on the X position of the deposition point.

General conclusions

Electronic components are crucial in our modern era. Whether on ground or on space applications, the role of electronic devices can be crucial. As a consequence, their reliability is a key factor for their exploitation. Certainly, it is important to predict the behavior of a particular component. Nonetheless, the requirements they may met will be different depending on their application and on the environment in which they will work. Space, high-energy physics accelerators, nuclear power plants, they all have a different radiation environment, and depending on that, different outcomes will occur. In fact, radiation effects on electronic components are typically divided in three categories: Total Ionizing Dose, Single Event Effects and Displacement Damage. In this work, we have focused on Single Event Effects and specifically Single Event Latchup. The goal of this work is to investigate the effects of specifics design parameters on SEL sensitivity and to identify a method to predict SEL

In the first chapter, we have analyzed the different radiation environments, from ground to space. Ground applications may vary from high-energy physics accelerators or nuclear power plants. Each environment will pose a different challenge. For instance, in high-energy accelerators, a mixed field of particles with high energy up to 500 GeV are present, meanwhile in nuclear power plants, mostly neutron and gamma are present. In space, different radiation sources are present. Some are coming from the outer galaxies, as Galactic cosmic rays. They are composed by all the elements of the periodic table and due their composition and energies they can represent a significant risk to long duration spaceflight outside atmosphere. Another source of radiation is the Sun. It emits two different kind of radiation: a constant and low energy flux, which is less concerning for electronic components and sudden and high energy burst of particles, which can create damage to the electronic devices. Eventually, these particles will finally end up in two ways. First, in the Van Allen belts, which are belts containing particles trapped by the Earth's magnetic field and

second, some of the particles will interact with Earth's atmosphere and will create a cascade of secondary particles, which can create some damage to ground or to aviation application.

In the second chapter, we have discussed about Single Event Effects and specifically about Single Event Latchup. Single Event Effects are the consequences of a single particle hitting a component and creating electron-hole pairs inside it. Then, depending on the characteristics of the devices itself, different effects may appear. One of these is Single Event Latchup, which is the topic of this work. It arises from parasitic transistors, which are inherent to CMOS devices. If this effects is triggered, it may lead to the destruction of the device. We have analyzed which are the parameters that affects its sensitivity. Then, we had a deeper look to some of them, which will be investigated throughout this manuscript: temperature, doping profiles, anode to cathode spacing and well and substrate taps placement.

In the third chapter, we have introduced the tools used in this work. Single Event Latchup has been investigated by using computer simulations. Two different categories of tools have been used: TCAD and SPICE tools. TCAD stands for Technology computer-aided design and it is used to model semiconductors structure and physics. Different software exist, some developed by companies and some by universities or agencies. In this work we have used two specific software: Sentaurus and ECORCE. Sentaurus is developed by the company Synopsys, meanwhile ECORCE is developed by the University of Montpellier. The other class is SPICE tools, which were developed in the 1970s at the Electronics Research Laboratory of the University of California, Berkeley. It is a software that simulates the electrical performance of electronic circuits.

In the fourth chapter, we have started to analyze the effects of three parameters on SEL sensitivity. The parameters are: doping profiles, anode to cathode spacing, well and substrate taps placement. These parameters were modified within a certain range to investigate the effects of their variation. We have performed 2D TCAD simulations of a NPNP structure based on 65nm CMOS inverter. From these simulations, we have calculated

the SEL cross section and the SEL rate for each parameter. The SEL rate has been calculated using OMERE, a tool dedicated to the analysis of the space environment and radiation effects on electronics developed by TRAD and CNES. In this way, we have compared the effects of each parameter on SEL sensitivity. We have observed that doping profiles and well and substrate taps placement variation have a stronger impact on SEL sensitivity compared to A-C spacing. This result is highly important in design phase to decide which strategies can be adopted to harden the component. Then, we have investigated the effects of temperature variation in combination with the variation of each of the previous parameters. In this case, we have focused our attention on threshold LET and SEL rate. At first, threshold LET is investigated. We have observed, for every case, that when the component is less sensitive to SEL, temperature has a stronger impact on threshold LET, with respect to the opposite case. To further investigate this trend, we have calculated SEL rate for the GEO and LEO orbits. Indeed, the same trend has been observed for SEL rate. It is important to take into consideration this aspect when a device is facing different temperature conditions.

Eventually, in the fifth chapter, we have analyzed two methodologies to predict Single Event Latchup. The first method envisaged the combination of the simulation tools, TCAD and SPICE. With the first tool, we have investigated the dynamic of SEL. This has been done for three different values of LET, which are representative of three different situations for the device: the LET value at which SEL occurs (or the threshold); the LET value right before the threshold, given by the accuracy of the simulations (0.001 $pC/\mu m$); and an LET value well below the threshold. By using what we called a short ion track, we have injected charges in the n-well and the p-substrate. Currents at the different terminals of the device have been captured, and six steps have been retrieved. These steps are the one that leads to SEL. To find more proof of these steps, we have performed similar simulations with another TCAD tool, ECORCE, and with a long track. In both cases, the same steps were found, although some difference has been found due to the different nature of the simulations. Eventually, using the knowledge acquired with TCAD simulations, we have designed a modeling circuit in

SPICE, able to mimic the same steps. What we have found, is that this model is coherent with the TCAD simulations and then, it can be used for SEL prediction. Further steps would be to tune the SPICE parameters with the characteristics of the actual parasitic transistor that we simulate in TCAD.

On the other hand, the second method relies exclusively on TCAD simulations. The goal of this method is to correlate charge deposition to SEL occurrence. To do so, we have performed simulations with the short ion track in different deposition points. Depending on the location of the deposition points, we have defined three collection points. Due to the fact that was not possible to calculate the collected charge in a specific point, we wanted to link the deposited charge with the distance of the deposition points to the related collection point. The result was that there is a linear correlation between these two values, even though some discrepancies are present. Furthermore, we have seen that these discrepancies are due to the X position of the deposition points. Then, to overcome this problem, we have calculated an efficiency factor in order to match the calculated threshold charge and the trendline. Thanks to this efficiency factor, we have seen that, as far as the deposition point has a distance greater than 0.2 μm from the collection point, the efficiency factor is between ~0.85 and ~1.25, then introducing an error not greater than 25%. Thus, it is possible to correlate linearly the deposited charge with the distance from the related collection point.

Therefore, we can summarize the contribution and the future prospects of this work into four major outcomes:

- We have further investigated the influence of design parameters on SEL sensitivity. Our results confirmed the previous literature and they have extended the investigation not only to the threshold LET, but also to the SEL cross sections. We have developed a methodology that allows us to perform 2D simulations and to still obtain helpful parameters as the SEL cross section. In addition, we have observed that the impact of the parameter variation is different for each parameter and that it has to be taken into account, during the design

phase or during the development of a simulation where the design parameter are not known in detail.

- The impact of temperature variation in correlation with design parameters has been investigated. The results showed that the temperature impact is not constant for every temperature. This information is important when a device will face different temperature conditions and then its response can be different from the one expected at another temperature.
- A new SPICE model circuit has been proposed for SEL prediction. This model arises from the study of the time evolution of SEL in PNPN structure. We have identified six steps that has been used to mimic the SEL obtained with TCAD simulations, in SPICE. Nonetheless, this model can be improved in the future with more detailed parameters about the actual parasitic bipolar transistor that we simulate on TCAD.
- Eventually, another prediction model has been proposed. This method relies on a linear correlation between the deposited charge and the SEL occurrence. This allows to know rapidly the sensitivity of a device to SEL, with no need to perform numerous simulations. Even in this case, some improvements can be made. More simulations in different configurations could be helpful to obtain a more accurate linear correlation in the first place.

List of publications

S. Guagliardo et al., “Single-Event Latchup sensitivity: Temperature effects and the role of the collected charge”, *Microelectronics Reliability*, Volume 119, 2021, 114087, ISSN 0026-2714, https://doi.org/10.1016/j.microrel.2021.114087.

S. Guagliardo et al., Single Event Latchup Cross Section Calculation from TCAD Simulations—Effects of the Doping Profiles and Anode to Cathode Spacing, *European Conference on Radiation and its effects on Component and Systems (RADECS 2019),* Montpellier, France, 2019, *to be published*.

S. Guagliardo et al., "Effect of Temperature on Single Event Latchup Sensitivity," *2020 15th Design & Technology of Integrated Systems in Nanoscale Era (DTIS)*, Marrakech, Morocco, 2020, pp. 1-5.

Appendix

In this appendix, we show the complete charts for the different points showed in Figure 5.2.

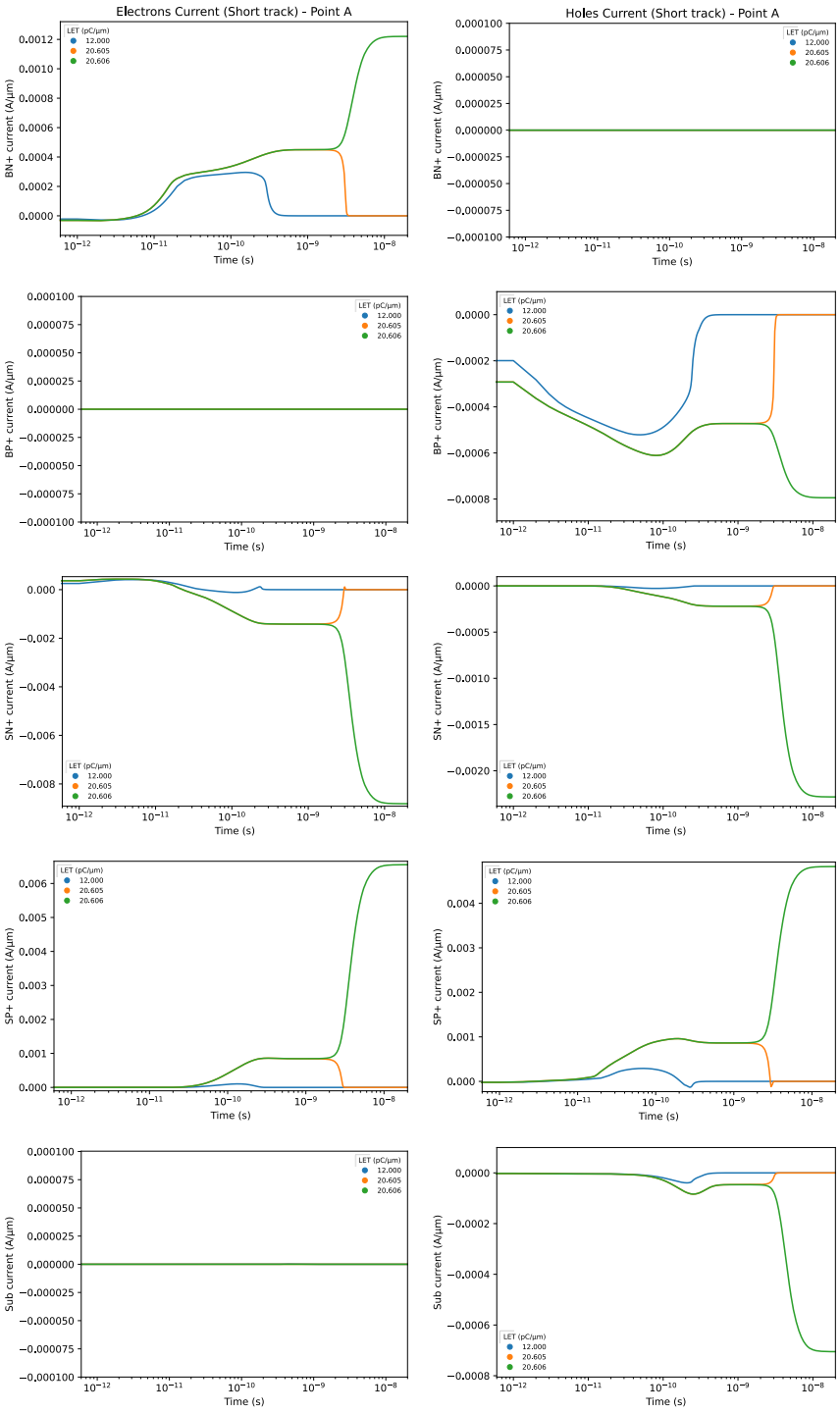

Figure A.1 Complete current charts for point A.

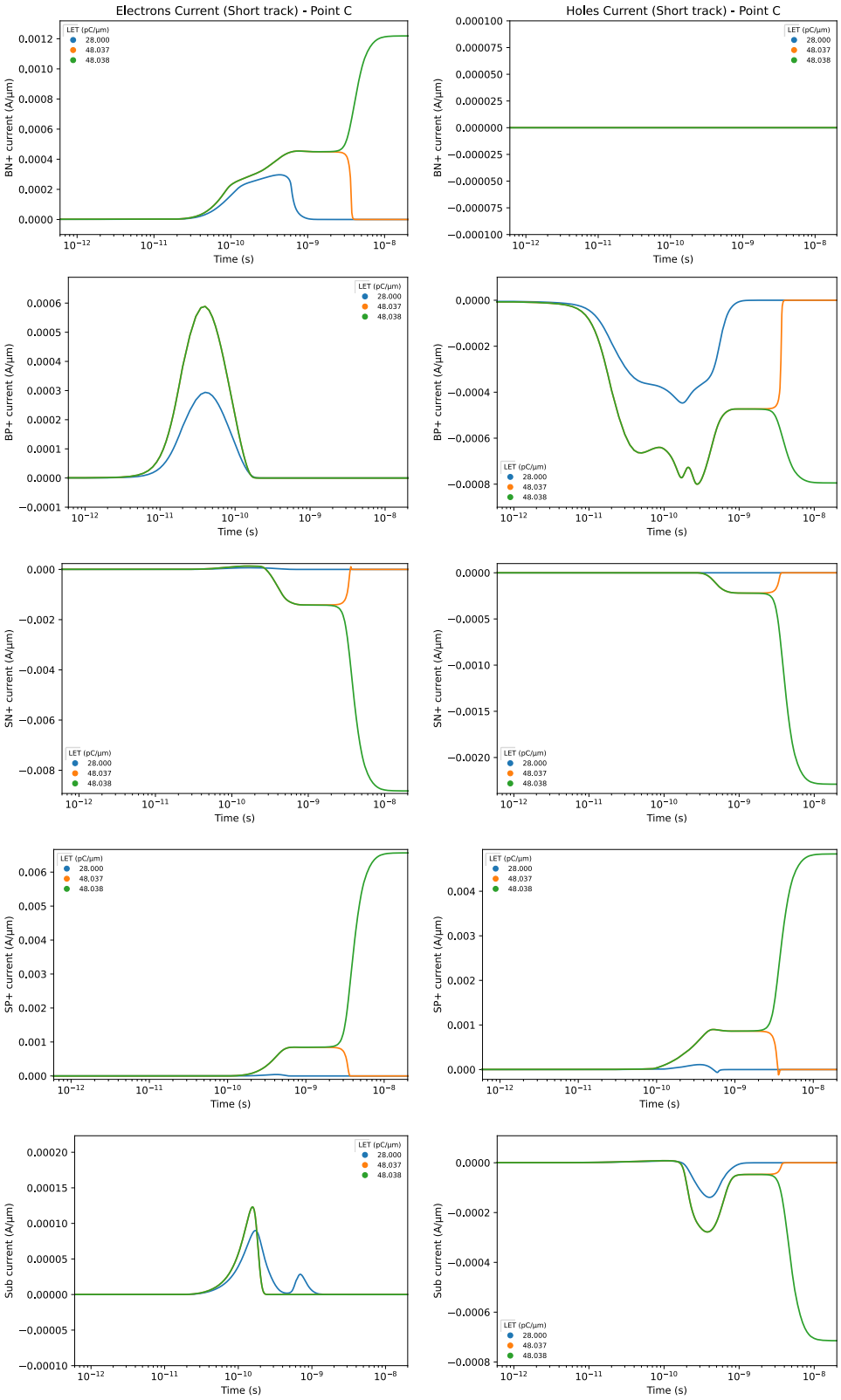

Figure A.2 Complete current charts for point C.

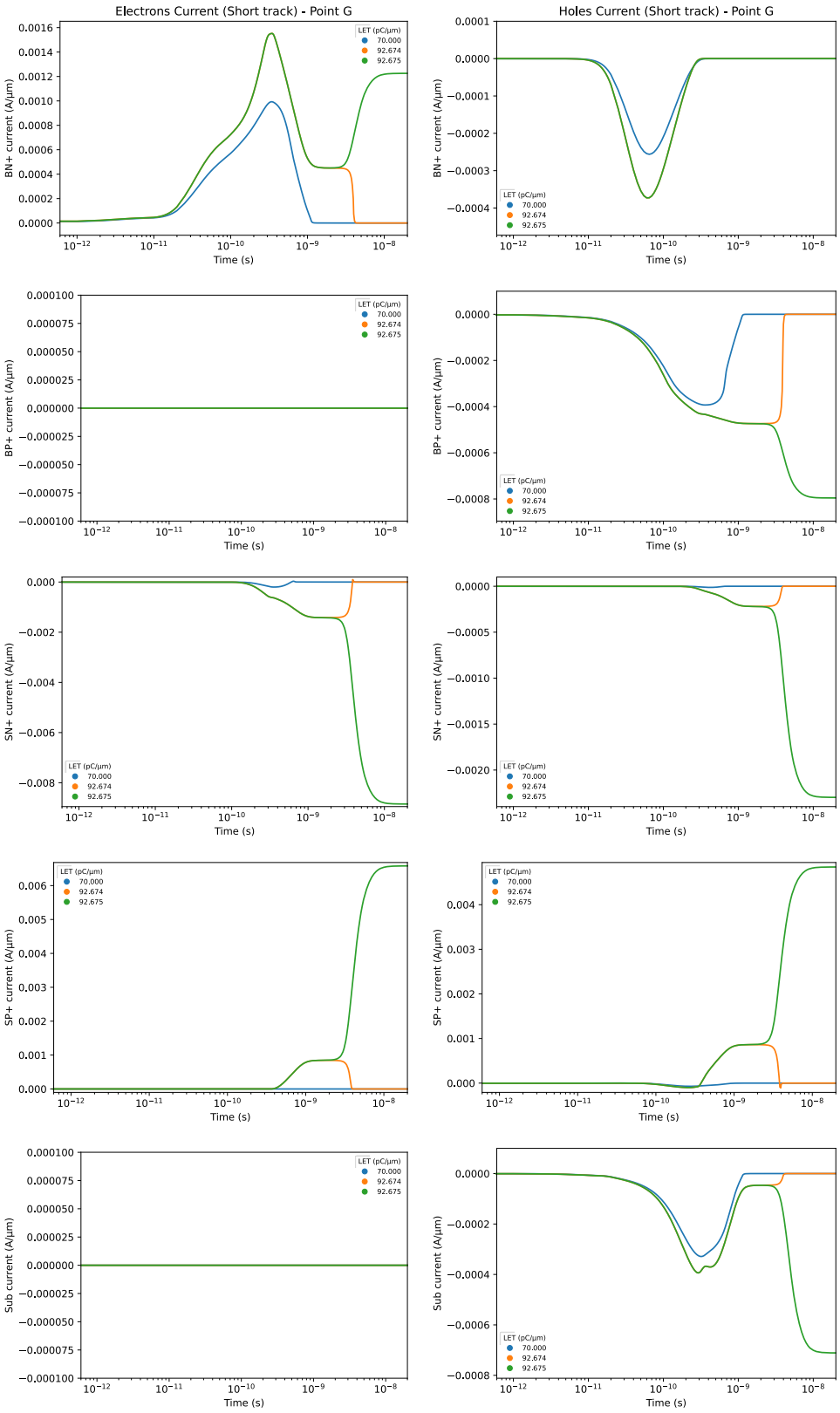

Figure A.3 Complete current charts for point G.

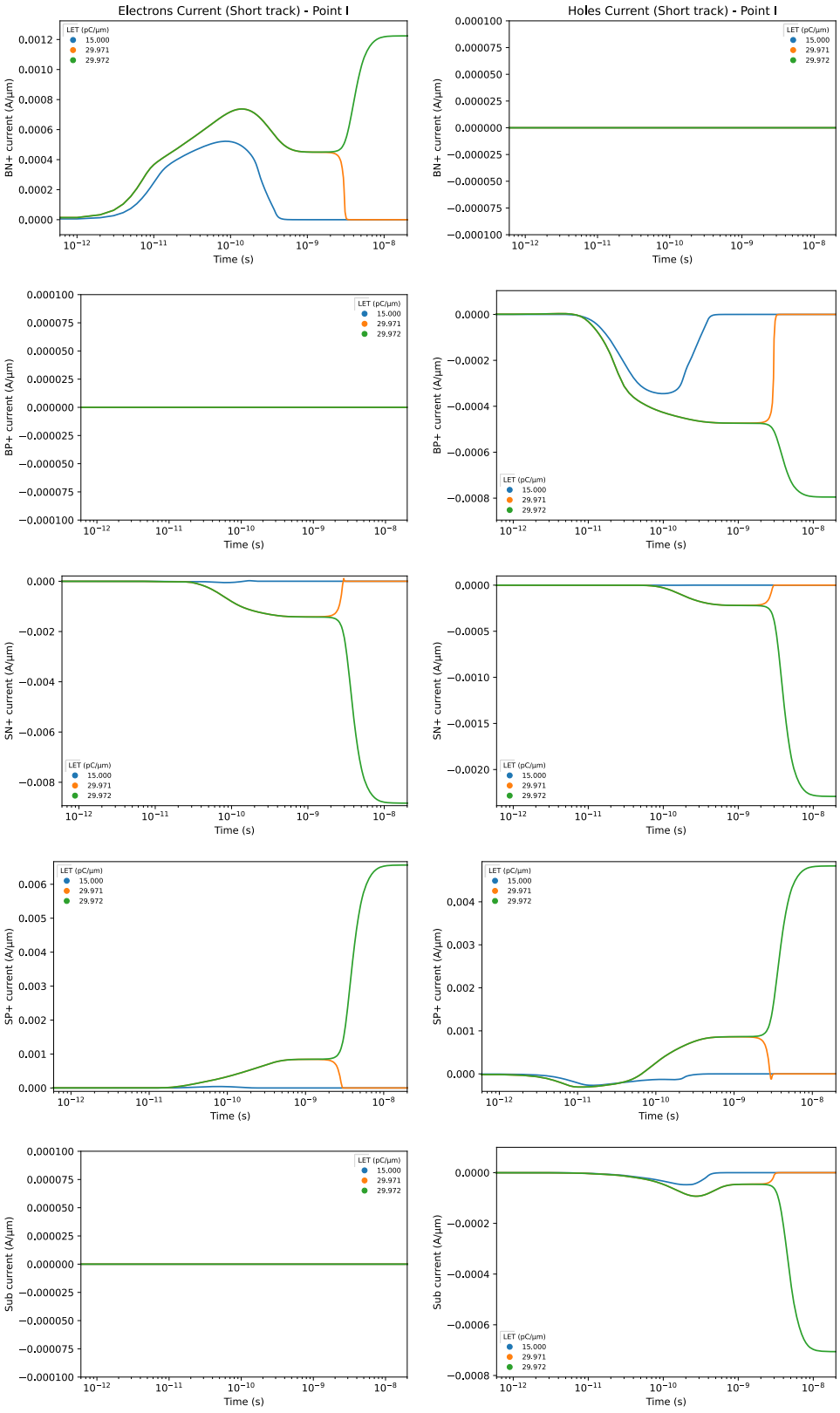

Figure A.4 Complete current charts for point I.

References

[1] J. W. Wilson, A. Cucinotta, H. Tai, L. C. Simonsen, M. Y. Kim, and A. Thibeault, "Galactic and Solar Cosmic Ray Shielding in Deep Space," p. 22.

[2] J. L. Barth, C. S. Dyer, and E. G. Stassinopoulos, "Space, atmospheric, and terrestrial radiation environments," *IEEE Trans. Nucl. Sci.*, vol. 50, no. 3, pp. 466–482, Jun. 2003, doi: 10.1109/TNS.2003.813131.

[3] J. D. Wrbanek and S. Y. Wrbanek, "Space Radiation and Impact on Instrumentation Technologies," p. 34, 2020.

[4] V. L. Ginzburg, "Cosmic ray astrophysics (history and general review)," *Phys.-Uspekhi*, vol. 39, no. 2, p. 155, 1996.

[5] J. W. Cronin, "Cosmic rays: the most energetic particles in the universe," *Cosm. Rays*, vol. 71, no. 2, p. 8, 1999.

[6] R. A. Mewaldt, "Galactic cosmic ray composition and energy spectra," *Adv. Space Res.*, vol. 14, no. 10, pp. 737–747, Oct. 1994, doi: 10.1016/0273-1177(94)90536-3.

[7] K. Lodders, "Solar System Abundances and Condensation Temperatures of the Elements," *Astrophys. J.*, vol. 591, no. 2, pp. 1220–1247, Jul. 2003, doi: 10.1086/375492.

[8] National Research Council (U.S.) and Ad Hoc Committee on the Solar System Radiation Environment and NASA's Vision for Space Exploration, *Space radiation hazards and the Vision for Space Exploration: report of a workshop*. Washington, D.C.: National Academies Press, 2006. Accessed: Nov. 04, 2020. [Online]. Available: http://site.ebrary.com/id/10150102

[9] M. Durante and F. A. Cucinotta, "Physical basis of radiation protection in space travel," *Rev. Mod. Phys.*, vol. 83, no. 4, pp. 1245–1281, Nov. 2011, doi: 10.1103/RevModPhys.83.1245.

[10] L. W. Townsend, "Implications of the space radiation environment for human exploration in deep space," *Radiat. Prot. Dosimetry*, vol. 115, no. 1–4, pp. 44–50, Dec. 2005, doi: 10.1093/rpd/nci141.

[11] G. Santin, P. Truscott, R. Gaillard, and R. Garcia Alia, "Radiation environments: space, avionics, ground and below," *RADECS 2017 Short Course*, p. 142, 2017.

[12] T. G. Forbes, "A review on the genesis of coronal mass ejections," *J. Geophys. Res. Space Phys.*, vol. 105, no. A10, pp. 23153–23165, Oct. 2000, doi: 10.1029/2000JA000005.

[13] B. C. Low, "Solar activity and the corona," *Sol. Phys.*, vol. 167, pp. 217–265, 1996, doi: 10.1007/BF00146338.

[14] S. W. Kahler, “Solar Flares and Coronal Mass Ejections,” p. 30.

[15] D. P. Stern, “A brief history of magnetospheric physics before the spaceflight era,” *Rev. Geophys.*, vol. 27, no. 1, p. 103, 1989, doi: 10.1029/RG027i001p00103.

[16] N. C. Christofilos, “The Argus experiment,” *J. Geophys. Res.*, vol. 64, no. 8, pp. 869–875, Aug. 1959, doi: 10.1029/JZ064i008p00869.

[17] A. M. Lenchek and S. F. Singer, “Geomagnetically trapped protons from cosmic-ray albedo neutrons,” *J. Geophys. Res.*, vol. 67, no. 4, pp. 1263–1287, Apr. 1962, doi: 10.1029/JZ067i004p01263.

[18] W. Li and M. K. Hudson, “Earth’s Van Allen Radiation Belts: From Discovery to the Van Allen Probes Era,” *J. Geophys. Res. Space Phys.*, vol. 124, no. 11, pp. 8319–8351, Nov. 2019, doi: 10.1029/2018JA025940.

[19] S. Snowden, “Steve Snowden (US ROSAT Science Data Center) - http://heasarc.gsfc.nasa.gov/docs/rosat/gallery/display/saa.html,” *US ROSAT Science Data Center*. http://heasarc.gsfc.nasa.gov/docs/rosat/gallery/display/saa.html

[20] J. Mazur, “The radiation environment outside and inside a spacecraft,” *2002 IEEE NSREC Short Course*, p. 317, 2002.

[21] M. K. Hudson *et al.*, “Simulations of radiation belt formation during storm sudden commencements,” *J. Geophys. Res. Space Phys.*, vol. 102, no. A7, pp. 14087–14102, Jan. 1997, doi: 10.1029/97JA03995.

[22] B. T. Kress, “Impulsive solar energetic ion trapping in the magnetosphere during geomagnetic storms,” *Geophys. Res. Lett.*, vol. 32, no. 6, p. L06108, 2005, doi: 10.1029/2005GL022373.

[23] E. G. Stassinopoulos and J. P. Raymond, “The space radiation environment for electronics,” *Proc. IEEE*, vol. 76, no. 11, pp. 1423–1442, Nov. 1988, doi: 10.1109/5.90113.

[24] J. I. Vette, “The NASA/National Space Science Data Center,” p. 60.

[25] CERN. Geneva. The LHC Study Group, “Design study of the Large Hadron Collider (LHC): a multiparticle collider in the LEP tunnel,” 1991, doi: 10.5170/CERN-1991-003.

[26] F. Wrobel, “Fundamentals on Radiation-Matter Interaction,” *RADECS 2005 Short Course*, p. 34, 2005.

[27] O. Klein, “Uber die Streuung yon Strahlung durch freie Elektronen nach der neuen relativistischen Quantendynamik yon Dirac.,” *Z. Für Phys.*, vol. 52, pp. 853–868, 1929.

[28] D. Brusaa, G. Stutza, J. A. Riverosa, J. M. Fernbdez-Vareab, and F. Salvata, “Fast sampling algorithm for the simulation of photon Compton scattering,” p. 9.

[29] J. E. Turner, “Interaction of ionizing radiation with matter,” *Health Phys.*, vol. 88, no. 6, p. 25, 2005.

[30] J.-L. Autran, *Soft Errors: From Particles to Circuits*, 1st ed. CRC Press, 2015. doi: 10.1201/b18132.

[31] N. Bohr, "On the decrease of velocity of swiftly moving electrified particles in passing through matter," *Lond. Edinb. Dublin Philos. Mag. J. Sci.*, vol. 30, pp. 581–615, 1915.

[32] N. Bohr, "On the theory of the decrease of velocity of moving electrified particles on passing through matter," *Lond. Edinb. Dublin Philos. Mag. J. Sci.*, vol. 25, no. 145, pp. 10–31, Jan. 1913, doi: 10.1080/14786440108634305.

[33] J. F. Ziegler and J. P. Biersack, *The Stopping and Range of Ions in Matter*. Boston, MA: Springer.

[34] H. Bethe, "Zur Theorie des Durchgangs schneller Korpurkularstrahlen durch Materie," *Ann. Phys.*, vol. 397, pp. 325–400, 1930.

[35] J. Lindhard and M. Scharff, "Energy Dissipation by Ions in the kev Region," *Phys. Rev.*, vol. 124, no. 1, pp. 128–130, Oct. 1961, doi: 10.1103/PhysRev.124.128.

[36] R. A. Reed, "Fundamental Mechanisms for Single Particle-Induced Soft Errors," Tucson, AZ, 2008.

[37] Y. Zhang, W. J. Weber, and H. J. Whitlow, "Electronic stopping powers for heavy ions in silicon," *Nuclear Instruments and Methods in Physics Research Section B: Beam Interactions with Materials and Atoms*, vol. 215, no. 1–2, pp. 48–59, 2004.

[38] D. J. Skyrme, "The passage of charged particles through silicon," *Nuclear Instruments and Methods*, vol. 57, pp. 61–73, 1967.

[39] A. Virtanen, A. Javanainen, H. Kettunen, A. Pirojenko, I. Riihimäki, and K. Rantilla, "RADiation Effects Facility, JYFL." Available: jyu.fi/accelerator/radef

[40] M. Alderighi, F. Casini, S. Gerardin, A. Paccagnella, and M. Violante, "Long Duration Balloon ights for the evaluation of radiation e ects on electronic systems," p. 4.

[41] European Cooperation for Space Standardization, "ECSS-E-HB-10-12A Space Engineering: Calculation of Radiation and Its Effects and Margin Policy Handbook." ESA Requirements and Standards Division, 2010.

[42] G. Bruguier and J.-M. Palau, "Single particle-induced Latchup," *IEEE Trans. Nucl. Sci.*, vol. 43, no. 2, pp. 522–532, Apr. 1996, doi: 10.1109/23.490898.

[43] A. H. Johnston, "The influence of VLSI technology evolution on radiation-induced latchup in space systems," *IEEE Trans. Nucl. Sci.*, vol. 43, no. 2, pp. 505–521, Apr. 1996, doi: 10.1109/23.490897.

[44] J. F. Leavy and R. A. Poll, “Radiation-Induced Integrated Circuit Latchup,” *IEEE Trans. Nucl. Sci.*, vol. 16, no. 6, pp. 96–103, 1969, doi: 10.1109/TNS.1969.4325510.

[45] B. L. Gregory and B. D. Shafer, “Latch-Up in CMOS Integrated Circuits,” *IEEE Trans. Nucl. Sci.*, vol. 20, no. 6, pp. 293–299, 1973, doi: 10.1109/TNS.1973.4327410.

[46] R. R. Troutman, *Latchup in CMOS Technology*. Boston, MA: Springer US, 1986. doi: 10.1007/978-1-4757-1887-4.

[47] Ye Li, Xiaohan Gong, Weiwei Xu, Zhiliang Hong, and D. Killat, “An experimental extracted model for latchup analysis in CMOS process,” in *2009 IEEE 8th International Conference on ASIC*, Changsha, Hunan, China, Oct. 2009, pp. 1035–1038. doi: 10.1109/ASICON.2009.5351514.

[48] A. Al Youssef, L. Artola, S. Ducret, and G. Hubert, “Compact Modeling of Single-Event Latchup of Integrated CMOS Circuit,” *IEEE Trans. Nucl. Sci.*, vol. 66, no. 7, pp. 1510–1515, Jul. 2019, doi: 10.1109/TNS.2019.2920629.

[49] G. Goto, H. Takahashi, and T. Nakamura, “Modeling and analysis of transient latchup in double-well bulk CMOS,” *IEEE Trans. Electron Devices*, vol. 33, no. 9, pp. 1341–1347, Sep. 1986, doi: 10.1109/T-ED.1986.22668.

[50] T. Aoki, “Dynamics of heavy-ion-induced latchup in CMOS structures,” *IEEE Trans. Electron Devices*, vol. 35, no. 11, pp. 1885–1891, Nov. 1988, doi: 10.1109/16.7401.

[51] H. Iwata and T. Ohzone, “Numerical simulation of single event latchup in the temperature range of 77-450 K,” *IEEE Trans. Nucl. Sci.*, vol. 42, no. 3, pp. 148–154, Jun. 1995, doi: 10.1109/23.387354.

[52] J. M. Hutson *et al.*, “The Effects of Angle of Incidence and Temperature on Latchup in 65 nm Technology,” *IEEE Trans. Nucl. Sci.*, vol. 54, no. 6, pp. 2541–2546, Dec. 2007, doi: 10.1109/TNS.2007.910330.

[53] C. J. Marshall *et al.*, “Mechanisms and Temperature Dependence of Single Event Latchup Observed in a CMOS Readout Integrated Circuit From 16–300 K,” *IEEE Trans. Nucl. Sci.*, p. 5658023, Dec. 2010, doi: 10.1109/TNS.2010.2085018.

[54] J. G. Dooley and R. C. Jaeger, “Temperature dependence of latchup in CMOS circuits,” *IEEE Electron Device Lett.*, vol. 5, no. 2, pp. 41–43, Feb. 1984, doi: 10.1109/EDL.1984.25825.

[55] A. H. Johnston, B. W. Hughlock, M. P. Baze, and R. E. Plaag, “The effect of temperature on single-particle latchup,” *IEEE Trans. Nucl. Sci.*, vol. 38, no. 6, pp. 1435–1441, Dec. 1991, doi: 10.1109/23.124129.

[56] A. A. Youssef, L. Artola, S. Ducret, G. Hubert, and F. Perrier, “Investigation of Electrical Latchup and SEL Mechanisms at Low

Temperature for Applications down to 50K," *IEEE Trans. Nucl. Sci.*, pp. 1–1, 2017, doi: 10.1109/TNS.2017.2726684.

[57] J. M. Hutson, "Single Event Latchup in a deep submicron CMOS technology," Vanderbilt University, Nashville, TN, 2008.

[58] J. R. Schwank, V. Ferlet-Cavrois, M. R. Shaneyfelt, P. Paillet, and P. E. Dodd, "Radiation effects in SOI technologies," *IEEE Trans. Nucl. Sci.*, vol. 50, no. 3, pp. 522–538, Jun. 2003, doi: 10.1109/TNS.2003.812930.

[59] O. Musseau, "Single-Event Effects in SOI Technologies and Devices," *IEEE Trans. Nucl. Sci.*, vol. 43, pp. 603–613, Apr. 1996, doi: 10.1109/23.490904.

[60] N. A. Dodds *et al.*, "Effectiveness of SEL Hardening Strategies and the Latchup Domino Effect," *IEEE Trans. Nucl. Sci.*, vol. 59, no. 6, pp. 2642–2650, Dec. 2012, doi: 10.1109/TNS.2012.2224374.

[61] G. Gasiot, D. Giot, and P. Roche, "Multiple Cell Upsets as the Key Contribution to the Total SER of 65 nm CMOS SRAMs and Its Dependence on Well Engineering," *IEEE Trans. Nucl. Sci.*, vol. 54, no. 6, pp. 2468–2473, Dec. 2007, doi: 10.1109/TNS.2007.908147.

[62] H. Puchner *et al.*, "Elimination of Single Event Latchup in 90nm SRAM Technologies," in *2006 IEEE International Reliability Physics Symposium Proceedings*, San Jose, CA, USA, 2006, pp. 721–722. doi: 10.1109/RELPHY.2006.251342.

[63] A. Wilson *et al.*, "Radiation and Reliability Characterization of a Multiplexer Family Using a 0.35µm Triple-Well CMOS Technology," in *2011 IEEE Radiation Effects Data Workshop*, Las Vegas, NV, Jul. 2011, pp. 1–7. doi: 10.1109/REDW.2010.6062537.

[64] N. Rezzak and J.-J. Wang, "Single Event Latch-Up Hardening Using TCAD Simulations in 130nm and 65nm Embedded SRAM in Flash-Based FPGAs," *IEEE Trans. Nucl. Sci.*, vol. 62, no. 4, pp. 1599–1608, Aug. 2015, doi: 10.1109/TNS.2015.2450210.

[65] S. H. Voldman and E. G. Gebreselasie, "The influence of implanted sub-collector on CMOS latchup robustness," p. 10.

[66] C. K. Maiti, "Introducing Technology Computer-Aided Design (TCAD)," p. 438.

[67] H. de La Rochette, G. Bruguier, J. M. Palau, J. Gasiot, and R. Ecoffet, "The effect of layout modification on latchup triggering in CMOS by experimental and simulation approaches," *IEEE Trans. Nucl. Sci.*, vol. 41, no. 6, pp. 2222–2228, Dec. 1994, doi: 10.1109/23.340566.

[68] Synopsys, "Technology Computer Aided Design (TCAD) [online] Available." https://www.synopsys.com/silicon/tcad-html

[69] "Silvaco Inc. [online] Available." https://silvaco.com/tcad. .

[70] Y.-C. Wu and Y.-R. Jhan, *3D TCAD Simulation for CMOS Nanoeletronic Devices*. Singapore: Springer Singapore, 2018. doi: 10.1007/978-981-10-3066-6.

[71] N. D. Arora, J. R. Hauser, and D. J. Roulston, "Electron and hole mobilities in silicon as a function of concentration and temperature," *IEEE Trans. Electron Devices*, vol. 29, no. 2, pp. 292–295, Feb. 1982, doi: 10.1109/T-ED.1982.20698.

[72] "Sentaurus™ Device User Guide," p. 1530.

[73] R. Hacker and A. Hangleiter, "Intrinsic upper limits of the carrier lifetime in silicon," *J. Appl. Phys.*, vol. 75, no. 11, pp. 7570–7572.

[74] L. Huldt, N. G. Nilsson, and K. G. Svantesson, "The temperature dependence of band-to-band Auger recombination in silicon," *Appl. Phys. Lett.*, vol. 35, no. 10, pp. 776–777.

[75] W. Lochmann and A. Haug, "Phonon-assisted Auger recombination in Si with direct calculation of the overlap integrals," *Solid State Commun.*, vol. 35, no. 7, pp. 553–556, Aug. 1980, doi: 10.1016/0038-1098(80)90896-0.

[76] A. Michez, S. Dhombres, and J. Boch, "ECORCE: A TCAD Tool for Total Ionizing Dose and Single Event Effect Modeling," *IEEE Trans. Nucl. Sci.*, vol. 62, no. 4, pp. 1516–1527, Aug. 2015, doi: 10.1109/TNS.2015.2449281.

[77] L. Nagel and R. Rohrer, "Computer analysis of nonlinear circuits, excluding radiation (CANCER)," *IEEE J. Solid-State Circuits*, vol. 6, no. 4, pp. 166–182, Aug. 1971, doi: 10.1109/JSSC.1971.1050166.

[78] L. W. Nagel and D. O. Pederson, "SPICE (Simulation Program with Integrated Circuit Emphasis)," University of California, Berkeley, 1973.

[79] A. Vladimirescu and S. Liu, "The Simulation of MOS Integrated Circuits Using SPICE2:," Defense Technical Information Center, Fort Belvoir, VA, Oct. 1980. doi: 10.21236/ADA606827.

[80] T. L. Quarles, "Analysis of performance and convergence issues for circuit simulation," University of California, Berkley, 1989.

[81] L. Nagel, "SPICE2: A computer program to simulate semiconductor circuits." University of California, 1975.

[82] A. A. Youssef, "Etude par modélisation des évènements singuliers (SET/SEU/SEL) induits par l'environnement radiatif dans les composants électroniques," p. 159.

[83] J. M. Hutson, R. D. Schrimpf, and L. M. Massengill, "The Effects of Scaling and Well and Substrate Contact Placement on Single Event Latchup in Bulk CMOS Technology," in *2005 8th European Conference on Radiation and Its Effects on Components and Systems*, Cap d'Agde, France, Sep. 2005, pp. PC24-1-PC24-5. doi: 10.1109/RADECS.2005.4365577.

[84] Y. Gawlina, L. Borucki, G. Georgakos, and G. Wachutka, “Transient 3D Simulation of Single Event Latchup in Deep Submicron CMOS-SRAMs,” in *2009 International Conference on Simulation of Semiconductor Processes and Devices*, San Diego, CA, USA, Sep. 2009, pp. 1–4. doi: 10.1109/SISPAD.2009.5290213.

[85] Y. Moreau *et al.*, “The latchup risk of CMOS-technology in space,” *IEEE Trans. Nucl. Sci.*, vol. 40, no. 6, pp. 1831–1837, Dec. 1993, doi: 10.1109/23.273473.

[86] H. de La Rochette, G. Bruguier, J.-M. Palau, J. Gasiot, and R. Ecoffet, “Simulation of heavy ion latchup cross section curves,” in *Proceedings of the Third European Conference on Radiation and its Effects on Components and Systems*, Arcachon, France, 1996, pp. 359–364. doi: 10.1109/RADECS.1995.509803.

[87] A. Varotsou, “OMERE 5.0, 2017, [Online].” http://www.trad.fr/en/download/omere-us/

[88] L. Artola, G. Hubert, and T. Rousselin, “Single-Event Latchup Modeling Based on Coupled Physical and Electrical Transient Simulations in CMOS Technology,” *IEEE Trans. Nucl. Sci.*, vol. 61, no. 6, pp. 3543–3549, Dec. 2014, doi: 10.1109/TNS.2014.2362857.

[89] J. M. Hutson, “Single event Latchup in a deep submicron CMOS technology,” Vanderbilt University, Nashville, TN, 2008.

[90] S. H. Voldman, *Latchup*. John Wiley & sons, 2007.

[91] Voldman *et al.*, “Retrograde well and epitaxial thickness optimization for shallow- and deep-trench collar merged isolation and node trench SPT DRAM cell and CMOS logic technology,” in *International Technical Digest on Electron Devices Meeting*, San Francisco, CA, USA, 1992, pp. 811–814. doi: 10.1109/IEDM.1992.307482.

[92] J.-M. Palau, G. Hubert, K. Coulie, B. Sagnes, M.-C. Calvet, and S. Fourtine, “Device simulation study of the SEU sensitivity of SRAMs to internal ion tracks generated by nuclear reactions,” *IEEE Trans. Nucl. Sci.*, vol. 48, no. 2, pp. 225–231, Apr. 2001, doi: 10.1109/23.915368.